Exploring gravity, astrophysics, and cosmology with gravitational waves

A Thesis

Submitted to the

Tata Institute of Fundamental Research, Mumbai

for the degree of Doctor of Philosophy

in Subject Board of Physics

by

Aditya Vijaykumar

International Centre for Theoretical Sciences

Tata Institute of Fundamental Research

Bengaluru 560089, India

July 2023

Final version submitted in March, 2024

DECLARATION

This thesis is a presentation of my original research work. Wherever contributions of others are involved, every effort is made to indicate this clearly, with due reference to the literature, and acknowledgement of collaborative research and discussions. The work was done under the guidance of Professor Parameswaran Ajith, at the International Centre for Theoretical Sciences, Tata Institute of Fundamental Research, Bengaluru.

Aditya Vijaykumar

Aditya Vijaykumar

In my capacity as supervisor of the candidate's thesis, I certify that the above statements are true to the best of my knowledge.

Parameswaran Ajith

Date: 4th March, 2024

Dedicated to my parents, Rajani and Vijaykumar

And all other parents who struggle

So their children don't have to.

ACKNOWLEDGMENTS

I should be honest—I have dreamed of writing this section ever since I started my PhD! It gives me great pleasure to express thanks to so many people who were part of my PhD journey. While a PhD is often advertised as a lonely endeavour, I have realized over the years that that is not true. Hopefully, the record of people I thank here will be ample evidence for that.

In the summer of 2015, while interning at NCRA in Pune, I remember starting to learn general relativity from Bernard Schutz's popular textbook. The table of contents of that book was the first time I encountered the words "Gravitational Radiation". This immediately fuelled my curiosity; being the compulsive googler that I am, I started reading up about GWs online. It was there that I chanced upon two ex-students from my undergraduate institution who were working on gravitational waves. One of them had worked in the group of one Prof. Ajith Parameswaran at a new institute called ICTS[1]. "Nice to know", I thought to myself and moved on.

Cut to winter 2017. Gravitational waves were now a huge thing—GW150914, GW170817 and the Nobel Prize had made it *the* hottest topic in astronomy. At the same time I was, to put it mildly, in a scary position—my decision to shift out from astrophysics and spend my masters thesis doing high energy physics had not worked out, and I had no idea what I would do after graduating college. I thought gravitational waves were interesting, and decided to write an email to Ajith to see if he had any projects that I could work on based on my previous internship experience. Ajith replied almost immediately, and offered me a project, the results of which are included in this thesis. I am of course indebted to Ajith being the nicest and most supportive PhD mentor, teaching me how to do research, helping me become the scientist that I am today, and a million other things; but above everything else, I would like to thank Ajith for that project opportunity in late 2017—it meant a lot to me at that point, and it means a lot to me now.

Apart from his scientific contributions, Ajith's most impactful contribution to gravitational wave astronomy (at least in my opinion) is setting up the Astrophysical Relativity group at ICTS.

---

1. The other one would end eventually end up joining ICTS as a professor, and we would also end collaborating on multiple projects!

What a wonderful group of people! I would be short of words to describe how crucial the environment provided by the group was to my growth as a researcher, and I have a lot of people to thank for the same. Having the father of gravitational wave astronomy in India as a towering presence in our group activities was inspiring and humbling at the same time, and I thank Bala for all his advice and encouragement over the years. In my later years of graduate school, I have had a blast discussing various aspects of gravitational wave detection and waveform accuracy with Prayush, apart from learning a lot many things about scientific computing from him. I also want to thank Rama, Loga, and Pallavi for all the support and conversations through the years.

I learned most practical things about gravitational-wave astronomy and astrophysics by continuously bothering the postdocs at ICTS, in particular, the early postdoc bunch of Sumit, Rahul, Haris, and Gayathri. I am sure they were irritated when I would barge into their office without rhyme or reason, but I thank them for always being patient and kind both in work matters and otherwise. Sumit, especially, was the best first mentor and collaborator I could have asked for. Among other things, it was he who first impressed upon me the importance of well-written code, which would end up defining my outlook towards working on any project. After this bunch of postdocs left, Apratim and Shasvath made sure that their absence wasn't felt too much. Apratim, apart from being a very easy collaborator on multiple projects, has also been a very good friend and listener-of-problems. Shasvath is a collaborator on three out of the four works in this thesis—I think that is proof enough of how crucial he has been in the completion of my PhD. A lot of the way I think about research topics in astrophysics is influenced by Shasvath, but most of all, I would like to thank him for showing me how to come up with an idea and see it to completion. I really admire the knack he has for this process. I would also like to thank my fellow graduate students in the group for all the good times—Soummyadip, Srashti, Aditya S, Mukesh, Uddeepta, Souvik. Thanks also to Adhrit, Kruthi, and Kaustubh for allowing me to experience the joy of mentoring them.

The seven months that I spent at The University of Chicago as a Fulbright-Nehru fellow was career-defining in a number of ways. For this opportunity, I am eternally grateful to Daniel Holz.

Lastly, if you are reading this and are going through mental health problems or feeling the imposter syndrome in graduate school, you are definitely not alone. I promise you it will get better. The next hundred pages are one example of that.

LIST OF FIGURES

xii

LIST OF TABLES

CONTENTS

ABSTRACT

In this thesis, we shall explore a few possibilities of probing gravity, cosmology, and astrophysics using observations of gravitational waves from current and future detectors. We first develop a method to place constraints on the time variation of the gravitational constant G using the detected LIGO-Virgo binary neutron star events. We then ask if a binary neutron star merger near a supermassive black hole could enable a detection of the elusive post-merger gravitational wave signal. Continuing on the theme of mergers near supermassive black holes (and in general gravitational potentials), we investigate how well we can measure the imprint of centre-of-mass acceleration. Finally, we develop a method to measure the two-point correlation function using binary black hole observations in proposed next-generation gravitational wave detectors, accounting for localization uncertainties and realistic merger rates.

CHAPTER 1

INTRODUCTION

In the year 1915, Albert Einstein presented the general theory of relativity as a theory of gravity [21]. Although general relativity was consistent with Newtonian gravity in the latter's regime of validity, it was a marked conceptual departure from the Newtonian picture of gravity, in that it viewed gravity as arising from the curvature of spacetime. This paradigm shift in the conception of gravity had many interesting implications, including the prediction (by Einstein himself [22]) of the existence of gravitational waves (GWs).

GWs are produced by time-varying quadrupole (and higher) moments of mass-energy distributions. GWs interact with test masses by squeezing their spatial separation in one direction and stretching it in the orthogonal direction. There are several proposed ways of detecting GWs, but laser interferometers [23, 24] have been the most successful. It should be noted that GWs from a typical black hole binary system (such as the one from GW150914 [25]) produce extremely small displacements of $\sim 10^{-19}$ metres on a kilometre-scale interferometer, and it is a testament to years of scientific and technological advancements that we can now detect GWs.

When massive stars run out of their nuclear fuel and are no longer able to support their own gravity, they collapse and form dense, compact objects like black holes and neutron stars. The most promising sources of GWs that can be detected with laser interferometers are the merger of such compact objects. These mergers produce a signal in the laser interferometers with a characteristic *chirp* morphology i.e. the amplitude and the freqeuncy of the signal increase with time until the merger is complete. On September 14th, 2015, the Laser Interferometer GW Observatories (LIGO) at Livingston, Louisiana and Hanford, Washington in the United States of America detected GWs from the merger of two $\sim 30 M_\odot$ black holes at a distance of ~ 400 Mpc [25]. This first detection immediately provided constraints on various aspects of physics and astrophysics such as the validity of general relativity [26] and the merger rate of binary black holess (BBHs) [27]. On August 17th, 2017, LIGO along with the Virgo detector in Cascina, Italy also detected a GW signal from the merger of two neutron stars at a distance of ~ 40 Mpc [28]. This event was followed up by

electromagnetic telescopes all around the world [29], localizing the event inside the galaxy NGC 4993 while also detecting a short gamma-ray burst GRB 170817A and a kilonova powered by the radioactive decay of r-process nuclei synthesized in the merger ejecta. This observation allowed constraints to be placed on the speed of GWs [29], Hubble constant [30], cosmological models of dark energy and modified gravity [31, 32] and the neutron star equation of state [33].

At the time of writing, the LIGO-Virgo-KAGRA network of detectors have detected GW signals from ∼ 90 compact binary mergers over three observing runs [34]. The aggregate properties of these events have shed light on the population of merging binaries in the Universe [35]. These detectors are expected to be upgraded to better sensitivities in the next few years [36, 37, 38], while an additional LIGO detector in India (LIGO-India [39]) is expected to come online in the current decade. Moreover, the next generation of ground-based detectors including Einstein Telescope [40, 41] and Cosmic Explorer [42, 43] are expected to go online in the next decade. All these improvements would enable the detection of hundreds of thousands of compact binary detections with much better localization [44, 45], thus opening up immense possibilities for precision astrophysics and cosmology. This thesis explores some of the astrophysics, cosmology, and fundamental physics knowledge that can be harnessed from current and future GW observations.

In this chapter, we will briefly review basic aspects of GWs, describe how they are detected, how the parameters of the source are estimated, and how these observations can be used to shed light on various aspects of physics and astrophysics.

1.1   Sources of GWs

To understand what configurations of mass/energy produce GWs, it is useful to draw an analogy with electromagnetism. The following discussion can be found in standard textbooks on gravitation [46, 47, 48]. Specifically, let's consider electromagnetic radiation, and its connection with the multipole moments of a charge distribution $\rho_q(\vec{\mathbf{r}})$. For a multipole to be radiative, it should vary in time. However the monopole term $\int \mathrm{d}^3\vec{\mathbf{r}} \, \rho_q(\vec{\mathbf{r}})$ is equal to the total charge Q, which is always conserved. Hence, monopole radiation is prohibited in electromagnetism. However, the

dipole term $\int \mathrm{d}^3\vec{\mathbf{r}}\,\vec{\mathbf{r}}\,\rho_q(\vec{\mathbf{r}})$ has no such associated conservation law, and dipole radiation is possible in electromagnetism.

Now, let's consider a mass distribution $\rho(\vec{\mathbf{r}})$ and its associated multipoles. Similar to electromagnetism, the monopole $\int \mathrm{d}^3\vec{\mathbf{r}}\,\rho(\vec{\mathbf{r}})$ is conserved and is equal to the total mass. However, unlike electromagnetism, the dipole term $\int \mathrm{d}^3\vec{\mathbf{r}}\,\vec{\mathbf{r}}\,\rho(\vec{\mathbf{r}})$ is also conserved due to the conservation of linear momentum. Hence, at least a time-varying quadrupole moment is required for the generation of GWs. Specifically, the quadrupole formula derived by Einstein [22] says that the GW amplitude h_{ij} is proportional to the second time-derivative of the quadrupole moment Q_{ij}. That is,

$$ h_{ij} = \frac{2G}{c^4}\frac{1}{r}\frac{\partial^2 Q_{ij}}{\partial t^2} \quad . \tag{1.1} $$

Here, r is the distance of the source from the observer, and G and c are Newton's gravitational constant and the speed of light in vacuum respectively.

Approximating $\frac{\partial^2 Q_{ij}}{\partial t^2} \sim MR^2\omega^2$ where M is the mass, R is the characteristic dimension, and ω is the characteristic frequency of the system, and assuming $\omega^2 R^3 = GM$ we get that the strain h follows

$$ h \simeq 10^{-22}\left(\frac{M}{2.8M_\odot}\right)^{5/3}\left(\frac{\omega}{100\ \mathrm{Hz}}\right)^{2/3}\left(\frac{r}{100\ \mathrm{Mpc}}\right)^{-1} \quad . \tag{1.2} $$

The expression above tells us that, indeed, GWs produce a very small strain of $\sim 10^{-22}$ even from a system as massive as a binary neutron stars (BNS) at a distance of 100 Mpc orbiting at a frequency of 100 Hz. This also means that GWs from such a source will change the length of a kilometre-long object (i.e. typical length of GW detectors) by around 10^{-19} metres. This explains why, even if we build these long detectors, GWs are extremely challenging to detect. A lot of progress in quantum measurement science and technology have gone into making the measurement of these tiny disturbances possible. We shall not delve into these aspects in this thesis, and we refer the reader to Ref. [49] for further reading.

1.1.1 Modelling GWs from inspiralling binaries of compact objects

From the order-of-magnitude analysis above, it is clear that one requires massive objects at high frequencies for the GW emission from them to be efficient. The most natural setting for such a system is a binary composed of compact objects such as black holes or neutron stars. To search for these signals in GW data, one needs theoretical templates predicted by general relativity. We would also require these templates to be extremely accurate in modelling the phase of the GW signal, since GW detectors can measure the phase to a precision of $\sim \text{SNR}^{-1}$ [50], where SNR is the signal-to-noise ratio. However, we run into a problem. Unlike Newtonian dynamics, the two-body problem (or the "Kepler problem") does not have a known exact analytical solution in general relativity [51]. This makes accurate modelling the GW signal from inspiralling binaries extremely challenging. One way to solve the problem is to resort to approximation techniques.

One approximation scheme, called the post-Newtonian (PN) expansion, involves writing the dynamics of the two-body problem as a series expansion in v/c, where v is the orbital velocity of the binary system. The history of this approximation scheme goes back to the very beginning of general relativity, when Einstein calculated relativistic corrections to the precession of the perihelion of Mercury upto leading order in v/c [52]. PN expansion has also been used to great success in explaining changes in the orbital period of binary pulsars [53]. However, describing binary pulsars only requires going to the second of third term beyond the leading order, since the typical $v/c \sim 10^{-3}$ for these systems. Sources in the band of ground-based GW detectors reach $v/c > 0.5$, requiring the knowledge of the PN expansion to very high order. Many efforts over the past decades (for a review, see Ref. [54]) have led to the derivation of the GW phase complete upto $(v/c)^7$ (3.5 PN) for binaries of compact objects with arbitrary masses and spin angular momenta. That is, we can write the GW phase $\Psi(f)$ as a function of frequency f under the stationary phase approximation as:

$$\Psi(f) \sim v^{-5} \sum_{k=0}^{7} \Psi_k(\vec{\theta}) v^k \quad , \quad v = (\pi G M f/c^3)^{1/3} \quad , \tag{1.3}$$

4

where $\vec{\theta}$ is the set of intrinsic parameters (masses, spins, tidal deformabilities, etc.) of the binary system, and $\Psi_k(\vec{\theta})$ are the PN coefficients. PN expansions form the cornerstone for most GW waveform models. Very recently, Ref. [55] have also calculated the 4 PN corrections to the phase, but for non-spinning systems.

The fact that PN calculations only exist upto a certain order beyond the leading term naturally defines the regime of applicability of the approximation scheme. When objects in the binary are very close to each other (i.e. $v/c \sim 1$), the PN approximations break down, and no analytical approximation techniques can be used. One needs to resort to solving the two-body problem numerically. However, numerically solving Einstein's equations is complicated; some reasons for this are:

1. Einstein's equations are a set of ten coupled nonlinear partial differential equations. Solving these incurs a very high computational cost.

2. Using the Arnowitt-Deser-Misner (ADM) formalism [56], Einstein's equations can be cast into an initial value problem. The main idea here is to foliate the (four-dimensional) space-time into (three-dimensional) spacelike slices which evolve in time. This reduces Einstein's equations to a set of time evolution equations, and a set of constraint equations. However, these evolution equations are only *weakly hyperbolic*, which means that they do not necessarily permit a well-posed Cauchy problem. This essentially means that there is no reason to expect numerical solutions of these equations to be well-behaved.

3. General relativity permits gauge freedom. However, not all gauge choices are suitable for numerical evolution of Einstein's equations. For instance, we do not want to use a gauge containing (unphysical) singularities, which might result in the numerical algorithm blowing up. We would also like a gauge that follows the symmetries of the system approximately, if not exactly.

The solutions to these and other problems required various advances in the formulation of Einstein's equations, computational schemes, and computer hardware. Numerical solutions of the

5

two-body problem in general relativity are now commonplace, with at least a few different groups working independently. For description of the progress and outstanding challenges, see Ref. [57].

Apart from GWs emitted by the two compact objects inspiralling and eventually merging, GWs are also emitted when the new, composite object settles down from a perturbed state to its equilibrium state. The GWs emitted by black holes in this regime are very well described by black hole perturbation theory, which predicts that the compact objects will emit a set of quasi-normal modes whose frequencies and damping times depend only on the intrinsic properties of the compact object. Calculations of these quasi-normal modes have a long history starting with Ref. [58]; how long after merger do the GWs emitted start being well-described by perturbation theory is a matter of debate in the community (see e.g. [59, 60, 61, 62]). Perturbative calculations of the post-merger GW spectrum for neutron stars is more complicated, and needs to take into account, for example, the fluid oscillation modes of the star.

To summarize:

1. PN expansions are good for describing the dynamics in the early inspiral, when the characteristic orbital velocity of the system is low. Although PN expansions are analytically complicated to derive, they are very easy to evaluate for any value of the source parameters.

2. Perturbation theory is a good descriptor for the post-merger dynamics of compact objects. Once calculated, they are also simple to evaluate.

3. Numerically solving Einstein's equations is the only way to understand GW emission when characteristic velocities of binaries are large. However, these numerical solutions are computationally expensive and are possible only for a finite set of points in the full parameter space.

Ideally, for full broad-band analysis of GW data, one would like to have a template which stitches together the inspiral, merger, and post-merger regimes. This is the philosophy behind the "phenomenological" methods (see e.g. [63]) and the "effective-one-body" formalism (see e.g. [64]) of modelling waveforms .

1.2 Data analysis aspects of GWs

Extracting information from GW data is the classic "needle in a haystack problem"—we search for weak signals in data that is overwhelmed by noise. As such, data analysis of GWs is divided into two broad steps. The first involves detecting the signals buried in the data by comparing the data against a (relatively) small set of template waveforms—this tells us exactly where a signal is present in the data. The second step involves inferring the source parameters by comparing the data segment containing the signal with a much larger number of template waveforms, typically using stochastic sampling techniques. We describe both of these steps briefly in this section.

1.2.1 Searching for GWs

Although GW signals are buried deep within detector noise, we can use information on the shape of the GW signal to set up searches for GWs using the "matched filtering" technique [65]. The idea here is to formulate an optimal detection statistic given a set of theoretical templates for the signal, and a model for the noise.

Under the assumption of stationary and zero-mean gaussian noise, it turns out that matched-filtering is easily formulated in the frequency domain. Under these assumptions, the noise properties are completely specified by the 'noise power spectral density' $S_n(f)$, defined by [50]

$$\left\langle \tilde{n}(f)\tilde{n}(f') \right\rangle = \frac{1}{2} S_n(f) \delta(f - f') \tag{1.4}$$

where $\tilde{n}(f)$ is the Fourier transform of the time-domain noise $n(t)$ in the GW detector. $S_n(f)$ is proportional to the variance of the noise at each frequency—higher the value of $S_n(f)$ at a certain frequency, lesser is the sensitivity of a detector to GWs at that frequency. The symbol $\langle \rangle$ denotes average over multiple chunks. Let $\tilde{d}(f)$ be the Fourier transform of the time domain detector data, and $\tilde{h}_{\vec{\theta}}(f)$ be the template of the signal in Fourier domain for a set of source parameters $\vec{\theta}$. Further, let $\mathcal{T}$ be the set of theoretical templates created to ensure that that no GW signal is missed. Given all these, the detection statistic called the matched-filter signal-to-noise ratio (SNR) can be defined

as [66],

$$\rho^2_{\text{mf}} = \max_{\vec{\theta} \in \mathcal{T}} 4 \int_{f_{\min}}^{f_{\max}} df \, \frac{\tilde{d}^*(f) \, \tilde{h}_{\vec{\theta}}(f)}{S_n(f)} \quad . \tag{1.5}$$

Basically, matched filtering tells us that to optimally detect a GW signal present in data, one should calculate a frequency-integrated, noise-weighted product of the data and the theoretical template for different values of source parameters in the "template bank". Typically, when the value of the matched-filter SNR is above a certain threshold, a GW event is said to be detected. However, the false alarm rate (FAR), a statistic that takes into account the presence of non-gaussianities in the data) and the probability of the signal being astrophysical p_{astro} are more commonly-used detection statistics nowadays.

1.2.2 Inferring source parameters from a GW signal

A search pipeline typically computes the matched-filter SNR, the best-match template, an effective distance to the source (which combines the amplitude-dependence of the luminosity distance and orientation angles), an estimate for the false alarm rate, and the probability of the signal being astrophysical p_{astro} (see e.g. [67]) as opposed to terrestrial. For further analyses, it is desirable to have a more fine-grained description of source properties. This is generally done by using Bayesian inference techniques coupled with stochastic samplers.

Bayesian inference allows us to construct the *posterior distribution* $p(\vec{\theta}|d)$ of the source parameters $\vec{\theta}$, by writing it in terms of the *likelihood function* $\mathcal{L}(d|\vec{\theta})$ and the *prior probability* distribution $\pi(\vec{\theta})$. This follows directly from the Bayes theorem, and can be written as,

$$p(\vec{\theta}|d) = \frac{\mathcal{L}(d|\vec{\theta})\pi(\vec{\theta})}{\mathcal{Z}} \quad , \tag{1.6}$$

where $\mathcal{Z} = \int d\vec{\theta} \, \mathcal{L}(d|\vec{\theta})\pi(\vec{\theta})$ is called the *evidence*. The evidence can be thought of an overall normalization factor, and is useful while comparing two or more hypotheses for the data.

Under the assumption of Gaussian and stationary noise, the likelihood in the frequency-domain

can be written as (see e.g. [68])

$$\mathcal{L}(d|\vec{\theta}) \propto \exp\left(-2 \int_{f_{\min}}^{f_{\max}} \mathrm{d}f \, \frac{\left|\tilde{d}(f) - \tilde{h}_{\vec{\theta}}(f)\right|^2}{S_n(f)}\right) \tag{1.7}$$

The derivation of the above proceeds by working in the fourier domain and demanding that the noise at each frequency f is gaussian and stationary.

Bayesian inference gives us a very elegant formalism to infer source properties. However, although the formalism is simple, the GW source property inference problem is complicated by the fact that the dimensionality of the parameter set is large (15 in the case of standard BBHs, 17 in the case of BNSs). In such cases, one uses stochastic samplers to sample the posterior distribution (for a review, see e.g. [69]). Stochastic samplers start out with a set of randomly distributed points (say, following the prior) and take stochastic steps to other points in the parameter space if the step increases the posterior probability. There are many stochastic sampling algorithms and corresponding implementations. Due to the multimodal nature of GW posterior distributions, nested sampling techniques [70] are used most frequently.

1.3 Status of observations

The LIGO and Virgo network of detectors has detected a total of 90 binaries passing $p_{\mathrm{astro}} >$ 0.5 [34]. These detections involve binaries consisting of two neutron stars, two black holes, or one black hole and one neutron star. One of the BNSs, GW170817 [28], also had signatures in all bands of the electromagnetic spectrum [29]. Below, we describe how GWs have furthered our understanding about astrophysics, gravity, and cosmology.

1.3.1 Implications for astrophysics

1. The inspirals of BNSs contain imprints of the tidal deformation of the component stars, which can be used to constrain the radius of the stars and hence the equation of state of the

dense matter inside these stars. The observation of GW170817 constrained the radii of the two stars to be $11.9^{+1.4}_{-1.4}$ km[1][33]. This measurement ruled out a large number of candidate equations of state that predicted higher radii for a given mass (called *soft* equations of state, as opposed to *stiff* equations of state). Further observations of BNSs have not yielded better constraints over and above those from GW170817 [71].

2. The observation of a kilonova accompanying GW170817 identified BNS mergers as sites of r-process nucleosynthesis [72], thus explaining how heavy elements are synthesized in the universe. The GW signal was used to estimate the mass of the dynamical ejecta, finding $M_{\text{ejecta}} = 10^{-3} - 10^{-2} M_{\odot}$ [73]. Kilonova lightcurves have also been used to constrain the ejecta properties (e.g. [74, 75]).

3. GW170817 was also accompanied by a short gamma ray burst (sGRB) GRB 170817A [76]. This observation confirmed the existence of relativistic jets in BNS mergers, possibly produced by the tidal disruption of the neutron stars just before merger. However, the luminosity of GRB 170817A was much weaker than other sGRBs detected at similar redshifts; this could be attributed a various reasons, including the non-alignment of the jet with the line-of-sight (see Ref. [77] for a review).

4. The merger rate of BBHs is constrained to be between $18 - 44 \, \text{Gpc}^{-3}\text{yr}^{-1}$, that of BNSs is constrained to be between $10-1700 \, \text{Gpc}^{-3}\text{yr}^{-1}$, and that of NSBHs is $7.8-140 \, \text{Gpc}^{-3}\text{yr}^{-1}$ [35]. The rate of BBHs is the best measured since most of the detected binaries are BBHs.

5. The primary-mass distribution of BBHs broadly is well-described by a power-law along with the addition of a gaussian peak. The physical motivation behind using this parametrization is that black hole masses would be expected to follow a power-law due to the power-law nature of the initial mass function of stars [78]. The extra peak in the model is to account for the possible existence of the pulsational pair instability supernova (PPISN) [79] pile-up. The power law exponent α ($p(m) \propto m^{-\alpha}$) is constrained to be $\alpha = 3.5^{+0.6}_{-0.56}$, and there is

---

1. This constraint depends on the choice of prior. For a full set of constraints, see Ref. [33].

evidence for a gaussian peak centred around $34^{+2.6}_{-4.0}M_\odot$ [35]. The existence of the peak is robust against choice of models [80, 81] or noise-induced uncertainties [82], but whether it originates from the PPISN process is uncertain (see for e.g. [83] and references therein). There is also some evidence for a peak at the lower end of the mass distribution, at $\sim 10M_\odot$, and some lesser evidence of structure in the mass distribution at other masses [80, 35].

6. GW data has also shed light on the spin distribution of black holes. For instance, the population-level distribution of the mass-weighted sum of spins in the direction of the orbital angular momentum (called effective spin χ_{eff}) reveals that most support lies around $\chi_{\text{eff}} = 0$, but also has support for $\chi_{\text{eff}} = 0.6$ at the higher end [35]. There is also evidence for negative χ_{eff} in the population [35].

7. Naively, one would expect the redshift scaling of the BBH merger rate to be proportional to the formation rate of stars, which increases with redshift. Current observations indeed show that the merger rate of BBHs increases with redshift [35], and is consistent with the evolution of the cosmic star formation rate [84].

8. The mass distribution of NSBHs and BNSs are not very well constrained. However, there is evidence for a dip in the detections between $3 - 5M_\odot$ [35]. The mass distributions of GW-detected neutron stars also do not prefer a peak at $1.33M_\odot$ where Galactic radio pulsars prefer a peak [35].

1.3.2 Implications for gravity and cosmology

The detection of GWs has enabled a wide variety of probes of gravity and cosmology. Below, we summarize some results from these probes:

1. The inspiral and the post-inspiral parts of the GW signal are consistent with general relativity, in that the mass and spin of the remnant black hole estimated independently from both regimes are consistent with each other [85].

11

2. Adding extra deviation parameters to each order in the PN expansion, it has been shown that the PN coefficients do not deviate from their GR predictions [85].

3. It has also been shown that the GWs are non-dispersive, in that the follow a dispersion relation $E = pc$, where E is the energy and p is the momentum [85]. In particular, this fact can be used to place bounds on the existence of a massive graviton, whose mass has been constrained to be $m_g < 1.27 \times 10^{-23} \mathrm{eV}/c^2$ from GW observations [85].

4. There is evidence for the existence of quasi-normal modes in the post-merger regime of GW150914. This has enabled consistency tests of the final mass and final spin [85]. There have also been claims of the existence of overtones and higher modes in the data [61, 86], but these have been contested in the literature [62, 87, 88].

5. The detection of both electromagnetic waves as well as GWs from GW170817 at roughly the same instant of time have enabled many precision gravity tests [89], including constraints on the mass of the graviton [89], speed of GWs [76], existence of additional spacetime dimensions [90, 89], and ruling out a large class of modified gravity theories [32].

6. Since GWs give an independent measurement of the luminosity distance out to the source, they can be used to constrain the Hubble constant H_0 with redshift information obtained through identification of the host galaxy [91, 92], cross-matching [91, 93] or cross-correlation with galaxy catalogs [94, 95], or "standard" features in the mass spectrum [96, 97]. The localization of GW170817 to its host galaxy due to the associated kilonova enabled a measurement of the Hubble constant $H_0 = 70.0^{+12.0}_{-8.0}$ km s^{-1} Mpc^{-1} [30]. This measurement combined with those obtained by cross-matching localization volumes of BBHs with galaxy catalogs yields $H_0 = 68^{+8}_{-6}$ km s^{-1} Mpc^{-1} [98].

1.4 Outline of this thesis

In this thesis, we shall explore a few possibilities of probing gravity, cosmology, and astrophysics using observations of GWs from current and future detectors. We place constraints on the time variation of the gravitational constant G using the observed BNS events GW170817 and GW190425 [2] in Chapter 2. In Chapter 3, we ask if a BNS merger near a supermassive black hole (SMBH) could enable a detection of the elusive post-merger GW signal. Continuing on the theme of mergers near SMBHs (and in general gravitational potentials), we place upper limits on the centre-of-mass acceleration of GW170817 and GW190425, and investigate how well current and future detectors can measure the imprint of this acceleration in Chapter 4. Finally, in Chapter 5, we develop a method to measure the two-point correlation function using BBH observations in proposed next generation (XG) GW detectors, accounting for localization uncertainties and realistic merger rates.

CHAPTER 2

CONSTRAINING TIME VARIATION OF THE GRAVITATIONAL CONSTANT

2.1 Introduction

P. A. M. Dirac was the first to conjecture the possibility of variation of fundamental "constants" of Nature with cosmic time [99, 100] (see also [101, 102, 103]). Since then, a number of alternative theories of gravity, e.g., scalar-tensor theories like Brans-Dicke theory, that predict a time varying gravitational "constant" G [104, 105], have been constructed. In general, most theories of gravity that violate the strong equivalence principle predict that the value of the gravitational constant varies with cosmic time [106].

There are several observational bounds on the time variation of G, constraining its value at various cosmological epochs [105]. These include constraints derived from comparing the observed abundance of light elements with the abundance predicted by Big Bang nucleosynthesis models [107, 3, 108], those derived from the shape of the angular power spectrum of the cosmic microwave background [109], from the light curves of type Ia supernovae [110, 111, 112, 113, 114, 115], from the non-radial pulsations (asteroseismology) of white dwarfs [4], from the timing [5] and the observed mass distributions [6] of binary pulsars, from the age of globular clusters [116], from helioseismology [7], and from monitoring the orbits of solar system planets [117, 118, 119] and the Earth-Moon system through radar ranging [120] and lunar laser ranging (LLR) [121, 8]. Here, we show how the observation of GW signals from BNSs can be used to constrain the time evolution of G. Assuming a monotonic variation in G, we also produce observational constraints on the time variation of G from the BNS observations by LIGO and Virgo [28, 2]. To the best of our knowledge, this is the first such constraint placed that uses the GW signal from a BNS system. It is also fourteen orders of magnitude better than the existing GW based constraint (from constraints on the dephasing of BBH waveforms) [122]. We also show that the next generation of GW detectors will improve these constraints by several orders of magnitude.

14
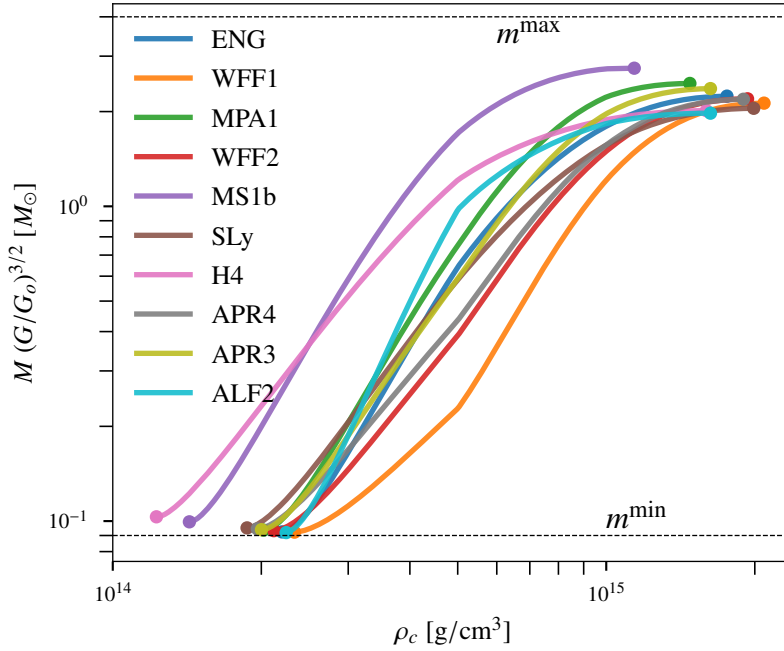
Figure 2.1: The mass of non-spinning neutron stars as a function of the central density ρ_c. These are computed by numerically solving the equations of hydrostatic equilibrium in general relativity assuming different equations of state (shown in the legend). We rescale the mass by $(G/G_o)^{3/2}$ where G is the value of the gravitational constant used to solve the equations and $G_o = 6.67 \times 10^{-11}$ m^3 kg^{-1} s^{-2} the current value of G. These relations between the rescaled mass and central density are independent of the value of G used to compute the mass. The dots at the end of the curves correspond to the maximum/minimum mass supported by each equation of state. The horizontal dashed lines correspond to the maximum/minimum possible mass of neutron stars that we assume in this chapter, independent of the equation of state.

2.2 Neutron star mass limits and the gravitational constant

The mass of a spherically symmetric star is determined by the following equations of hydrostatic equilibrium

$$\frac{dm(r)}{dr} = 4\pi r^2 \rho(r), \quad \frac{dP(r)}{dr} = \frac{-G \, m(r) \, \rho(r)}{r^2} \, C(r), \tag{2.1}$$

where $m(r)$ denotes the (gravitational) mass enclosed by a radius r while $P(r)$ and $\rho(r)$ denote the pressure and density at r. The dimensionless quantity $C(r)$ denotes the relativistic corrections. That

15

is, $C(r) = 1$ in Newtonian gravity, and

$$C(r) = \left[1 + P(r)/\rho(r)c^2\right]\left[1 + 4\pi r^3 P(r)/m(r)c^2\right]\left[1 - 2Gm(r)/c^2 r\right]^{-1} \qquad (2.2)$$

in general relativity [123], while $C(r)$ depends on additional quantities such as scalar fields in alternative theories of gravity (see, e.g., [124]). The mass of the star can be computed by solving Eq. (2.1) along with an equation of state that relates the density and pressure.

A dimensional analysis of Eq. (2.1) reveals that the mass of the star scales as $G^{-3/2}$. This is illustrated in Fig. 2.1, which shows the mass of non-spinning neutron stars as a function of the central density, computed by numerically solving the equations of hydrostatic equilibrium in general relativity [123]. We rescale the mass by $(G/G_o)^{3/2}$, where G is the value of the gravitational constant used to solve the equations and $G_o = 6.67 \times 10^{-11}$ m^3 kg^{-1} s^{-2} the current value of G. The rescaled mass as a function of the central density is independent of the value of G used to compute the mass. In particular, for a given equation of state, the central densities corresponding to the maximum and minimum masses are independent of G.

We entertain the possibility that the value of the gravitational constant during the merger, G_s, could be different from its current value G_o [125]. Following common practice [105, 106], we assume that all other fundamental constants and fundamental interactions (and hence the nuclear equation of state) remain unchanged across cosmic time [1]. It is well known that neutron stars have a minimum (maximum) mass limit [126] below (above) which the neutron star will gravitationally unbind (collapse). Fig. 2.1 shows that these mass limits scale as $G^{-3/2}$. Thus, the mass limits on the neutron star at the time of the merger are given by

$$m_s^{\text{min, max}} = m^{\text{min, max}} (G_s/G_o)^{-3/2} \qquad (2.3)$$

where $m^{\text{min, max}}$ are the minimum and maximum mass limit computed using the current value

---

1. A variation in G should also affect the nuclear reaction rates and hence the stellar evolution. This will alter the rate of compact binary mergers at various cosmological epochs. We neglect this effect while estimating the expected constraints using upcoming detectors.

of the gravitational constant, G_{o}. The precise values of $m^{\mathrm{min,\,max}}$ will depend on the nuclear equation of state, which, to date, remains an open question. Nevertheless, guided by the plethora of available equation of state models, we can make a conservative choice of $m^{\mathrm{min}} = 0.09\,M_{\odot}$ [127] and $m^{\mathrm{max}} = 4\,M_{\odot}$ (shown by horizontal dashed lines in Fig. 2.1), where the maximum mass includes the effects of maximal rotation [128, 129].

2.3 Constraining the cosmic evolution of the gravitational constant

The GW signal produced by the inspiral of a BNS system can be written in the frequency domain as $h(f) = A(f)\exp\{i\,\Psi(f)\}$, where $A(f)$ is the amplitude, $\Psi(f)$ is the phase and f is the Fourier frequency. The post-Newtonian expansion of the phase is given by [130]

$$\Psi(f) = \frac{3}{128\,\eta\,v^5}\,\sum_{k}\psi_k(\lambda)\,v^k. \tag{2.4}$$

Here, $v := \left(\pi\,G_{\mathrm{s}}M_{\mathrm{s}}f/c^3\right)^{1/3}$ is a dimensionless parameter, where $M_{\mathrm{s}} = m_{\mathrm{s},1} + m_{\mathrm{s},2}$ is the total mass of the binary, while ψ_k are some dimensionless coefficients that depend on a set of intrinsic parameters λ of the binary, such as the symmetric mass ratio η and dimensionless spins of the neutron stars, but *not* on the value of G [2].

The detection of GWs from compact binaries, and the estimation of source parameters is performed by phase matching the data with theoretical templates of the expected signal. Typically, several hundreds of thousands of templates, corresponding to different values of source parameters λ, need to be correlated with the data. These templates are generated using the current value G_{o} of the gravitational constant. That is, templates use $v := \left(\pi\,G_{\mathrm{o}}M_{\mathrm{o}}f/c^3\right)^{1/3}$ in Eq. (2.4), where M_{o} is the total mass of the binary parametrizing a given template.

---

2. The parameters that appear in the waveform describing the effects of the internal structure of the neutron stars (e.g., spin- and tidal-induced deformations) *do* depend on G. However, their (dimensionless) contributions to the waveform are G-independent, similarly to how they are not affected by the cosmological redshift [131]. Additionally, the phase of the GW also depends on extrinsic parameters such as the location and orientation of the binary, which do not affect the current discussion.
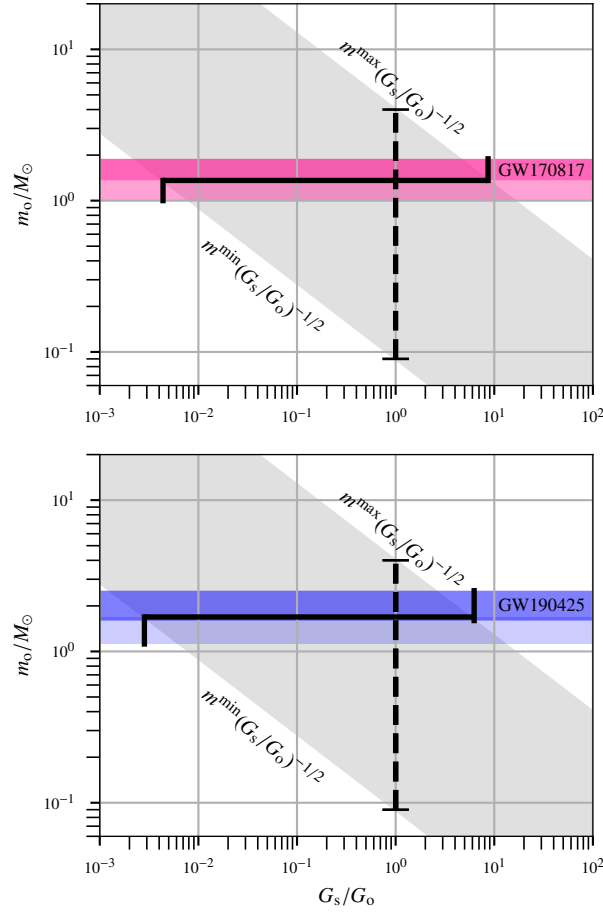
Figure 2.2: The horizontal axis corresponds to the assumed value of G at the epoch of the merger of the neutron stars, denoted by G_s (in units of the current value G_o), and the vertical axis corresponds to the measured value of the neutron star mass m_o (in units of solar mass) from GW observations. The horizontal patches correspond to the measured value of the neutron star masses from GW170817 and GW190425 (90% credible regions of the marginalized posteriors on the component masses [1, 2]; darker shades correspond to primary masses while lighter shades correspond to secondary masses). The vertical dashed lines correspond to the theoretically allowed range of neutron star masses $m^{\min} - m^{\max}$ calculated using the current value, G_o, of the gravitational constant. The tilted gray regions show the allowed range of the observed neutron star mass; i.e., $m^{\min} (G_s/G_o)^{-1/2}$ to $m^{\max} (G_s/G_o)^{-1/2}$, where $m^{\min} = 0.09 M_\odot$ and $m^{\max} = 4 M_\odot$. The horizontal error bars show the constraints on G_s/G_o that we obtain by requiring that the measured values overlap with the theoretically allowed (gray) region.

Template matching is achieved when the phase of the template is matched with the phase of the signal, which, in turn, occurs when the set of parameters λ of the templates matches that of the source. It can be seen from Eq. (2.4) that, in addition, the following condition also has to be
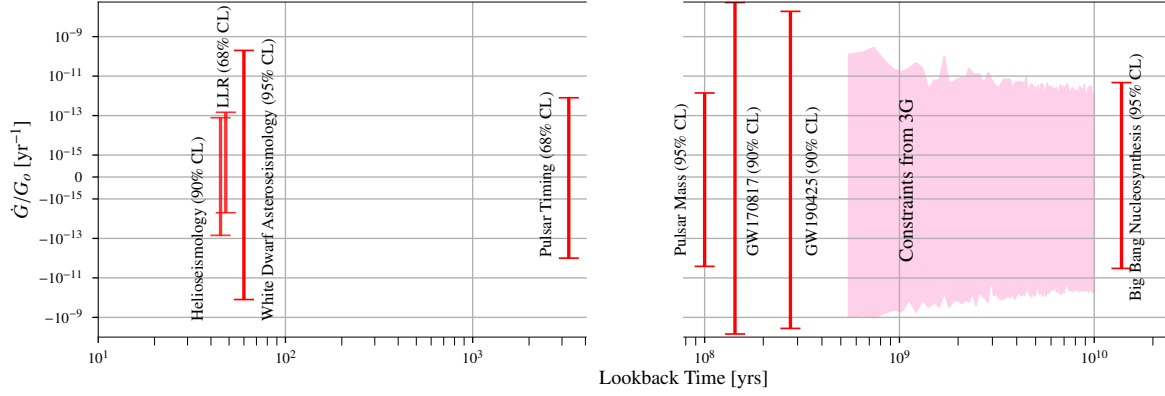
Figure 2.3: Comparison of the constraints on $\dot{G}/G_o$ obtained from various observations with confidence levels of the constraints indicated in brackets (LLR denotes constraints from lunar laser ranging). The horizontal axis shows the look back time. The constraints presented this chapter are labeled as GW170817 and GW190425, while the expected constraints from 10 year of observations with XG GW detectors is shown by the pink band. We also plot constraints obtained from Big Bang nucleosynthesis models [3], white dwarf astroseismology [4], from the timing [5] ("pulsar timing") and the observed mass distributions [6] of binary pulsars ("pulsar mass"), helioseismology [7], and lunar laser ranging (LLR) [8].

satisfied (neglecting cosmological redshift)

$$\left(\frac{\pi G_o M_o f}{c^3}\right)^{1/3} = \left(\frac{\pi G_s M_s f}{c^3}\right)^{1/3}, \tag{2.5}$$

Thus, when $G_s \neq G_o$, the estimated total mass of the binary from this template matching (and hence the masses $m_{o,1}$ and $m_{o,2}$ of the neutron stars) will be biased.

$$M_o = \frac{G_s}{G_o} M_s \implies m_o = \frac{G_s}{G_o} m_s, \tag{2.6}$$

where m_s and m_o are the actual and estimated masses of the neutron stars, respectively. We have omitted the subscripts 1, 2 for simplicity. Due to the cosmological expansion, GWs will be redshifted. The effect of this can be captured by applying the redshift factor $(1 + z)$ to the masses, i.e., by replacing m by $m(1 + z)$ [50]. Due to this effect, Eq.(2.6) will be modified to

$$m_o = \frac{G_s}{G_o} \left(\frac{1 + z_s}{1 + z_o}\right) m_s, \tag{2.7}$$

19

where z_s is the true cosmological redshift of the source and z_o is the estimated redshift — either from a direct electromagnetic observation of the host galaxy or by converting the luminosity distance estimated from the GW observation, assuming a cosmology. Using Eq. (2.3) in Eq. (2.7) gives the maximum and minimum values of observable masses

$$m_o^{\text{max, min}} = m^{\text{max, min}} (G_s/G_o)^{-1/2} \left(\frac{1 + z_s}{1 + z_o} \right). \qquad (2.8)$$

If the redshift is accurately known from an electromagnetic observation (as in the case of the neutron star merger event GW170817 [29]), then $z_o = z_s$, and Eq.(2.8) reduces to

$$m_o^{\text{max, min}} = m^{\text{max, min}} (G_s/G_o)^{-1/2}. \qquad (2.9)$$

That is, when $G_s \neq G_o$, the allowed range of neutron star masses (as measured from GW observations) will be different from the range m^{min} — m^{max}. This is shown by the gray region in Fig. 2.2. If G_s has a significant deviation from the current value G_o, the observed values of neutron star masses (from GW observations, shown as horizontal bands in Fig. 2.2) would have gone out of the allowed range of neutron star masses (gray region). Hence such large deviations are ruled out by current GW observations.

Even if the redshift is not known from electromagnetic observations, the luminosity distance estimated from GW observations can be used to infer the redshift assuming a cosmological model. However, if G varies over cosmological time, then the inferred redshift will have a bias because the cosmological model uses the current value, G_o, of G. The allowed mass range of neutron stars should be made larger to accommodate this effect (see the parenthetical ratio of redshifts in Eq.(2.8)). This effect is negligible for GW190425 thanks to its relatively low distance; however we will need to consider this effect for BNS observations from large distances (for e.g., by the next generation detectors).

2.4 Results

Figure 2.2 summarizes the constraints on the variation of G between the epoch of the merger of the neutron stars and the present epoch, obtained from the two putative BNS observations by LIGO and Virgo, GW170817 [28] and GW190425 [2]. The horizontal axis corresponds to the assumed value of G at the epoch of the merger, denoted by G_s (in units of the current value G_o), and the vertical axis corresponds to the neutron star mass m_o (in units of solar mass) that we would estimate from GW observations. The tilted gray regions show the allowed range of the observed neutron star mass; i.e., $m^{min} (G_s/G_o)^{-1/2}$ to $m^{max} (G_s/G_o)^{-1/2}$, where $m^{min} = 0.09 M_\odot$ and $m^{max} = 4 M_\odot$. The two horizontal bands correspond to the measured value of the neutron star masses (90% credible regions of the marginalized posteriors on the component masses from LIGO-Virgo observations [28, 2]).

When $G_s \lesssim 4 \times 10^{-3} G_o$ or when $G_s \gtrsim 9 G_o$, the observed mass range of the neutron stars in GW170817 will go out of the predicted mass range. Thus, the fractional deviation $\Delta G/G_o :=$ $(G_s - G_o)/G_o$ in gravitational constant is constrained to be $-0.996 \lesssim \Delta G/G_o \lesssim 8$. Similarly, GW190425 constrains G_s to be in the range $-0.997 \lesssim \Delta G/G_o \lesssim 5$. Note, however, that G_s in different observations will refer to different epochs (that of the individual mergers).

If we know the time Δt elapsed between the merger and the GW observation, we can compute an average rate of change of the G during this period: $\dot{G}/G_o \simeq \Delta G/(G_o \Delta t)$. Since the luminosity distance to the source is measured, by assuming a cosmology, we can compute the time taken by the signal to reach the observer from the source [3]. GW170817 and GW190425 provide the constraints $-7 \times 10^{-9} \text{ yr}^{-1} \lesssim \dot{G}/G_o \lesssim 5 \times 10^{-8} \text{ yr}^{-1}$ and $-4 \times 10^{-9} \text{ yr}^{-1} \lesssim \dot{G}/G_o \lesssim 2 \times 10^{-8} \text{ yr}^{-1}$, respectively. These are plotted in Fig. 2.3, along with similar constraints obtained from other astronomical observations.

---

3. Note that a time varying G will also change the cosmology in a non-trivial manner, and hence the GW propagation time. Naively, since Friedmann equations give $H_0 \propto \sqrt{G}$ and $\Delta t \approx d_L/c \times (1 - H_0 d_L/c)$ for low d_L a factor of ~ 10 increase in G will change the Δt by a $\sim 10\%$ for the events we analyze. Hence, we choose to neglect it. It should be noted that this estimate does not consider G as a dynamical field in the problem, which will have to be done for any realistic time-varying G cosmology. We assume standard values for cosmological parameters as quoted in [132].

The proposed XG detectors will detect millions of BNS mergers out to cosmological distances [45]. These will include binaries with neutron star masses close to their theoretical upper/lower limits, providing tight constraints on the value of G at the corresponding cosmological epochs. In order to characterize the expected constraints from such observations, we simulate populations of neutron star mergers assuming three different mass distributions. The first is uniform in component masses in the range $1 - 3M_\odot$; the second [10] and third [9] are based on observed Galactic binary pulsars. We assume a 10 year observing run of a network of two Cosmic Explorer [43] detectors at the LIGO Hanford and Livingston sites, and an Einstein Telescope [133] at the Virgo site. Using the redshift distribution from [45] and assuming a local merger rate of 320 Gpc^{-3} yr^{-1} [134], this will amount to ~ 2.5 million detections, out to redshift of 1.7.

We assume that $\sim 1\%$ of these mergers will produce detectable short gamma-ray bursts [135], which will enable a direct measurement of source redshifts z_s using follow-up observations. This allows us to use Eq. (2.9) instead of Eq. (2.8). We estimate the expected errors on measuring the component masses of these 25,000 binaries using the GWBENCH [136] code. The best constraints on $\dot{G}/G_0$ from different cosmological epochs (bins of 0.096 Gyr) are plotted in Fig. 2.4 as a function of lookback time. For this, we assume a more optimistic choice of $1 - 3M_\odot$ for the theoretical mass limits of neutron stars; a conservative choice of $0.09 - 4M_\odot$ will worsen these constraints by a factor of $5 - 10$. As expected, we get the best constraints when the observed mass range span the entire theoretically allowed mass range — for e.g., in the case of the flat mass distribution considered here (also quoted in Fig. 2.3). Over a wide cosmological epoch spanning about 10 Gyr, GW observations will, and perhaps are the only way to, probe the variation of G. [4]

---

4. Even BNS mergers without electromagnetic counterparts can be used to put constraints, assuming specific cosmological models with varying G (e.g, [137]). Note also that multi-band observations (using ground- and space- based detectors) of BBHs are also expected to produce comparable constraints [138].
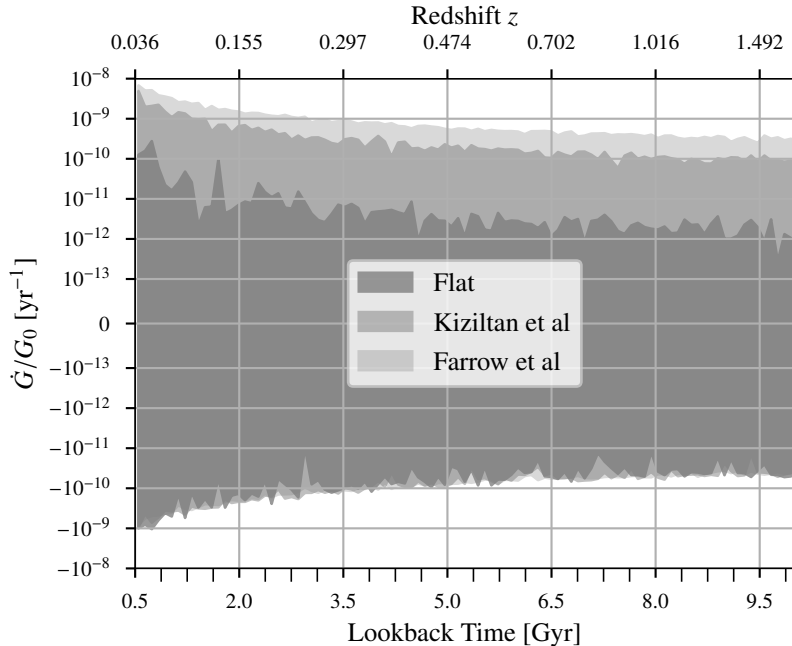
Figure 2.4: Expected constraints on $\dot{G}/G_O$ from 10 year observations of XG GW detectors. We assume three different mass distributions of neutron stars (flat, Kiziltan et al [9], Farrow et al [10]) and that $\sim 1\%$ of the mergers will have a detectable electromagnetic counterpart from which the cosmological redshift can be estimated.

2.5   Summary and outlook

We proposed a method to constrain the evolution of the gravitational constant over cosmic time using GW observations of BNSs, and produced the first constraints with LIGO-Virgo observations (Fig. 2.2). Although these constraints are not as tight as the best available bounds from other measurements, they sample a different cosmological epoch that is not covered by other observations. Additional detections of BNSs would constrain the variation of G at different epochs.

Gravitational-wave observations sampling the extremes of the neutron star masses will further tighten these bounds. For example, the measurement of a high-mass (low-mass) neutron star will constrain the possibility of $G_s > G_O$ ($G_s < G_O$). If there are multiple observations from similar distances (i.e., mergers from similar cosmological epochs), these constraints can be combined, thus further tightening them. Tighter theoretical mass limits for neutron stars (through better understanding of the nuclear equation of state) will also help us to place tighter bounds on ΔG. By

observing a large number of BNSs (some sampling the extremes of the neutron star mass limit), the upcoming generation of GW detectors will be able to tightly constrain the evolution of G over vast cosmological epochs spanning ~ 10 Gyrs (Fig. 2.3).

Note that this test relies on coalescing binaries having at least one neutron star, and is therefore extendable to neutron star - black hole mergers as well, especially if these can be associated with an electromagnetic counterpart. We have assumed that the GW events GW170817 and GW190425 are BNS mergers. Although the possibility of GW190425 being a BBH can not be ruled out [2], the observed electromagnetic counterparts of GW170817 strongly suggests that the binary contains at least one neutron star.

In principle, comparison of the predicted luminosity of the electromagnetic counterparts such as kilonovae with observations will also allow us to constrain the time evolution of G. This requires accurate models of the electromagnetic emission from binary mergers, which might become available in the near future.

CHAPTER 3

CAN A BINARY NEUTRON STAR MERGER IN THE VICINITY OF A SUPERMASSIVE BLACK HOLE ENABLE A DETECTION OF A POST-MERGER GRAVITATIONAL WAVE SIGNAL?

3.1   Introduction

Understanding and constraining the neutron star (NS) equation of state (EOS) with observational data is arguably one of the most exciting and high-profile targets of astrophysical research (for a review see, e.g. [139]). Not only does it promise to shed light on the properties and structure of the neutron star, but it also enables a probe of matter at its most extreme densities, currently irreplicable in human-made laboratories (for a review see, e.g. [140]). Electromagnetic (EM) observations of NSs can provide invaluable data on the NS-EOS, either via detections of periodic radio pulses from spinning NSs [141], or via highly sensitive spectroscopy of soft X-rays carried out by the Neutron Star Interior Composition Explorer (NICER) [142, 143].

Nevertheless, perhaps the most direct probe of the NS EOS would be enabled by GW observations of compact binary coalescences (CBCs) containing at least one NS. The GWs from their inspirals could contain imprints of the degree of tidal deformation of the NS(s), which in turn would allow constraints on the NS EOS see, e.g. [144] and references therein. Furthermore, the shape of the BNS postmerger signal could also enable an EOS model selection, since, for example, the location of the postmerger peak frequency is EOS dependent [145]. The postmerger signal could also contain information on the evolutionary path of the merged binary; depending on the mass of the compact binary and the EOS of the NS, the merged object could either be a black hole (BH) or a heavy (hypermassive or supramassive) unstable NS [146] which subsequently collapses to a BH after a period of time (which is also EOS dependent) (see Ref [147] and references therein).

Detecting the postmerger signal therefore promises to open a treasure-trove of astrophysical riches. Unfortunately, the current sensitivity band of the LIGO-Virgo detectors does not encom-

pass the high frequency regime necessary to detect the postmerger signal [148, 149]. Thus, even though this GW detector network has detected over ninety CBCs (across three observing runs) of which a handful have been BNS detections [150, 151, 152, 34, 153, 154], the postmerger signal remains hidden deep within noise. In fact, even GW170817, the very first and loudest BNS merger [28], did not contain a postmerger signal that was detectable to the LIGO-Virgo-GEO network [155]. Furthermore, future planned upgrades to this network (A+ [148], Voyager [156]) will also be insensitive to postmergers beyond $O(1 - 10\text{Mpc})$ [145].

Arguably, the best bet to observe a postmerger signal in the next decade is to construct a high-frequency detector such as the proposed Neutron Star Extreme Matter Observatory—or NEMO [157] for short—even at the expense of a loss of sensitivity at the lower frequency end. The lower frequency piece of the GW would be captured by the other (LIGO-Virgo-KAGRA) detectors in the network. However, the concept for NEMO-like detectors are in the early stage of their development. Alternatively, a XG detector network consisting of two Cosmic Explorers [43] and one Einstein Telescope [158] could also detect the postmerger. Nevertheless, these detectors may struggle to see the postmerger GWs coming from distances of $O(10 - 100 \text{ Mpc})$ or farther [145, 147].

In this work, we consider a scenario in which a postmerger signal would be detectable, even in the absence of a high-frequency detector. If a BNS merger were to occur in the vicinity of a SMBH, then the gravitational redshift produced by the potential of the SMBH, as well as the Doppler redshift due to the BNSs proper motion around the SMBH (assuming it has a velocity component pointing radially away from the Earth [1]), could effectively "stretch" the postmerger signal into the band of the detectors. At least two mechanisms have been proposed in the literature to deliver a compact binary merger in the vicinity of an SMBH, even near its innermost stable circular orbit (ISCO). One involves the existence of migration traps [159], while the other pertains to tidal capture [160, 161].

---

1. Strictly speaking, in curved spacetime, relating redshift to proper motion of the source requires detailed, ray-tracing calculations. Here, we assume that the curvature is sufficiently small (binary orbits are sufficiently far away from the SMBH) so that the Doppler shift can be computed by projecting the velocity vector on to the line of sight.

Nuclear star clusters are expected to be sites where compact binary mergers occur in significant numbers. The mechanisms that drive these mergers in the vicinity of the SMBH include mass segregation [162, 163], tidal capture [161], and tidal perturbation [164]. Among these mechanisms, tidal capture could enable mergers close to the SMBH, even within $10R_s$, where R_s is the gravitational (Schwarzschild) radius of the SMBH. Some authors have even speculated that a subset of the heavier masses observed in LIGO-Virgo's BBHs can be attributed to gravitational and Doppler redshifting suffered by their GWs, since they could have merged in the vicinity of SMBHs via tidal capture [160].

Several studies have also suggested that the accretion disk in an active galactic nucleus (AGN) could contain a large number of compact objects. Some of them could have been snared by the accretion disk due to repeated collisions with it [165, 166, 167, 168], while others could have become compact objects from massive stars residing in the outer parts of the disk [169, 170, 171].

These compact objects could then form binaries, and merge within Hubble time, due to interactions with each other or with the gas-rich environment. On the other hand, the interaction of the binary with the surrounding gas would cause it to migrate towards the central SMBH powering the AGN. However, opposing wind-driven torques near the ISCO of the SMBH produces a migration trap, where the binary could live out the remainder of its life and merge [159].

AGNs have been seriously considered in the literature as potential sites for the mergers detected by LIGO-Virgo. Recent work suggests that, under certain assumptions, as many as 50% of the BBHs detected in the third observing run (O3) could be associated with AGN disks [172]. The SMBHs driving the AGNs enable mass segregation [163] that allow stellar mass BBHs to merge in the vicinity of the SMBHs, while their heavier masses make them less likely to acquire the necessary escape velocity to be ejected (kicked) out of the AGN.

On the other hand, BNS mergers in AGN disks are expected to contribute a smaller fraction to the total BNS merger rate than the corresponding contribution of BBH mergers to the total BBH merger rate. AGNs are therefore not expected to be the dominant sites for LIGO-Virgo's BNS mergers. This can be attributed at least in part to mass-segregation pushing NSs away from the

SMBHs, and their lighter masses allowing them to acquire the necessary velocities to get ejected out of the AGN. Nevertheless, the BNS merger rate within AGNs could be up to ~ 4 times as large as the BBH merger rate [172]. From [173], the BBH merger rate in AGNs can be as high as $\sim 20 \, \mathrm{Gpc}^{-3}\mathrm{yr}^{-1}$, which places a BNS merger rate upper limit of $\sim 80 \, \mathrm{Gpc}^{-3}\mathrm{yr}^{-1}$. Optimistically, then, in a 10-year XG era, $\mathcal{O}(1000)$ BNS mergers in AGNs could be detected within 1000 Mpc. Interaction of the BNSs with the gas-rich environment, and mechanisms such as tidal capture, could then cause a small fraction of them to merge in the vicinity of the SMBH, even inside the last migration trap close to the ISCO of the SMBH [159] [2].

It is therefore reasonable to speculate that a handful ($\mathcal{O}(1-10)$) of BNSs could merge close to SMBHs, and their GWs redshifted sufficiently to present a detectable postmerger signal in a ten-year XG era. We show that such a GW event would allow a significantly improved postmerger SNR, constraint on the postmerger peak frequency (provided the degree of redshifting could be acquired using independent means), and EOS model selection.

The rest of the chapter is organized as follows. Section 4.2 delineates the redshifting of the detector frame mass and luminosity distance estimates, the computation of the postmerger SNR, a phenomenological model of the postmerger signal and inference of the peak frequency, and an approximate EOS (Bayesian) model selection scheme. Section 4.4 summarizes the results, highlighting the improvements due to gravitational and Doppler redshifting. Section 4.5 discusses ways of inferring the true peak frequency from the redshifted peak frequency, the limitations of this work, and potential avenues for future work.
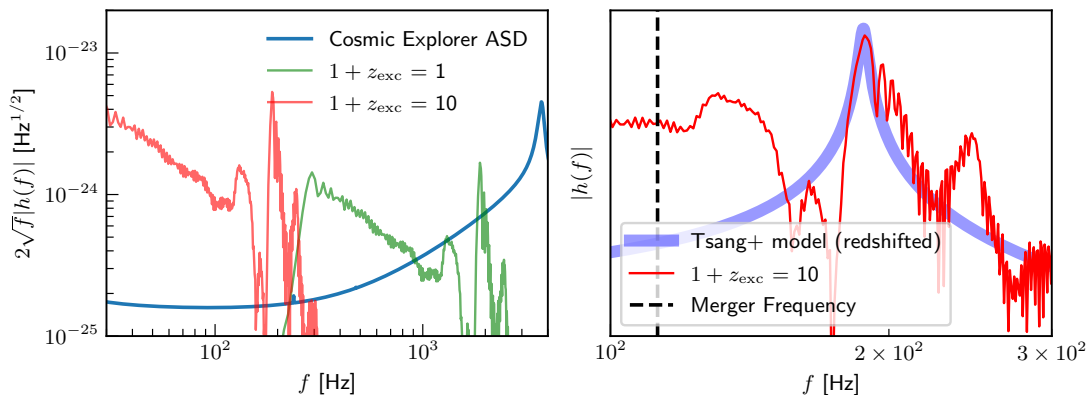
Figure 3.1: (Left) Illustration of the the redshifting and the "dragging" of the postmerger into the sensitive band of the detector. We use the frequency-domain GW strain from the BAM:0098 numerical relativity simulation [11] of the Computational Relativity (CoRe) database [12] for a source located at d_L = 5000 Mpc (*ie* $1 + z_{cos}$ = 1.78). The green line corresponds to a BNS merger with $1 + z_{exc}$ = 1 *i.e.* it incurs no extra redshift due to gravitational/Doppler redshifting. We note that most of the postmerger signal is hidden under the expected noise amplitude spectral density (ASD) of the XG Cosmic Explorer detector (blue solid line). However, when $1 + z_{exc}$ = 10 (red line), the signal gets pulled into band and most of the postmerger is now above the noise ASD. (Right) Illustration of the match between the numerical simulation and the phenomenological model from [13]. The BAM:0098 waveform is plotted in the frequency domain (red line), assuming $1 + z_{exc}$ = 10. We plot Eq. (3.5) with f_{peak} = 3340 Hz, f_{spread} = 31 Hz and $1 + z$ = 10 (blue line). We also show the merger frequency calculated using the analytical expression in Eq. (3.3) (vertical dashed black line) and use it to denote the start of the postmerger regime. The model captures the peak frequency and the spread in the frequency domain as expected.

3.2 Motivation and Methods

3.2.1 Redshifting of the GW signal

GWs from CBCs in the neighbourhood of SMBHs will undergo three distinct kinds of redshifts. These are:

1. the cosmological redshift due to the expansion of the universe

2. the Doppler redshift due to the motion of the BNS around the SMBH (if it has a velocity component that points radially away from the observer)

3. the gravitational redshift due to the GWs climbing out of the SMBH's potential well,

Each of these redshifts dilates the time at the location of the CBC, as measured by a distant observer. As a result, the frequency of the GWs reaching the observer is reduced with respect to the frequency produced at the CBC's location. Since frequency is degenerate with the total mass of the system, the inferred component masses will be an overestimate of the true (source-frame) masses by an amount that depends on the degree of redshifting.

In general, computing the total redshift of such GWs is complicated, especially since it would require a single coordinate system to describe the metric in the vicinity of the SMBH as well as the metric of the expanding universe. Following [160], we approximate the total redshift to be a product of the cosmological redshift (estimated assuming standard cosmology [174]), and an "excess" redshift due to the geodesic motion of a test particle in the Kerr metric [175] of the SMBH:

$$1 + z_{\text{tot}} = (1 + z_{\text{cos}})(1 + z_{\text{exc}}) \tag{3.1}$$

Note that, we are concerned exclusively with the postmerger signal of a BNS whose wavelength (even after redshifting), is several orders of magnitude smaller than the gravitational radius

---

2. The BNS merger rate in the vicinity of the SMBH and in the last migration trap is inferred by making use of estimates of BBH merger rates in those regimes, and assuming that the ratio of the rates of BNS and BBH mergers is maintained throughout the AGN (see Section 4.5). However, such an estimate would likely have large uncertainties and must be interpreted as an optimistic upper limit.

of the SMBH ($M_{\text{SMBH}} > 10^6 M_\odot$). We can therefore estimate the gravitational redshift in the short-wavelength limit (as with light) [176].[3] The redshifting of the postmerger signal effectively "drags" the postmerger peak towards (or even into) the detector's sensitivity band, thus enabling its detection. This is illustrated in Figure 3.1 (left panel) for an extreme value of the excess redshift.

The inferred redshifted mass (say the chirp-mass), will be changed from its source-frame value to its detector frame value, by $\mathcal{M} \rightarrow \mathcal{M}(1 + z_{\text{tot}})$ [91, 160]. The inferred comoving distance is also biased by the redshifting. With cosmological redshift, this bias provides the luminosity distance d_L [92]. The additional redshift due to gravity and the BNS's proper motion, then results in a biased estimate of the luminosity distance: $d_L \rightarrow d_L(1 + z_{\text{exc}})$ [160].

3.2.2 Postmerger SNR

The prevalent method to search for GW signals of known shape in detector data is matched-filtering [177], where a GW template is cross-correlated with the data to produce a signal-to-noise ratio (SNR) statistic. If the detector noise is both stationary and Gaussian, and assuming that the template is a perfect representation of the signal in the data, then the optimal SNR is given by [178]:

$$\rho = \sqrt{4 \int_0^\infty \frac{\left|\tilde{h}(f)\right|^2}{S_n(f)} df} \tag{3.2}$$

where $\tilde{h}(f)$ is the Fourier transform of the time-domain GW strain template $h(t)$, and $h(t)$ is a linear combination of the two GW polarizations, with coefficients that correspond to the response of the detector to each of the polarizations (often called the antenna pattern functions) [179, 180].

As mentioned earlier, this work restricts itself to the postmerger phase of the BNS merger. The postmerger phase is (in this work) defined to span frequencies $f \in \left[f_{\text{merg}}(1 + z_{\text{tot}})^{-1}, f_{\text{max}} \right]$. We

---

3. We assume $1 + z_{\text{exc}}$ values to be ≤ 5. Values greater than (or even close to) this value are likely to be quite rare, since such redshifts would require mergers close to the ISCO of highly spinning SMBHs. We also neglect the effects of gravitational lensing, which might occur for mergers that happen behind the SMBH with respect to the observer.

use the following analytical fit to calculate the merger frequency of BNSs [181]:

$$Mf_{\text{merg}} = \left(3.3184 \times 10^{-2}\right)\frac{1 + (1.3067 \times 10^{-3})\xi_{3199.8}}{1 + (5.0064 \times 10^{-3})\xi_{3199.8}} \quad, \tag{3.3}$$

where $\xi_{3199.8} = \kappa_2^T + (3199.8)(1-4\eta)$. Here, η is the symmetric mass ratio $\eta = (m_1 m_2)/(m_1+m_2)^2$. M is the total source-frame mass of the binary, which, for this work, we assume to be (in units of $M_\odot$) $M = m_1 + m_2 = 1.35 + 1.35 = 2.7$. κ_2^T is the effective tidal parameter for the binary at quadrupolar order in the EOB framework[4] [11]. We set $f_{\text{max}} = 4000$ Hz.

3.2.3   A phenomenological postmerger model

A finite number of numerical relativity waveforms that represent certain discrete points in the postmerger parameter space are currently available. However, a sufficiently accurate method to generate postmerger waveforms at arbitrary parameters does not exist at the time of writing. For this work, we follow [13] to construct a simple phenomenological postmerger waveform that effectively mimics the postmerger peak frequency[5]. Specifically, the waveform is modelled as a damped sinusoid in the time domain, which (Fourier) transforms to a Lorentzian. We therefore adopt the following three-parameter ansatz for the frequency domain [13]:

$$\tilde{h}(f) = \frac{c_0\, f_{\text{spread}}}{\sqrt{(f - f_{\text{peak}})^2 + f_{\text{spread}}^2}} e^{-i \tan^{-1}\left(\frac{f - f_{\text{peak}}}{f_{\text{spread}}}\right)} \quad. \tag{3.4}$$

---

4. For equal-mass binaries considered in this work, κ_2^T is related to the oft-used $\tilde{\Lambda}$ parameter [182] by $\tilde{\Lambda} = \frac{16}{3}\kappa_2^T$ [11].

5. There exist other models for the postmerger that capture more of its spectral features [183, 184]. However, we consider this model for its functional simplicity.

The peak frequency is captured by f_{peak}, the width of the postmerger is modelled by f_{spread}, while c_0 is an overall amplitude scaling parameter. Accounting for the redshift z_{tot}, this becomes:

$$\tilde{h}(f) = \frac{c_0 \, f_{spread}}{\sqrt{\left(f(1 + z_{tot}) - f_{peak}\right)^2 + f_{spread}^2}} e^{-i \tan^{-1}\left(\frac{f(1+z_{tot})-f_{peak}}{f_{spread}}\right)} \quad . \tag{3.5}$$

The comparison of this model to a numerical simulation is illustrated in Figure 3.1 (right panel). The model, for a certain choice of parameter values, captures the peak of the postmerger and the spread in frequency as expected. However, it fails to capture other subdominant features in the postmerger.

In this work, we assume this phenomenological model to be the "true" model of Nature, and study the precision with which the dominant postmerger peak can be recovered. However, extracting a realistic postmerger signal from data would require more sophisticated models, to avoid any potential mis-association of a subdominant peak with the dominant peak.

3.2.4 Bayesian parameter estimation

The core of Bayesian parameter estimation is the construction of the posterior distribution $p(\vec{\theta}|d)$ of the parameters $\vec{\theta}$, given the data s and a signal model $h(\vec{\theta})$. Using Bayes theorem:

$$p(\vec{\theta}|s) = \frac{\pi(\vec{\theta})p(s|\vec{\theta})}{p(s)} \quad , \tag{3.6}$$

where $\pi(\vec{\theta})$ is the prior distribution, $p(s|\vec{\theta})$ is the likelihood, and $p(s) := \int \pi(\vec{\theta})p(s|\vec{\theta}) \, d\vec{\theta}$ is the marginalized likelihood, or the *evidence*. If the noise is stationary Gaussian, the likelihood can be written as [185]:

$$\mathcal{L} \equiv p(s|\vec{\theta}) \propto e^{-\frac{1}{2}\langle s-h(\theta)|s-h(\theta)\rangle} \quad , \tag{3.7}$$

where s is the detector strain data, and $\langle \cdot | \cdot \rangle$ represents the noise-weighted inner product:

$$\langle a|b \rangle = 2 \int_{f_{\min}}^{f_{\max}} \mathrm{d}f \, \frac{(a(f)b^*(f) + a^*(f)b(f))}{S_n(f)} \quad . \tag{3.8}$$

Here, $[f_{\min}, f_{\max}]$ is the frequency range over which the inner product is to be evaluated.

It would be germane to mention here that the prior, likelihood, evidence and the posterior, are implicitly conditioned on the assumed physical model used to produce the postmerger, in particular, the NS EOS. For notational simplicity, this has been omitted, but will be explicitly mentioned in the next subsection.

3.2.5   Equation of State Model Selection

A number of NS EOSs have been proposed in the literature. While some of the harder EOSs have been disfavoured by analyses of GW170817 [33], what is the true NS EOS still remains an open question. BNS postmerger detections have the potential to further rule out candidate EOSs.

A comparative analysis that quantitatively determines if one EOS model (say, EOS1) is favored over another EOS model (say, EOS2), involves evaluating a Bayes factor. This factor is simply the ratio of the marginal likelihoods (evidences) under each of two hypotheses - the hypothesis $\mathcal{H}_1(\mathcal{H}_2)$ that the signal in the data known to be a BNS postmerger corresponds to EOS1 (EOS2). The Bayes factor can be evaluated as follows:

$$\mathcal{B}_2^1 = \frac{p(s \mid \mathcal{H}_1)}{p(s \mid \mathcal{H}_2)} = \frac{\int p(\vec{\theta} \mid \mathcal{H}_1)p(s \mid \vec{\theta}, \mathcal{H}_1)d\vec{\theta}}{\int p(\vec{\theta} \mid \mathcal{H}_2)p(s \mid \vec{\theta}, \mathcal{H}_2)d\vec{\theta}} \quad . \tag{3.9}$$

In the absence of postmerger waveform models (for different EOSs) that can smoothly span the domain of the BNS's intrinsic parameters, we resort to a well-known approximation to this Bayes factor. In particular, given that the data s contains a postmerger signal corresponding to EOS1 with intrinsic parameters $\vec{\theta} = \vec{\theta}_1$, this approximation can be evaluated using the optimal SNR and the

fitting factor (FF)[6][186, 187]

$$\ln \mathcal{B}_2^1 \approx (1 - \text{FF})\rho^2 \tag{3.10}$$

where the FF is defined as the noise-weighted inner product (cf. Eq. 3.8) of the waveforms under each of the two hypotheses, maximized over the intrinsic parameters $\vec{\theta}$:

$$\text{FF} \equiv \left\langle h_{\text{EOS1}}(\vec{\theta}) \middle| h_{\text{EOS2}}(\vec{\theta}) \right\rangle_{\max(\vec{\theta})} \tag{3.11}$$

and ρ is evaluated using $h_{\text{EOS1}}(\vec{\theta}_1)$ (cf. Eq. 3.2).

3.3   Results

We use the methods described in Section 4.2 to quantify the improvements gained by the redshifting of the GW signal. We first calculate the SNR of the postmerger signal using the prescription mentioned in Section 3.2.2. We use the numerical relativity simulations BAM:0002 and BAM:0098 [11] from the Computational Relativity (CoRe) database [12]. These assume EOSs 2H [188] and SLy [189] respectively [7], and model the last few orbits of the BNS inspiral, merger, and postmerger phases. The component masses are set to $1.35M_\odot$ and $1.35M_\odot$, and the effective tidal deformabilities are $\kappa_2^T = 436$ and $\kappa_2^T = 73$.

We consider two observing scenarios [190, 156, 191, 192]:

1. *A+*: A future observing run of the LIGO-Virgo-KAGRA network, consisting of 3 LIGO detectors (including LIGO-India [193, 194]), and the Virgo [149] and KAGRA [38] detectors, operating at their A+ sensitivities.

2. *XG*: The XG network, consisting of two Cosmic Explorers [43] located at Hanford and Livingston, as well as one Einstein Telescope [158] (in the L-shaped configuration) located at Virgo's site.

---

6. The extrinsic parameters are semi-independent of the intrinsic parameters, and are assumed to be known for simplicity.

7. 2H and SLy are chosen to be representative of stiff and soft EOSs, respectively.
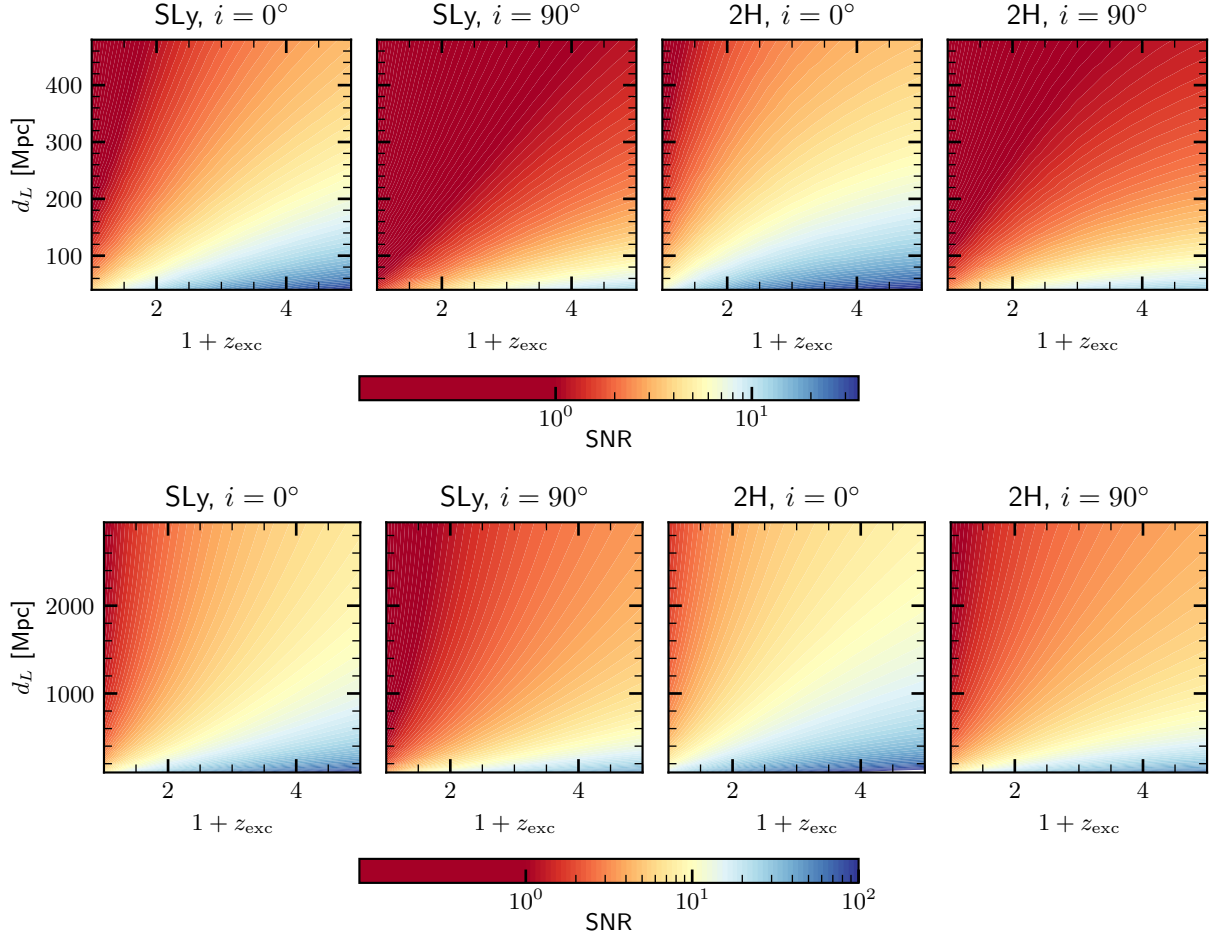
Figure 3.2: Postmerger SNRs for face-on and edge-on binaries for the Advanced LIGO (top row) and Cosmic Explorer (bottom row) sensitivities. As expected, SNR increases with an increase in the $1 + z_{\rm exc}$ and a decrease in the luminosity distance d_L. For aLIGO sensitivity and $1 + z_{\rm exc} = 4$, typical SNRs are ~ 2 (0.2) for face-on (edge-on) binaries. However, for the Cosmic Explorer sensitivity, the typical SNRs for the same value of $1 + z_{\rm exc}$ are ~ 10 (3). We also note that in both cases, the SNR for the case with no excess redshifting is always < 1.

We then calculate the optimal SNR for the postmerger on a grid of excess redshifts $1 + z_{\text{exc}}$ and d_L.

Figure 3.2 shows the results from the SNR calculation for the A+ (top row) and XG (bottom row) scenarios. As expected, we see that the SNR of the postmerger increases with an increase in $1 + z_{\text{exc}}$ and decreases with an increase in d_L.

For SLy, when the binary is face-on *i.e.* inclination $i = 0\,\text{deg}$, the SNRs are all close to 1 or below when there is no excess redshifting, for systems located at 150 Mpc or larger. However, increasing $1 + z_{\text{exc}}$ to a value of 2.5 increases the SNRs to values well above 1, with some being as high as 6 at 200 Mpc. In the case of edge-on binary ($i = 90\,\text{deg}$), without excess redshifting, all binaries at distances > 100 Mpc have postmergers with SNRs below 1. However, a $1 + z_{\text{exc}} = 4$ would provide an SNR of ~ 5 at 100 Mpc.

The situation is more optimistic for the 2H EOS, with $1 + z_{\text{exc}} = 2.5$ providing an SNR of ~ 10 even at 200 Mpc for the face-on binary. The edge-on case has lower SNRs as expected, although larger than such systems with an SLy EOS. Nevertheless, given that detecting the postmerger in A+ requires large excess redshift values, even for distances within 500 Mpc, it seems unrealistic that the postmerger will be detected in A+, and if detected, will likely occur due to the BNS merger being within $\mathcal{O}(10)$ Mpc.

The impact of excess redshifting is more drastic in the XG scenario. Even $1 + z_{\text{exc}} = 2.5$ enables a detection with SNRs of ≈ 10 and ≈ 20 at $d_L = 1000$ Mpc, for the SLy and 2H EOSs respectively, assuming face-on binaries. Edge-on systems can also be detected with SNRs of ~ 5 and ~ 8 for the two EOSs respectively.

Having established the impact of excess redshifting on the detectability of the postmerger signal, we now investigate how this will improve the measurement of parameters related to the postmerger, in particular, the postmerger peak frequency.

We inject the phenomenological model [13] outlined in Section 3.2.3 into a "zero-noise" realization for the detectors, again on a grid of $1 + z_{\text{exc}}$ and d_L. The "zero-noise" realization can be thought of as the most probable realization of the noise, and the error estimates obtained from this realization will be similar to those obtained using non-zero realizations. The model is fitted to the
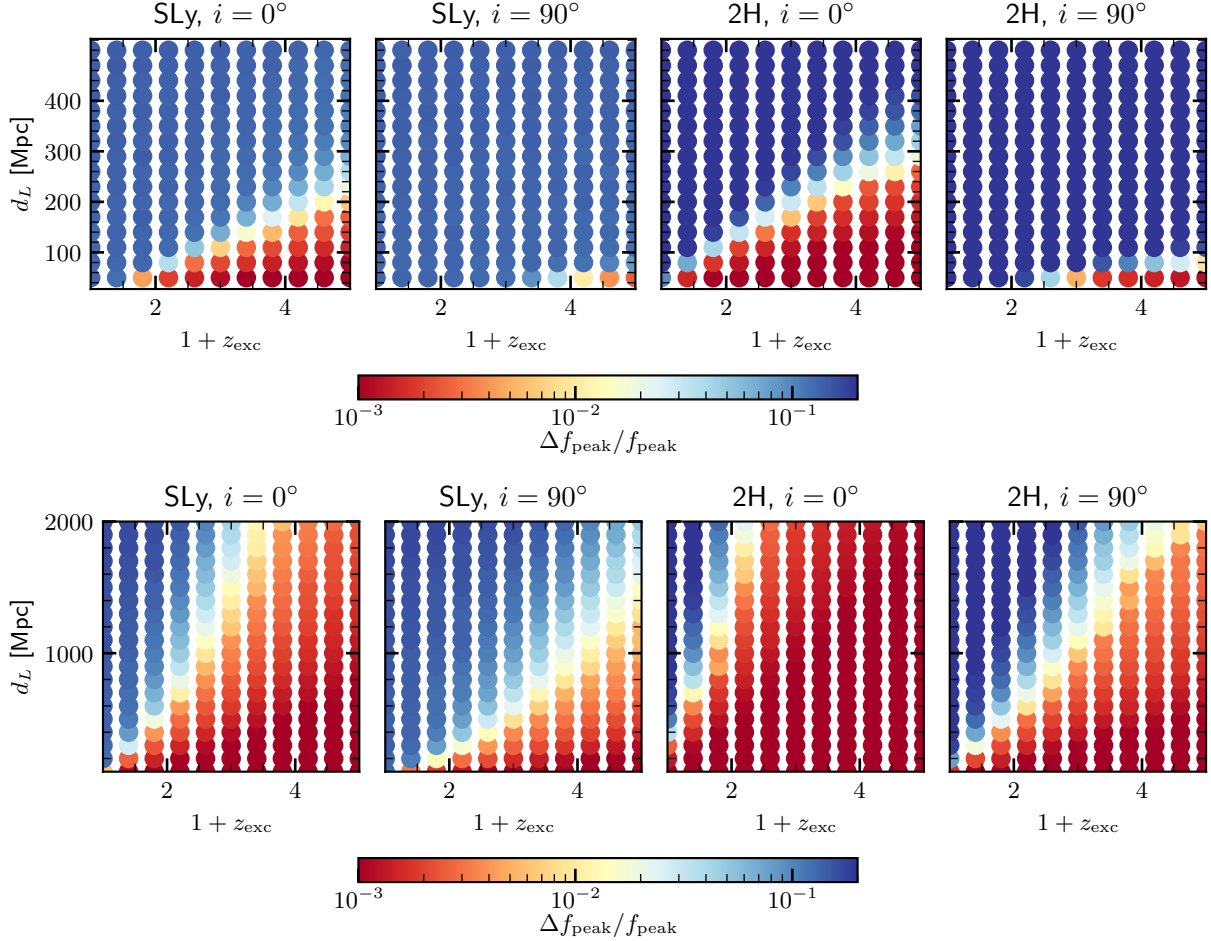
Figure 3.3: Relative errors in the measurement of the peak frequency for A+ (Top Panel) and XG (Bottom Panel), for a range of excess redshifts and luminosity distances. The relative errors reduce with increasing excess redshift, decreasing luminosity distance, and stiffer EOS. In A+, the relative error for all configurations considered is $\sim 10^{-1}$ without excess redshift, even for binaries as close as 40 Mpc, suggesting that the sampling of the posterior on model parameters (in particular, f_{peak}) has returned the prior. On the other hand, even a mild excess redshift of 1.5 can constrain the peak to relative errors of $\sim 10^{-2}$ at 40 Mpc. In XG, an excess redshift of $1 + z_{\text{exc}} = 2.5$ could constrain the peak frequency for the SLy EOS to $\sim 10^{-2}$, at 1000 Mpc, assuming face-on orbits. This constraint is tighter by an order of magnitude for the 2H EOS.

BAM:0002 and BAM:0098 postmerger peaks, and the fits are then used as proxys for the 2H and SLy postmerger waveforms.

For each injection on the grid, we perform Bayesian parameter estimation to find the recovered posteriors and relative error on the peak frequency f_{peak} and the spread in the frequency domain f_{spread}. We fix the sky location and the extra redshift of the binary, thereby varying only f_{peak} and f_{spread} over a flat prior range between $[1800, 2200]$ and $[10, 30]$ respectively. We make use of the open source package `bilby` [195] coupled with the dynamical nested sampler `dynesty` [196] to streamline our parameter estimation analyses.

The results are summarized in Figure 3.3, where the relative error in the measurement of the peak frequency is plotted as a function of excess redshift and luminosity distance. We see that in the A+ scenario, even for BNSs as close as ~ 40 Mpc, the postmerger peak frequency measurement has an error of $\sim 10^{-1}$ without redshifting [8]. On the other hand, even a mild $1 + z_{exc} = 1.5$ gives a relative error of $\sim 10^{-2}$ at the same distance for the face-on BNS. Larger excess redshifts give similar relative errors out to larger luminosity distances. As with the SNRs, the relative errors improve with increasing excess redshifts, decreasing luminosity distances, face-on orientation and stiffer EOS.

In the XG scenario, while the general trends are similar to the A+ scenario, the relative errors are significantly smaller. In particular, $1 + z_{exc} \sim 2$ gives relative errors of $< 10^{-1}$ even at 1000 Mpc for the face-on SLy case, and $< 10^{-2}$ for the 2H EOS. The edge-on BNSs at similar distances would require larger excess redshifts to acquire the same relative errors [9].

Finally, we quantify the improvement in the distinguishability of the EOS using the approximate Bayes factor described in Section 3.2.5 as our discriminator. We use numerical simulations of BNSs with masses $m_1 = m_2 = 1.35 M_\odot$ and the same postmerger waveforms used above pertaining to the same two EOSs, as our fiducial "true" EOSs. We then evaluate Bayes factors ($\mathcal{B}_{EOS}^{SLy,2H}$) following the prescription delineated in Sec. 3.2.5 for a range of different EOSs. The details of the

---

8. Note that errors of 10^{-1} imply that the sampling of the PE posterior has returned the prior.

9. Note that our parameter estimation exercise assumes that the degree of excess redshifting would be known by independent means (which we discuss in Sec. 4.5)
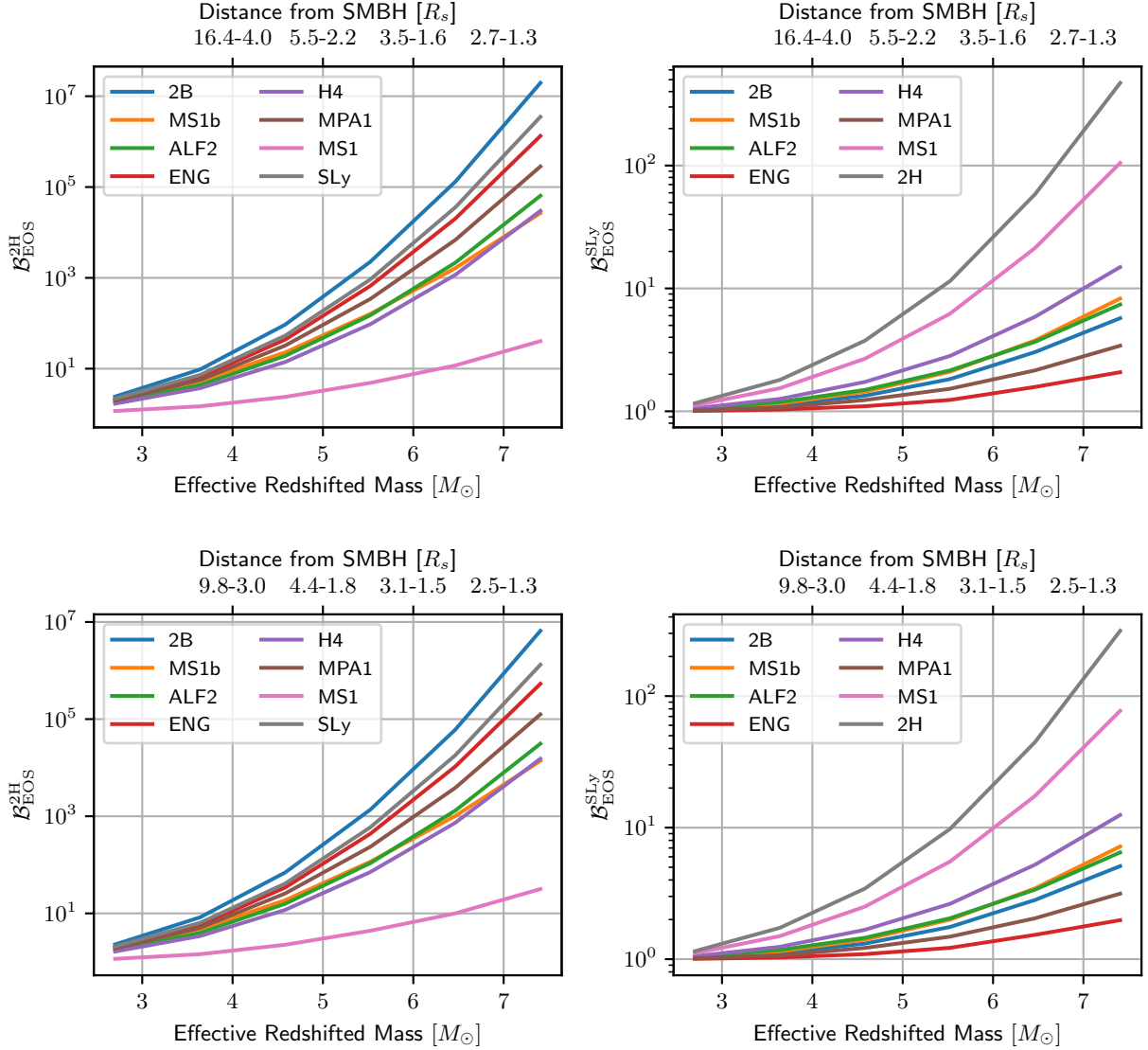
Figure 3.4: EOS model selection Bayes factors, as a function of effective redshifted mass (or, equivalently, the distance of the BNS from the SMBH.). The effective redshifted mass is simply $M(1 + z_{\text{tot}})$. The Bayes factor $\mathcal{B}_{\text{EOS}}^{\text{SLy,2H}}$ assumes that SLy (2H) is the "true" (injected) EOS, and quantifies how well these EOSs can be distinguished from other EOS models. The distance from the SMBH (on the top horizontal axis) pertains to the location of the BNS with respect to the SMBH at which the corresponding redshifted mass in the bottom horizontal axis is measured in the detector frame, assuming a circular geodesic motion in Kerr spacetime (with a spin of $\chi = 0.95$), and standard cosmology. This distance depends on the orientation of the outer binary with respect to the observer. The larger (smaller) value at each tick mark corresponds to purely longitudinal (transverse) motion of the BNS around the SMBH. The top (bottom) panels show the results for face-on (edge-on) BNSs located at 1000(500) Mpc. An effective redshifted mass of $\sim 5 M_{\odot}$ improves the Bayes factor by a factor of $\sim 10 (> 100)$ for the SLy (2H) EOS, and face-on orbits. Such a detector frame mass is achieved at $\sim 6 R_s$ or smaller, depending on the orientation of the outer binary.

40

Table 3.1: List of BNS numerical simulations used in this study, along with their EOSs, effective tidal parameter in the EOB formalism κ_2^T, and the merger frequency calculated using Eq. (3.3). The simulations are part of the CoRe database, and were performed in [11, 19, 20]

CoRe ID	EOS	κ_2^T	f_{merg} [Hz]
BAM:0001	2B	24	2297
BAM:0002	2H	436	1231
BAM:0003	ALF2	138	1742
BAM:0022	ENG	90	1922
BAM:0035	H4	208	1555
BAM:0058	MPA1	114	1825
BAM:0060	MS1	325	1353
BAM:0064	MS1b	287	1408
BAM:0098	SLy	73	2002

numerical simulations used can be found in Table 3.1.

Figure 3.4 shows the results from this investigation, for face-on and edge-on binaries, in the XG era. The face-on binaries are assumed to be at 1000 Mpc, and the edge-on binaries are assumed to be at 500 Mpc. The horizontal axis plots the effective redshifted total mass, which is simply the source-frame mass multiplied by $1 + z_{\mathrm{tot}}$. The vertical axis shows the Bayes factor between the "true" EOS and a host of other EOSs. The upper horizontal axis plots the distance from the SMBH at which the effective redshifted mass is acquired. The SMBH is assumed to have a spin of $\chi = 0.95$, consistent with measured spins of SMBHs [197], and the motion is assumed to be a circular geodesic in the Kerr metric. The two numbers at each x-value correspond to the minimum and maximum distance from the SMBH at which the same total redshift occurs – the minimum corresponds to transverse motion devoid of Doppler redshifting, and the maximum corresponds to longitudinal motion where the velocity vector of the orbiting binary points radially away from the Earth [10].

With an effective redshifted total mass of $\sim 5 M_\odot$, we see that the SLy and 2H EOSs can be

---

10. Note that we only consider those BNSs whose velocities (pertaining to their motion around the SMBH) are assumed to have a component that points radially away from the Earth. There may of course be BNSs whose velocity component points towards the Earth, and the resulting distance from the SMBH may need to be even smaller than the minimum value computed here.

distinguished with $\mathcal{B}^{2H}_{SLy} > 100$ and $\mathcal{B}^{SLy}_{2H} \gtrsim 10$ for $d_L \leq 1000$ Mpc, assuming face-on orbits. [11].
At $d_L = 1000$ Mpc, an effective redshifted total mass of $\sim 5M_\odot$ would need the merger to occur within $\sim 6R_s$ from the SMBH, where R_s is the Schwarzschild radius of the SMBH.

The Bayes factors for edge-on binaries at 500 Mpc are similar to those of face-on binaries at 1000 Mpc, although the smaller luminosity distance reduces the cosmological redshift. Thus, larger excess redshifts are required to produce the same effective redshifted mass. This, in turn, requires mergers to occur relatively closer to the SMBH, as compared to mergers at 1000 Mpc.

Clearly, then, even in the XG era, EOS model selection using postmerger signals out to luminosity distances of $\sim$ 1Gpc requires excess-redshifting, without which, Bayes factors are found to be $\sim$ 1.

3.4   Discussion

3.4.1   Executive summary

Extracting astrophysical information about NS properties from GWs emanated during the post-merger phase of BNS coalescences could prove to be crucial to our understanding of NSs and the nature of matter at extreme densities. The high-frequency noise in current GW detectors makes the detection of such signals almost impossible, except perhaps for unrealistically nearby BNSs. Even XG detectors could struggle to constrain properties of the postmerger—such as its peak frequency—for BNSs located at distances greater than a few tens of Mpc.

In this work, we show that, in the absence of a detector sensitive at $\mathcal{O}(1000)$ Hz, one way to detect the BNS postmerger and constrain its properties, for BNSs located at distances of several tens to hundreds of Mpc, is for the postmerger to be somehow "dragged" into the band of the detectors. Perhaps the only conceivable astrophysical mechanism to achieve this is for the BNS to merge in the vicinity of an SMBH. The gravitational redshift produced by the gravitational field

---

11. Note that even a small decrease in luminosity distance increases the Bayes factor significantly, since the log of the Bayes factor is inversely proportional to the square of the luminosity distance.

of the SMBH, as well as the Doppler redshift due to the BNS's proper motion around the SMBH (assuming that its velocity has a component pointing radially away from the Earth), in addition to the cosmological redshift, could effectively stretch the postmerger GW towards frequencies where ground based detectors are sensitive.

Denoting the combined gravitational and Doppler redshifts as $1 + z_{\text{exc}}$, we vary this quantity from $1 - 5$ to see its effect on the postmerger SNR, the width of the Bayesian posterior on the peak frequency, as well as EOS model selection. We use NR simulations of postmerger signals for non-spinning $1.35 - 1.35 M_{\odot}$ BNSs with the SLy and 2H EOSs to evaluate the optimal SNR for a range of luminosity distances. Using a phenomenological fit to the postmerger waveforms, we evaluate a posterior on the postmerger peak frequency. We then estimate approximate Bayes factors to discriminate between SLy (2H) and other EOSs. We perform these exercises for varying excess redshifts, luminosity distances and both EOSs, as well as two observing scenarios (A+ and XG).

We find that the SNRs, relative errors on the peak frequency, and Bayes factors, improve significantly with increasing excess redshift. In A+, postmergers could optimistically be detectable out to 150 Mpc with $1 + z_{\text{exc}} = 2.5$, and the peak frequency constrained to well within a relative error of 10^{-1}, which would not be the case without this extra redshift. In XG, similar values are found for distances up to 1000 Mpc. In addition, EOS model selection (specifically, the Bayes factor) improves by up to an order of magnitude, at 1000 Mpc, assuming the "true" EOS to be SLy. For a stiffer (2H) EOS, this improvement factor jumps to more than two orders of magnitude.

3.4.2   *Measuring the excess redshift*

While measuring the postmerger SNR, or evaluating the EOS model selection Bayes factors [12], do not require an estimate of $1 + z_{\text{exc}}$, estimating the true value of the postmerger peak requires it, to break the degeneracy between f_{peak} and $1 + z_{\text{tot}}$.

---

12. In this work, the evaluation of the Bayes factors assumes that there is no degeneracy between the total mass of the BNS, and the EOS. In other words, given a postmerger signal pertaining to an EOS and a total mass, no other EOS can exactly replicate all the spectral features of this signal for *any* total mass.

There are at least three methods that could potentially disentangle these two quantities. Perhaps the most comprehensive method would involve a multiband detection. Information about the outer binary's orbit around the SMBH would be acquired by the space-based low-frequency detector LISA [198], while ground based XG detectors would probe the motion of the inner binary. If, in addition, the BNS merger's counterpart was observed, then multiple measurements of the mass of the BNS, as well as the degree of redshifting, would allow for consistency checks and a robust estimate of the true location of f_{peak}.

The second method uses the measurement of tidal parameters from the inspiral to break the degeneracy between masses and redshift. This can be done using quasi-universal relations between the source frame mass and the tidal parameters [199], or combining information of the inspiral with the measurement of the postmerger [200]. However, it must be noted that while these methods are relatively straightforward to employ for an isolated merger, mergers in the vicinity of the SMBH would need to account for the imprint of the BNS's proper motion around the SMBH on the inspiral waveform. This is especially true for the XG scenario, where the inspiral in-band could last for $O(10 - 100)$ minutes.

Yet another method would be to use the BNS merger's counterpart (kilonovae, short gamma-ray bursts) [29, 201] assisted by a galaxy catalog to identify the host galaxy, thereby estimating z_{cos}. Comparing the associated d_L with the measurement of d_L from the merger's GWs would enable an estimate of $1 + z_{\text{exc}}$ (cf. Eq. 3.1). Note, however, that these estimates of d_L would have associated error-bars, which would need to be accounted for when converting from the redshifted postmerger peak to its true value. Thus, the relative errors on f_{peak} quoted in this work can be thought of as lower-limits.

3.4.3   Outlook

We showed in this work that *if* a BNS merger occurred in the vicinity of an SMBH, then the redshifted postmerger could not only be detected, but its spectral properties could potentially be constrained, and the NS EOS could be determined. While we speculated (based on recent simulation

results) in Sec. 4.1 that detecting BNS postmergers redshifted by an SMBH might not be inconceivable (especially in the XG era), the rate of such systems is far from determined. Achieving this would require a full understanding of competing mechanisms in dense stellar environments. While some such as tidal-capture, tidal-perturbation, and migration traps close to the ISCO, could enable BNS mergers near SMBHs, others such as mass-segregation and kick-velocities inhibit the occurrence of such events. Nevertheless, an approximate (and likely optimistic) upper limit can be estimated as follows.

With tidal capture, the rate of stellar mass BBH mergers within $10R_s$ of an SMBH is estimated to be $\sim 0.03\mathrm{Gpc}^{-3}\mathrm{yr}^{-1}$ [160]. On the other hand, rate of mergers within the last migration trap (which can be as close as $6R_s$ from a non-spinning SMBH) is estimated to be $\sim 0.4\mathrm{Gpc}^{-3}\mathrm{yr}^{-1}$ [159]. However, the rate of BNS mergers within $10R_s$ has (to the best of our knowledge) not been computed. An approximate upper limit on this rate can be arrived at using the results of [172], where the upper limit on the ratio of the number of mergers of BNSs to BBHs within AGNs is estimated to be ~ 4. Assuming that this fraction is also maintained in the vicinity of the SMBH, the rate of BNS mergers would be $\lesssim 2\mathrm{Gpc}^{-3}\mathrm{yr}^{-1}$.

From Fig. 3.3, assuming the more realistc SLy EOS, constraining the postmerger peak frequency would be difficult for non-excess-redshifted BNSs located at distances larger than ~ 100 Mpc in the XG era. Thus, using the limits on the rate of BNS mergers acquired from LIGO-Virgo data ($10 - 1700\mathrm{Gpc}^{-3}\mathrm{yr}^{-1}$ [35]), the number of BNSs (per year) that enable such constraints could be anywhere between about $0 - 7$. On the other hand, the peak frequency could be well constrained for BNSs out to distances of ~ 1000 Mpc if they're excess-redshifted. The upper limit on their merger rate, as estimated above, suggests that within 1000 Mpc, $0 - 2$ such events per year could occur. This is a non-trivial fraction of the number of non-redshifted BNS mergers per year within 100 Mpc.

It must however be noted that not *all* BNSs in the vicinity of SMBHs will necessarily be sufficiently excess-redshifted to present a detectable waveform with constrainable spectral properties. In fact, a fraction may even be blue-shifted. Nevertheless, even if $O(1)$ such events were detected

by the end of the 10-year XG era, they could provide unprecedented access to postmergers and their astrophysics.

In principle, the non-detection of redshifted BNS postmergers could provide upper limits on the rate of such events. While admittedly, these rates would be limited to specific masses and EOSs, for which numerical relativity based postmerger waveforms are available, they could enable constraints that could guide models of mergers in the neighbourhood of SMBHs.

CHAPTER 4

PROBING LINE-OF-SIGHT ACCELERATION OF MERGING COMPACT OBJECTS WITH GRAVITATIONAL WAVES

4.1 Introduction

The vast majority of detected CBC events are BBHs [34]. This offers the exciting prospect of constraining their population properties and exploring their formation channels [35]. It has been suggested, however, that a single formation channel cannot explain all the detected BBH events and their source properties [202]. Furthermore, it is often difficult to conclusively identify a given event's formation channel, although statistical arguments can sometimes be made to quantify if one formation channel is preferred over another. Nevertheless, even if such arguments can point to one channel being favored over another, they cannot always conclusively rule out all formation channels at the exception of the statistically preferred one. BNS [28, 2] and neutron star black hole binaries (NSBH) [203] have also been observed with GWs. However, given that their number is barely a handful [34], it is difficult to even make statistical arguments about their provenance, although some preliminary constraints on their source properties have been placed.

It is therefore of considerable interest to ask if there exist any potential signatures or "smoking guns", in the GW waveform itself, that could help identify the astrophysical environment or the formation channel of the CBC that produced it. In this work, we discuss one such generic feature, the signature of accelerated motion of the binary in the gravitational waveform.

Non-rectilinear motion of the compact binary's center-of-mass is expected when the merger happens in a gravitational potential. Though there may be many scenarios where such mergers occur, the resulting motion will depend on the distance of the binary from the center of the potential. Here we focus on CBCs in the vicinity of SMBHs, and discuss the detectability of the resulting accelerated motion with the current and future generation GW detectors as a function of the mass of the SMBH. CBCs in AGN environments [204, 162, 205] would be an example of this binary population, though our method would be sensitive to any mechanism which provides the binary a

detectable line-of-sight acceleration.

Accelerated motion of the centre-of-mass of the CBC, with a non-zero time-varying velocity component along the line-of-sight, would produce a time-varying Doppler shift. This in turn would modulate the inspiral waveform with respect to its standard shape[1]. Previous work [208, 209] showed that a constant line-of-sight acceleration would introduce a term in the post-Newtonian expansion of the phase at the −4PN order. Orbital motion of CBCs around SMBHs will also introduce terms at lower post-Newtonian orders pertaining to higher time derivatives of the velocity (jerk, snap, etc). However, given the finite duration of CBC inspirals in-band, such effects are more difficult to measure, especially for ground-based detectors whose noise power-spectral densities [210] rise sharply at frequencies below ∼ 10 Hz due to seismic activity.

In this work, we place the very first observational constraints on the line-of-sight acceleration of putative BNS mergers GW170817 [28] and GW190425 [2]. We find no evidence of a line-of-sight acceleration. We also study the prospects of constraining this acceleration for a range of component masses of the CBCs, in the fourth observing run of the LIGO-Virgo-KAGRA network [148], the A+ configuration of the LIGO detectors [148], next-generation (XG) detector configurations Cosmic Explorer and Einstein Telescope [43, 158], and the space-based detector DECIGO [211]. We also interpret these constraints in the context of mergers around SMBHs.

Throughout this chapter, we will consider accelerations in units of the speed of light converted to SI units. i.e. a/c [s^{-1}]. Unless otherwise specified, a is the acceleration of the source along the line-of-sight.

4.2 Motivation and Methods

A binary of total mass M_{src} in the source frame will, in general, appear to have a total mass

$$M = M_{\mathrm{src}}(1 + z_{\mathrm{cos}})(1 + z_{\mathrm{dop}}) \tag{4.1}$$

---

1. It is intuitively straightforward to see that these modulations would be identical to those produced by a time-varying gravitational constant G [206]. However, this is not expected to occur on timescales comparable to the duration of the CBC in-band, if at all. See e.g. [207].

in the detector frame. Here, z_{cos} is the cosmological redshift of the source, and $z_{\text{dop}} \approx v/c$ is the Doppler shift induced due to a (constant) line-of-sight velocity v of the source. In addition, if the binary also has a line-of-sight acceleration a/c, the apparent detector frame mass would be

$$M_{\text{det}} = M(1 + a/c \times t) \quad . \tag{4.2}$$

The equation above assumes that $|z_{\text{dop}}| \ll 1$ and acceleration is low ($|a/c| \times t \ll 1$). As is evident, an accelerating source produces a time-varying detector-frame mass which leaves an imprint on the gravitational waveform. If $\Psi_0(f)$ is the full GW phase without acceleration, and $\Psi(f) = \Psi_0(f) + \Delta\Psi(f)$ is the phase including the acceleration, [209] showed that $\Delta\Psi(f)$ is given by:

$$\Delta\Psi(f) = \frac{25}{65536\,\eta^2} \left(\frac{GM}{c^3}\right)\left(\frac{a}{c}\right) v_f^{-13} \quad , \tag{4.3}$$

where $v_f = (\pi GMf/c^3)^{1/3}$, and symmetric mass ratio $\eta = m_1 m_2/M^2$ (m_1 and m_2 being the heavier and lighter mass in the binary respectively). The negative PN contribution also means that, for audio-band ($\sim 10 - 1000$ Hz) GW detectors, a/c would be best measured with BNSs or light BBHs. [212] further derived corrections to the leading order term upto 1.5 PN order, and also forecasted constraints on a/c from stellar mass binaries with LISA.

We extend the calculation of $\Delta\Psi(f)$ to include 3.5 PN corrections to the leading order and obtain

$$
\begin{aligned}
\Delta\Psi(f) = \frac{25}{65536\,\eta^2} \left(\frac{GM}{c^3}\right)\left(\frac{a}{c}\right) v_f^{-13} &\left[1 + \left(\frac{743}{126} + \frac{22}{3}\eta\right)v_f^2 - \frac{64\pi}{5}v_f^3 + \left(\frac{1755623}{84672} + \frac{32633}{756}\eta + \frac{367}{12}\eta^2\right)v_f^4 \right. \\
&- \left(\frac{20807}{210} + \frac{574}{15}\eta\right)\pi v_f^5 + \left\{ -\frac{28907482848623}{35206617600} + \frac{9472}{75}\pi^2 + \frac{13696}{105}\gamma + \frac{13696}{105}\ln(4v_f) + \left(\frac{3311653861}{1524096} \right.\right. \\
&\left. - \frac{451}{6}\pi^2\right)\eta + \frac{2030687}{18144}\eta^2 + \frac{66287}{648}\eta^3 \right\}v_f^6 - \left(\frac{158992529}{317520} + \frac{1015907}{1890}\eta - \frac{419}{945}\eta^2\right)\pi v_f^7 \bigg], \tag{4.4}
\end{aligned}
$$

where $\eta := m_1 m_2/M^2$ is the symmetric mass ratio of the binary. The full derivation of the Eq. (4.4) is described in Section 4.3.

Astrophysically, a binary can have a non-zero acceleration due to multiple reasons. For example, such acceleration could arise due to a binary's circular orbit around an SMBH [213]. In general, for a spherically symmetric potential $\Phi(r)$, the acceleration $\mathbf{a}(r)$ is given by [214, 215]

$$\|\mathbf{a}(r)\| = \frac{d\Phi(r)}{dr}. \tag{4.5}$$

Specifically, for motion around an SMBH, one can express the line-of-sight acceleration as

$$a/c = \frac{\mathbf{a}(r) \cdot \hat{\mathbf{n}}}{c} = 4.65 \times 10^{-12} \left(\frac{M_{\mathrm{BH}}}{10^{10} M_{\odot}}\right) \left(\frac{r}{1\mathrm{pc}}\right)^{-2} \cos\theta \ \mathrm{s}^{-1} \tag{4.6}$$

where r is the distance from the centre of the potential, M_{BH} is the mass of the SMBH, and θ is the angle that the acceleration vector makes with the line-of-sight vector $\hat{\mathbf{n}}$. In our convention, $\cos\theta = 1$ (i.e. $\theta = 0$) means that the acceleration vector is pointed away from the observer. Since the GW phase only allows for a measurement of a/c, one can only constrain the quantity $M_{\mathrm{BH}} \cos\theta / r^2$ with GW observations.

4.3 Derivation of the GW phase and amplitude correction

Here we describe the steps required to compute the corrections to the phase and amplitude of the Fourier domain waveform due to the time-dependent Doppler shift caused by the line-of-sight acceleration of the binary. While the original waveforms (without the Doppler shift) are generated using either the IMRPhenomD or IMRPhenomPv2_NRTidal approximant, we use the non-spinning 3.5PN waveforms to compute the Doppler shift, as we expect their accuracy to be sufficient for our purpose.

Let $z_l = \Gamma t_o$ be the (time-dependent) redshift due to the line-of-sight acceleration of the binary of total mass M, where $\Gamma = a/c$, a is the line-of-sight acceleration, and t_o is the observation time. Hereon, we will be working in $G = c = 1$ units. Let us further define $v_u = (\pi M f_u)^{1/3}$, where f_u is the unperturbed Fourier frequency, and let f_o be the Doppler shifted Fourier frequency.

Then, for $\Gamma t_o \ll 1$,

$$f_u = f_o(1 + z_l) \quad : \quad \text{redshift}, \tag{4.7}$$

$$dt_u = dt_o/(1 + z_l) \quad : \quad \text{time dilation} \tag{4.8}$$

$$v_u = v_o(1 + z_l)^{1/3} \tag{4.9}$$

where $v_o = (\pi M f_o)^{1/3}$. We can further write:

$$\frac{dv_u}{dt_u} = (1 + \Gamma t_o)^{4/3}\left(\frac{dv_o}{dt_o} + \frac{\Gamma v_o}{3}\right) \quad \Rightarrow \quad \frac{dv_o}{dt_o} = -\frac{\Gamma v_o}{3} + (1 + \Gamma t_o)^{-4/3}\frac{dv_u}{dt_u} \tag{4.10}$$

Under the stationary phase approximation (SPA), $\frac{dv_u}{dt_u}$ is given by Eq. (3.6) of [130] with v replaced by v_u and v by the symmetric mass ratio η. Substituting this relation in Eq. (4.10) together with v_u from Eq. (4.7), we get $\frac{dv_o}{dt_o}$ in terms of v_o and z_l. Note that z_l still has a factor of t_o. Hence as a next step, we use the relationship between t_o and v_o, which is given by[2] Eq. (3.8b) of [130], to get $\frac{dv_o}{dt_o}$ in terms of v_o and Γ. In the final step, we invert this equation to get $\frac{dt_o}{dv_o}$.

Integrating $\frac{dt_o}{dv_o}$ in the limits $v_o \to v_{lso} \equiv (\pi M f_{lso})^{1/3}$ and $v_o \to v \equiv (\pi M f)^{1/3}$, where $f_{lso} = \frac{1}{6^{3/2}\pi M}$ and f is the observed frequency of the GW, we get (in geometrized units):

$$
\begin{aligned}
t - t_c = &-\frac{5M}{256\eta}v^{-8}\bigg[1 + \left(\frac{743}{252} + \frac{11}{3}\eta\right)v^2 - \frac{32\pi}{5}v^3 + 2\left(\frac{3058673}{1016064} + \frac{5429}{1008}\eta + \frac{617}{144}\eta^2\right)v^4 - \left(\frac{7729}{252} - \frac{13}{3}\eta\right)\pi v^5 \\
&+ \left\{-\frac{10052469856691}{23471078400} + \frac{128}{3}\pi^2 + \frac{6848}{105}\gamma + \left(\frac{3147553127}{3048192} - \frac{451}{12}\pi^2\right)\eta - \frac{15211}{1728}\eta^2 + \frac{25565}{1296}\eta^3 + \frac{6848}{105}\ln(4v)\right\}v^6 \\
&- \left(\frac{15419335}{127008} + \frac{75703}{756}\eta - \frac{14809}{378}\eta^2\right)\pi v^7 + \frac{65\Gamma M}{1536\eta}v^{-8}\left\{1 + \frac{22}{13}\left(\frac{743}{252} + \frac{11}{3}\eta\right)v^2 - \frac{128}{13}\pi v^3 + \left(\frac{1755623}{122304} + \frac{32633}{1092}\eta\right.\right. \\
&+ \left.\frac{1101}{52}\eta^2\right)v^4 - \left(\frac{83228}{1365} + \frac{4592}{195}\eta\right)\pi v^5 + \left\{-\frac{2274117187691}{5029516800} + \frac{66304}{975}\pi^2 + \frac{13696}{195}\gamma + \left(\frac{3311653861}{2830464} - \frac{3157}{78}\pi^2\right)\eta\right. \\
&+ \left.\left.\frac{2030687}{33696}\eta^2 + \frac{35693}{648}\eta^3 + \frac{13696}{195}\ln(4v)\right\}v^6 - \left(\frac{158992529}{687960} + \frac{1015907}{4095}\eta - \frac{838}{4095}\eta^2\right)\pi v^7\right\}\bigg]
\end{aligned}
\tag{4.11}
$$

---

2. The reason behind using v_o instead of v_u is the presence of Γ with t_o in z_l and using v_u would have made it second order in Γ.

where all of the terms containing v_{lso} are just constants and have been absorbed in t_c (time at the coalescence).

Observing that the infinitesimal orbital phase $d\phi$ remains invariant, we can rewrite Eq. (3.3a) of [130] as $d\phi = \frac{v_o^3}{M}\frac{dt_o}{dv_o}dv_o$. Integrating this in the limits same as before, we get:

$$
\begin{aligned}
\phi(f) = {} & \frac{\phi_c}{2} - \frac{v^{-5}}{32\eta}\left[1 + \left(\frac{3715}{1008} + \frac{55}{12}\eta\right)v^2 - 10\pi v^3 + 5\left(\frac{3058673}{1016064} + \frac{5429}{1008}\eta + \frac{617}{144}\eta^2\right)v^4 + \left(\frac{38645}{672} - \frac{65}{8}\eta\right)\pi v^5 \ln\left(\frac{v}{v_{lso}}\right) \right.\\
& - \left\{-\frac{12348611926451}{18776862720} + \frac{160}{3}\pi^2 + \frac{1712}{21}\gamma + \left(\frac{15737765635}{12192786} - \frac{2255}{48}\pi^2\right)\eta - \frac{76055}{6912}\eta^2 + \frac{127825}{5184}\eta^3 + \frac{1712}{21}\ln(4v)\right\}v^6 \\
& + \left(\frac{77096675}{2032128} + \frac{378515}{12096}\eta - \frac{74045}{6048}\eta^2\right)\pi v^7 + \frac{25\Gamma M}{768\eta}v^{-8}\left\{1 + \frac{7}{3}\left(\frac{743}{336} + \frac{11}{4}\eta\right)v^2 - \frac{52}{5}\pi v^3 + \left(\frac{1755623}{112896} + \frac{32633}{1008}\eta\right.\right.\\
& + \frac{367}{16}\eta^2\right)v^4 - \left(\frac{228877}{3360} + \frac{3157}{120}\eta\right)\pi v^5 + \left\{-\frac{5873342252515}{11266117632} + \frac{1184}{15}\pi^2 + \frac{1712}{21}\gamma + \left(\frac{16558269305}{12192768} - \frac{2255}{48}\pi^2\right)\eta\right. \\
& \left.\left.\left. + \frac{10153435}{145152}\eta^2 + \frac{331435}{5184}\eta^3 + \frac{1712}{21}\ln(4v)\right\}v^6 - \left(\frac{158992529}{564480} + \frac{1015907}{3360}\eta - \frac{419}{1680}\eta^2\right)\pi v^7\right\}\right]
\end{aligned}
$$

$$(4.12)$$

where ϕ_c is the phase at the coalescence. Here all of the terms containing v_{lso} have been absorbed in ϕ_c except the log term.

Substituting Eq. (4.11) and Eq. (4.12) in $\Psi(f) = -\pi/4 + 2\pi ft(f) - \phi(f)$, we get the total phase. The correction in the phase is then simply $(\Psi_{acc}(f) - \Psi_{no\,acc}(f) \equiv \Psi(f) - \Psi_{3.5}(f))$, which is given by:

$$
\begin{aligned}
\Delta\Psi(f) = {} & \frac{25\Gamma M}{65536\eta^2}v^{-13}\left[1 + \left(\frac{743}{126} + \frac{22}{3}\eta\right)v^2 - \frac{64\pi}{5}v^3 + \left(\frac{1755623}{84672} + \frac{32633}{756}\eta + \frac{367}{12}\eta^2\right)v^4\right.\\
& - \left(\frac{20807}{210} + \frac{574}{15}\eta\right)\pi v^5 + \left\{-\frac{28907482848623}{35206617600} + \frac{9472}{75}\pi^2 + \frac{13696}{105}\gamma + \frac{13696}{105}\ln(4v) + \left(\frac{3311653861}{1524096}\right.\right.\\
& \left.\left.\left. - \frac{451}{6}\pi^2\right)\eta + \frac{2030687}{18144}\eta^2 + \frac{66287}{648}\eta^3\right\}v^6 - \left(\frac{158992529}{317520} + \frac{1015907}{1890}\eta - \frac{419}{945}\eta^2\right)\pi v^7\right] \quad.
\end{aligned}
$$

$$(4.13)$$

Assuming $\iota = 0$ in Eq. (4.361) of [47] and observing that $\frac{d\Phi}{dt_o} = \omega_{GW} = 2\pi f_o = \frac{2v_o^3}{M} > 0$

52

i.e. $\frac{d^2\Phi}{dt_o^2} = \frac{6v_o^2}{M}\frac{dv_o}{dt_o} > 0$, we find, using the Eq. (4.366) of the same, the amplitude correction [3] (considering the corrections only to the Newtonian order) to be given by:

$$\frac{\mathcal{A}}{\mathcal{A}_{lead}} = 1 + \frac{65\Gamma M}{2048\eta v^8}[1 + \mathcal{O}(v^2)] \tag{4.14}$$

where $\mathcal{A}_{lead}$ is the leading order amplitude and is given by the Eq. (4.369) of the same reference with $\iota = 0$. We have checked that the amplitude correction does not affect our constraints on Γ significantly enough to merit inclusion.

4.4   Results
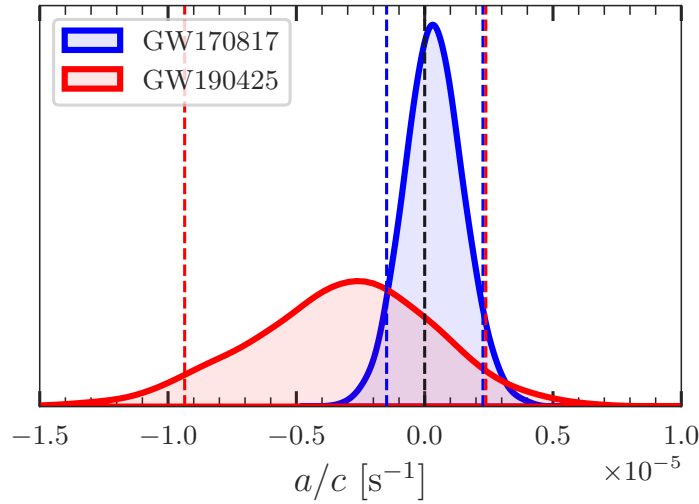
Figure 4.1: Measurement of the line-of-sight acceleration from GW170817 and GW190425. The measurements are expressed as a ratio of the acceleration to the speed of light (a/c) in units of s^{-1}. The solid lines indicate the inferred posterior distribution on a/c, while the vertical dashed lines indicate the edges of the 90% CI. GW170817 yields a stronger constraint (-2.2×10^{-6}—1.5×10^{-6} s^{-1}, 90% CI) as compared to GW190425 (-3.4×10^{-6}—8.4×10^{-6} s^{-1}, 90% CI) due to its low detector frame chirp mass and also high SNR. Both measurements are consistent with zero acceleration.

---

3. We make the substitution $v_o \equiv v$ since we have already assumed the SPA.
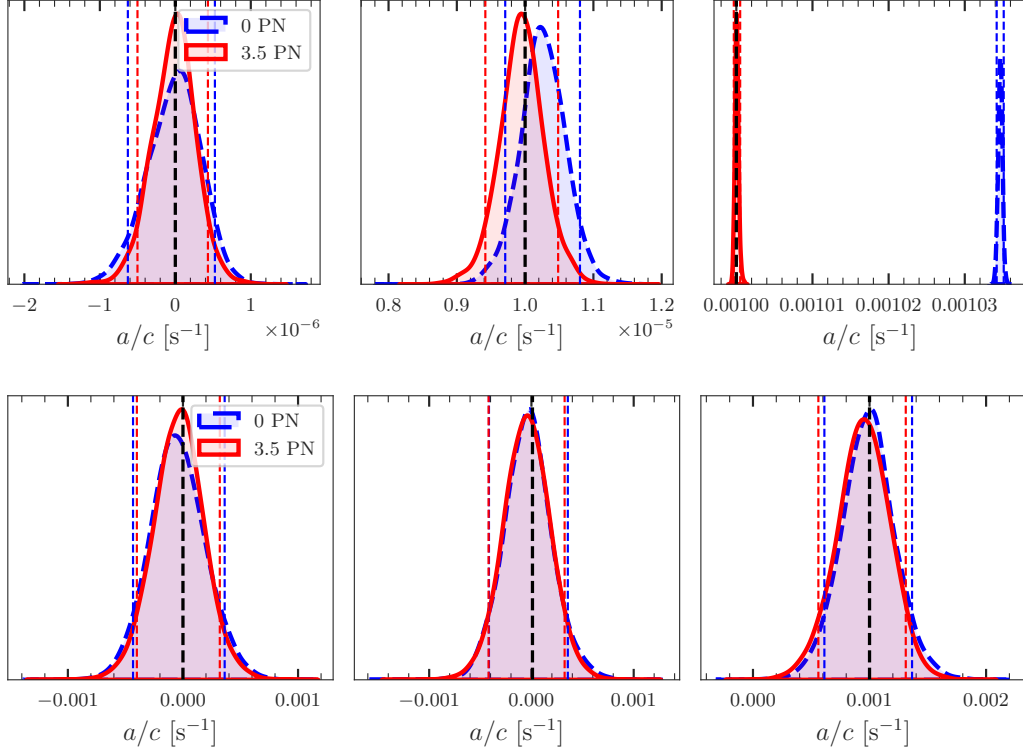
Figure 4.2: Recovered posteriors on a/c from GW170817-like (top) and GW170608-like (bottom) injections in an O4 network. The injected values (from left to right in each row) are 0, 10^{-5}, and 10^{-3} s^{-1}. These are plotted as vertical black dotted lines in each panel. The injected template contains the full phase of Eq. (4.4). The recoveries are done with the full phase (red solid curve) as well as the leading-order phase to check (blue dashed curve) for systematics. The precision in recovery of a/c is $\sim 10^{-7}$ s^{-1} for GW170817, and $\sim 10^{-4}$ s^{-1} for GW170608-like injections. Using only the leading-order phase for recovery does cause systematics in the recovery of the GW170817-like injections, with the bias being worse for larger injected values of a/c. However, recoveries of the GW170608-like injections do not show any significant bias, regardless of the injected a/c.

4.4.1   Constraints from GW170817 and GW190425

We first measure the line-of-sight acceleration from BNS candidates GW170817 [28] and GW190425 [2]. These events are chosen due to their low detector-frame chirp mass, which is ideally suited for a precise measurement of the acceleration. Template waveforms for our analyses are constructed by adding phase corrections due to line-of-sight acceleration (Eq. (4.4)) onto the IM-RPhenomPv2_NRTidal [216] approximant implemented within `lalsuite` [217]. We perform

Bayesian inference on these signals, using low-spin priors[4] of [1] and [2], sampling over all relevant intrinsic and extrinsic parameters including a/c using the dynamic nested sampler `dynesty` [196]. The prior on a/c is assumed to be flat between -10^{-2} s^{-1} and 10^{-2} s^{-1}. We use the parameter estimation packages `bilby` [195] and `bilby_pipe` [218] for streamlining our analyses, while also using the relative binning/heterodyning scheme [219, 220, 221] to speed up our likelihood calculations [222]. The likelihood is calculated in the range 20 Hz to 2048 Hz[5] assuming a sampling rate of 4096 Hz using the publicly-released noise power spectral densities [223], without marginalizing over calibration uncertainties. The inferred posterior on a/c for the two events is shown in Figure 4.1. We find that both events yield a measurement consistent with zero line-of-sight acceleration, with the 90% CI being -2.2×10^{-6}—1.5×10^{-6} s^{-1} for GW170817 and -3.4×10^{-6}—8.4×10^{-6} s^{-1} for GW190425.

Assuming these binaries were orbiting a SMBH we now interpret these measurements as limits on the location of the binary around the SMBH. For this purpose, we directly use Eq. (4.6), and assume that the SMBH mass M_{BH} makes up most of the mass that is enclosed by the binary's orbit a distance r away from the SMBH. In what follows, we quote constraints on r marginalizing over θ assuming a uniform prior on $\cos\theta$. Since GW170817 also had an electromagnetic counterpart, the host galaxy of the merger was confidently identified as NGC 4993 [224], a galaxy that hosts a supermassive black hole of mass $M_{BH} \approx 0.7 \times 10^8 M_\odot$ [225][6]. For this event, we obtain a constraint $r > 12.1$ AU at the 90% credible level (CL). Ideally we should have used the full mass profile of NGC 4993 accounting for its stellar mass and dark matter halo for this constraint; however, since only very high values of acceleration as excluded by our constraints, we can only exclude scenarios where binary lies near the centre of the galaxy i.e. at regions where the acceleration is dominated

---

4. We have verified that using high-spin priors doesn't qualitatively change our results, and only changes the width of the 90% CI on a/c by $\sim 10\%$.

5. Since the corrections due to acceleration are calculated using PN expressions, we should have ideally cut-off our analysis at a frequency beyond which these expressions aren't valid. However, we do not expect this choice to impact our results; the SNR is negligible at high frequencies, and the measurement of a/c is driven by the low-frequency part of the signal.

6. This mass is calculated using the $M - \sigma$ relation of [226] along with NGC 4993's velocity dispersion estimate of $\sigma \approx 170$ km s^{-1} [225].

by the potential of the SMBH[7]. However, from the electromagnetic counterpart, we also know that GW170817 was 1.96 kpc ($\approx 4 \times 10^8$ AU) from the central black hole [225]. Hence, the constraints that we obtain for GW170817 are weaker by several orders of magnitude[8].

Since the host galaxy of GW190425 was not identified, we obtain a SMBH mass-dependent constraint of $r > 7.2 \times (M_{\mathrm{BH}}/10^8 M_\odot)^{1/2}$ AU (90% CL).
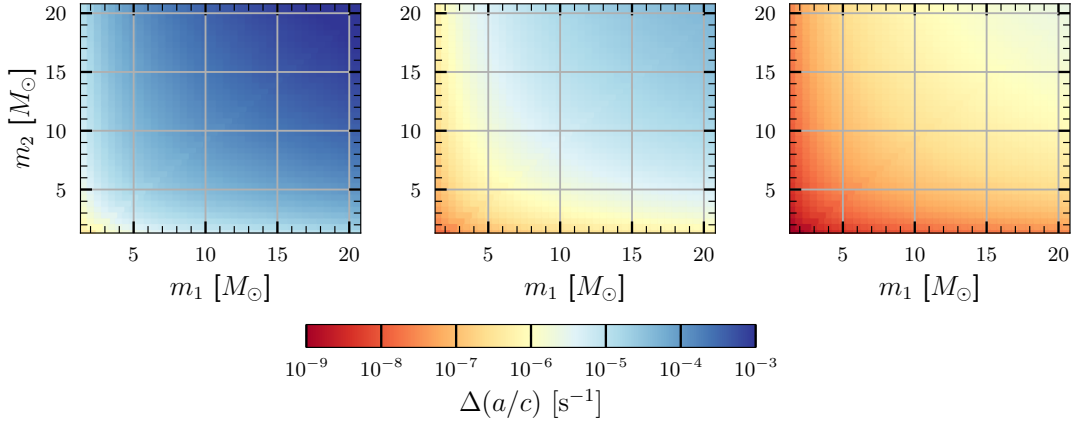
Figure 4.3: 1-σ error in the measurement of a/c for A+ (left), CE (middle), ET (right) detector configurations, over a grid of masses and fixed SNR=10. a/c is best measured with ET since the low-frequency sensitivity is expected to be better as compared to CE. Not surprisingly, lower masses enable better constraints on a/c, because such CBCs spend a longer duration in-band.

4.4.2 Measurement forecasts for future ground-based detector networks

We now outline how the measurement of a/c will improve with future detectors. We first inject a system into simulated gaussian noise assuming the projected sensitivity of LIGO-Virgo-KAGRA network in the fourth observing run (O4)[9], with component masses similar to GW170817 and

---

7. Indeed, redoing this calculation with a detailed potential of NGC 4993 does not change these constraints.

8. In fact, mimicking the mass profile of NGC 4993 by applying an overall scaling to the Milky Way potential MWPotential2014 as defined in galpy [14] to match the halo mass of NGC 4993 ($\approx 2 \times 10^{12} M_\odot$ [225]) gives $a/c \approx 4 \times 10^{-19} \mathrm{s}^{-1}$ at 1.96 kpc. This value of a/c is several orders of magnitude below the detectable values of acceleration at current sensitivities (see Sec. 4.4.2).

9. The network contains LIGO detectors at Hanford and Livingston in USA [36], the Virgo detector in Italy [37], and the KAGRA detector in Japan [38]. The corresponding projected noise power spectral densities are taken from https://dcc.ligo.org/LIGO-T2000012-v1/public. At the time of completion of this work, O4 had not commenced. The sensitivities of the detectors in O4 are lower than what was projected by the PSDs (see https://gwosc.org/detector_status/ for more information).

three different values of $a/c = \{0, 10^{-5}, 10^{-3}\}$ s^{-1}. The injection template contains the IMRPhenomD [227] waveform approximant with the additional contribution from line-of-sight acceleration as in Eq. (4.4). We then recover the parameters of the injected signal assuming the full GW phase using Bayesian inference by injecting the signal into a realization of noise that is zero at all frequencies ("zero-noise" injection). This noise realization means there will be no random scatter added to the posteriors due to the noise, and the recoveries with the correct phase will always have the injected value near the peak of the posterior. On the other hand, any mismodelling could bias the recovery and cause the injected value to be far away from the peak of the posterior. To probe the systematics in the recovery, we also infer the parameters of the signal with templates containing only the leading-order (i.e. -4 PN) term in the acceleration as in Eq. (4.4). Since these are zero noise injections performed to investigate systematics in the recovery of the acceleration due to mismodelling of the GW phase, the recoveries with the correct phase will always have the injected value near the peak of the posterior. On the other hand, any mismodelling could bias the recovery and cause the injected value to be far away from the peak of the posterior. The recovery a/c for all GW170817-like injections[10] is shown in the top row of Fig. 4.2. When using the full phase, all injected values are recovered within the posterior, with the measurement uncertainty being $O(10^{-7})$ s^{-1}. While using the -4 PN phase, the injected value is recovered within the posterior for $a/c = 0, 10^{-5}$ s^{-1}, but the recovery is significantly biased when $a/c = 10^{-3}$ s^{-1}. This illustrates the importance of using an accurate template waveform family while estimating a/c from BNS events. We also repeat the same procedure for injection with GW170608-like masses [228, 150] and plot recoveries in the bottom row of Fig. 4.2. For all the injected values, recoveries with full phase yield consistent posteriors that include the injected value, with the measurement uncertainty being $O(10^{-4})$ s^{-1}. The recoveries with -4 PN phase are consistent with the full phase recoveries since the higher order correction has a smaller effect for heavier masses.

In order to forecast constraints for A+ and next-generation (XG) GW detector networks, we

---

10. The IMRPhenomD approximant does not include tidal corrections to the phase. Although the non-inclusion of tidal corrections is unphysical for BNS events, we do not expect this choice to affect the posteriors on a/c or the biases due to incomplete terms in the phase.

resort to a Fisher matrix based approach. Given a frequency-domain GW waveform template $h(f)$ that depends on a set of parameters $\{\theta_i\}$ in the frequency domain, the elements of the Fisher information matrix Γ can be written as [50]:

$$\Gamma_{ij} = \left\langle \frac{\partial h}{\partial \theta_i} \middle| \frac{\partial h}{\partial \theta_j} \right\rangle \quad , \tag{4.15}$$

Here, $S_n(f)$ stands for the one-sided noise power spectral density (PSD). The covariance matrix Σ of the measurement uncertainties $\Delta\theta_i$ is the inverse of the Fisher information matrix (i.e. $\Sigma = \Gamma^{-1}$). The root-mean-square (rms) uncertainty in the measurement of parameter θ_i marginalized over all other parameters is given by $\sqrt{\left\langle \Delta\theta_i^2 \right\rangle} = \sqrt{\Sigma_{ii}}$.

We use the above prescription to calculate the rms uncertainty in the measurement of a/c. We perform this calculation for three different detector sensitivities:

1. LIGO at A+ sensitivity [148][11] with $f_{\min}$ = 15 Hz.

2. Cosmic Explorer (CE) [43] at its design 40 km compact-binary optimized sensitivity [229] with $f_{\min}$ = 5 Hz.

3. Einstein Telescope (ET) [158] at its design (ET-D) sensitivity [41] with $f_{\min}$ = 2 Hz.

The results for a grid of detector-frame masses at a fixed signal-to-noise ratio (SNR) of 10[12] in each detector are shown in Fig. 4.3. For all configurations, we assume that the binary is non-spinning and has no tidal deformability and that the phase without acceleration is modeled by the TaylorF2 approximant including point-particle phase corrections upto 3.5 PN order (see [130] and references therein). As expected, a/c is best measured for events with low detector frame mass. It is also evident that the measurement uncertainty is lower for XG detectors as compared to A+. The

---

11. The A+ design PSD was taken from https://dcc.ligo.org/LIGO-T2000012-v1/public

12. Note that the breakdown of the linear signal approximation at low SNRs causes the Fisher matrix estimates to become unreliable at those SNRs [230]. We have checked that our setup (with fixed spins and tidal parameters) gives a one-sigma error $\Delta(a/c) = 2 \times 10^{-5}$ s^{-1} for a GW190425 like signal (1.7-1.7 $M_\odot$ signal at SNR=13 assuming the Advanced LIGO PSD). The same quantity calculated using the posteriors from real data (Sec. 4.4.1) is $\Delta(a/c) = 3.5 \times 10^{-5}$ s^{-1}—off only by a factor of 1.75. Thus we do not expect the Fisher estimates to differ significantly as compared to full parameter estimation results SNR > 10.

enhanced low-frequency response of ET results in better constraints as compared to CE. Overall, we find that the best constraint obtained from a 1.4-1.4 $M_\odot$ binary is $O(10^{-9})$s^{-1} for XG detectors, and $O(10^{-7})$ s^{-1} for A+ detectors. Similarly, the best constraint obtained from a 20-20 $M_\odot$ binary is $O(10^{-5})$s^{-1} in XG detectors, and $O(10^{-3})$ s^{-1} in A+ detectors.

For the constraints above (and the ones that follow in Sec. 4.4.3), we do not take into account the effects on the binary waveform produced due to the rotation of the earth. We reiterate that these results are for fixed SNR = 10 and that we have verified that the errors scale as 1/SNR. As such, we do expect to detect both BNS and BBH events with very high SNRs (> 100), especially in XG detectors, and a $O(10^{-10})$ s^{-1} constraint is imminent.
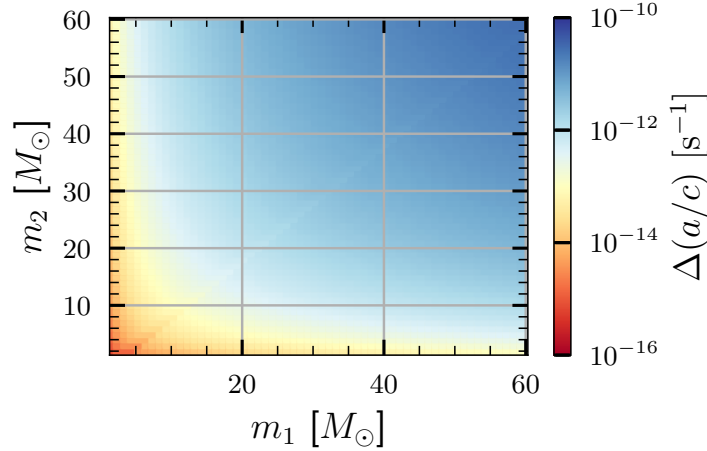
Figure 4.4: 1-σ error in the measurement of a/c in DECIGO over a grid of masses and fixed SNR=10. CBC masses as heavy as $120 M_\odot$ still provide constraints of better than $\sim 10^{-11}$ s^{-1}. Corresponding precision for BNSs is about $5-6$ orders of magnitude better.

4.4.3 *Measurement forecasts for decihertz detectors*

Decihertz detectors like DECIGO [211] can detect chirping stellar mass binaries in the early stages of inspiral out to very high redshifts. Applying the Fisher matrix formalism, we calculate the measurement accuracy of a/c over a grid of masses and fixed SNR = 10, assuming the DECIGO design

sensitivity [231, 232] with $f_{\min} = 0.1$ Hz and $f_{\max} = 1$ Hz[13]. The best constraints are $O\!\left(10^{-16}\right)$ s^{-1} which are seven orders of magnitude better than the corresponding constraints obtained with audio-band detectors. Even with a 60-60 $M_\odot$ system, the constraints are $O\!\left(10^{-10}\right) s^{-1}$. Again, typical events in DECIGO will have SNR ~ 1000, making the best possible constraints with DECIGO $O\!\left(10^{-18}\right) s^{-1}$.

Naively, one would think that the constraints would get better with stellar mass binaries in mHz detectors like LISA [233] or TianQin [234]. However, most systems in the mass range that we consider would effectively be monochromatic in such detectors, and their SNRs will also be low. We verified that the constraints here on a/c are similar to those obtained on $\dot{G}/G_0$ in other works [235].

4.5 Summary and Discussion

Recent work [236] has suggested that a significant fraction of LIGO-Virgo's BBHs could have merged in dense stellar environments, including within the disk of AGNs. [237] even claim possible evidence of an electromagnetic counterpart to GW190521 produced due to the kick-propelled ejection of this binary BBH merger from an AGN disk. This claim cannot be tested exclusively from the morphology of the observed GW signal due to the relatively large total mass of this BBH and the poor sensitivity of the LVK detectors at low frequencies [14].

Some works (see, e.g., [240]) have even speculated the possibility of mergers in the vicinity of SMBHs. The rate of these mergers is far from constrained, although the current expectation is that more massive CBCs will tend to merge closer to the SMBH than lighter ones, due to mass-segregation. However, other work (see, e.g., [159]) have proposed existence of migration traps close to the innermost stable circular orbit of the SMBH which could enable even relatively lighter

---

13. We have assumed that the systems we consider complete a full chirp in the DECIGO band between the assumed minimum and maximum frequency. For the lowest configuration of masses that we consider, the total time in-band is ~ 4 yrs, comparable to the expected mission duration of a space-based detector.

14. Recent work [238, 239] has shown that the AGN provenance of a similar event in LISA could be ascertained from the shape of the waveform.

binaries to merge in the vicinity of the SMBH.

In this work, we study the prospects of constraining line-of-sight acceleration a/c in future observing runs (O4, O5, XG and DECIGO). We then interpret these constraints in the context of mergers around SMBHs, to investigate if constraints on this acceleration could potentially serve as a smoking gun for the provenance of the CBC. We further place the very first GW data-driven constraints on the line-of-sight acceleration for putative BNSs GW170817 and GW190425.

We find that in O4, a/c (in units of s^{-1}) $= 0, 1 \times 10^{-5}, 1 \times 10^{-3}$ can be recovered with a precision of $\sim 1 \times 10^{-7}$ at 90% confidence for GW170817-like events. Importantly, however, large accelerations such as 1×10^{-3} could produce egregious biases in the recovered a/c if only the leading PN order is considered. The precision improves with future observing runs, as would be expected due to increased sensitivity at lower frequencies. BNS-like CBCs will have precisions (assuming SNR $= 10$) of $\sim 10^{-7} - 10^{-6}$ in O5, $\sim 10^{-8} - 10^{-7}$ in CE (single detector), and $\sim 10^{-9} - 10^{-8}$ in ET (single detector).

The low-frequency sensitivity of DECIGO promises spectacular constraints on a/c, with precisions that are several orders of magnitude better than XG detectors. Interpreting these constraints in the context of mergers around SMBHs, we find that GW170817-like BNSs could be probed out to distances as large as $R \sim 5$ kpc from the SMBH in a Milky Way-like galaxy (whose mass profile consisting of SMBH, dark matter, bulge, and disk components is simulated using `MWPotential2014` implemented in `galpy` [14]; see Fig. 4.5). In principle, this could enable an investigation of the motion of such BNSs in various parts of the galactic halo outside the SMBH's region of influence[15]. Even the motion of CBCs with total masses as large as $O(100 M_\odot)$ (and SNR ~ 1000) can be probed to a few parsecs from the center of the host galaxy. Such probes would be especially useful to test the claim that a large fraction of BBH mergers reside in AGNs. The techniques developed in this work can also be extended to probe motion and location of compact binaries in dense stellar environments such as globular clusters or nuclear star clusters

---

15. Note however that derivatives of a/c would also need to be constrained from the GW waveform to infer the position of the binary, and the mass-profile producing the gravitational potential. These can then be used to infer the magnitude of the acceleration of the binary in the potential.
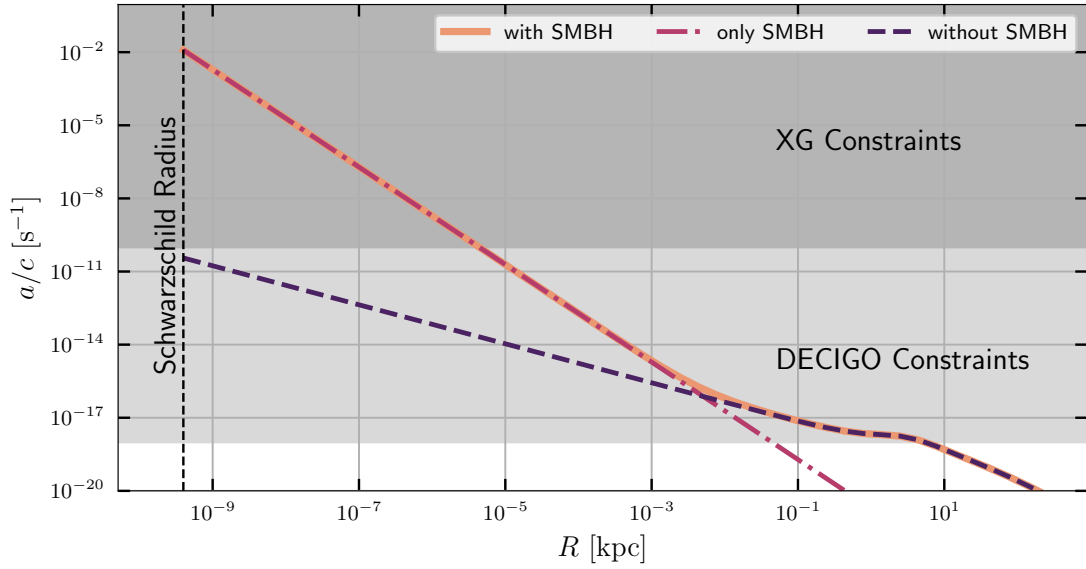
Figure 4.5: Accelerations in the Milky Way at different distances from its central black hole. The constraints in the figure assume that the acceleration is completely aligned with the line-of-sight, and thus represent a lower limit on the constraints. The accelerations are obtained using the `MWPotential2014` potential (consisting of dark matter, disk, and bulge components) as defined in `galpy` [14], along with a Kepler potential assuming $M_{\mathrm{SMBH}} = 4.154 \times 10^6 M_\odot$ [15] to account for the central SMBH (orange solid line). The dash-dotted and dashed lines respectively show accelerations only assuming the Kepler potential and `MWPotential2014`. Shaded regions showing constraints obtainable by future detector networks are shown for reference.

[213, 241, 242][16].

The non-detection of a/c, viz., one that is consistent with 0 at 90% confidence, can also be used to place constraints on the rate of mergers within a certain distance from the center of host galaxies. This, in turn, could help guide models of mergers in the vicinity of SMBHs, which currently have several uncertainties.

16. In the context of precision cosmology with DECIGO, measuring the acceleration of the Universe would need to account for the line-of-sight acceleration of the CBCs, both of which appear at the same PN order in the GW phase [243].

CHAPTER 5

PROBING THE LARGE SCALE STRUCTURE USING GRAVITATIONAL-WAVE OBSERVATIONS OF BINARY BLACK HOLES

5.1 Introduction

Although the network configuration and the sensitivity of the proposed XG detectors are not finalized, studies of various configurations and their implication on source localization and parameter estimation suggest that these detectors will be able to observe BBH mergers up to large redshifts (detection horizon up to $z \sim 100$) [244]. For the redshift range $z \in [0, 3]$, a significant fraction of BBH mergers can be localized to within 1 square degree [44].

During the second observing run, LIGO and Virgo detected GWs from a BNS merger, GW170817 [29], for the first time. EM counterparts of this event were also detected by several telescopes, which enabled the identification of the host galaxy of the merger [76]. This led to a precise measurement of the redshift of GW170817 and the first measurement of the Hubble constant H_0 from GW observations [30]. BNS detections expected in the near future with EM counterparts should improve the precision of this measurement, potentially contributing to resolving the apparent tension between the Planck measurement of H_0 [245] and that from type Ia supernovae [246]. Some studies also explore the techniques of cross-matching galaxy catalogs with BBH observations to constrain H_0 [91, 247, 248, 249, 250, 251, 252, 253, 254, 98].

With a large number of GW detections expected in the near future, we will have a population of BBH and BNS mergers distributed over a large redshift range, providing a new tracer of the large scale structure. Recent studies show that by cross correlating the GW events with galaxy catalogs, the large scale structure can be probed by estimating the linear bias [255, 256] or by the lensing of GWs [257]. In this work, we explore the possibility of probing the clustering of BBHs by estimating their two-point (auto)correlation function. If these mergers happen in specific types of galaxies, the clustering of the BBHs should trace that of such galaxies. If, for some reason, BBHs are predominantly distributed outside galaxies, their clustering information should reveal

this. Thus, an independent estimation of the clustering of BBHs offers an interesting probe of not only the large scale structure, but also the astrophysical environment of the mergers.

5.2   Method

The two-point correlation function (2PCF) $\xi(r)$ is related to the excess probability $\delta P(r)$, above what is expected for a random distribution, of finding a pair of objects (e.g., galaxies or, in the context of this work, BBH mergers) separated by distance r. This can be expressed as

$$\delta P(r) = n\,[1 + \xi(r)]\,dV, \tag{5.1}$$

where n is the number of objects per unit volume and dV is the volume element. For the matter overdensity field $\delta(\mathbf{x}) := \rho(\mathbf{x})/\bar{\rho} - 1$, where $\rho(\mathbf{x})$ is the local matter density and $\bar{\rho}$ the mean matter density of the Universe, the 2PCF is given by

$$\xi(r) = \langle \delta(\mathbf{x})\,\delta(\mathbf{y}) \rangle, \tag{5.2}$$

where angle brackets denote the ensemble average which, in turn, can be estimated by averaging over a large volume. The above equation assumes statistical homogeneity and isotropy of the Universe, hence ξ is only a function of the magnitude r of the separation vector $\mathbf{y} - \mathbf{x}$ between the two points $\mathbf{x}$ and $\mathbf{y}$. In general, the 2PCF is also a function of the redshift z. However, when we restrict ourselves to a relatively narrow redshift bin Δz, it can be assumed to be a constant within that redshift range.

The distribution of the galaxies in the Universe is expected to trace the underlying matter distribution. At large scales, to a good approximation, the 2PCF of the galaxies $\xi_{\mathrm{gal}}(r)$ is related to that of matter $\xi_{\mathrm{m}}(r)$ through a simple relation [258]

$$\xi_{\mathrm{gal}}(r) = b_{\mathrm{gal}}^2\,\xi_{\mathrm{m}}(r), \tag{5.3}$$

where b_{gal} is the galaxy bias, taken to be scale-independent. Usually, the value of b_{gal} depends on the luminosity and color type of galaxies [259]. Similarly, we can also define a bias which quantifies the clustering of the observed BBH population:

$$\xi_{\mathrm{BBH}}(r) = b_{\mathrm{BBH}}^2 \, \xi_{\mathrm{m}}(r). \tag{5.4}$$

If we are able to measure b_{BBH} from GW observations, this would allow us to compare it against b_{gal} estimated from other observations (e.g., EM galaxy surveys), thus providing hints to the host environments of the BBH mergers.

5.2.1 Estimating the BBH correlation function from GW observations

The interpretation of $\xi(r)$ as the excess probability of finding points separated by a distance r allows one to construct fast estimators of the correlation function from data. The Landy-Szalay (LS) estimator [260] is the most commonly-used estimator, and is given by,

$$\xi(r) = [DD(r) - 2DR(r) + RR(r)] \; RR(r)^{-1}. \tag{5.5}$$

Here, $DD(r)$ denotes the number of point-pairs in the data (galaxy catalogs or BBH mergers) separated by a distance r, $RR(r)$ denotes the number of point-pairs in an equal-sized simulated random catalog separated by a distance r, and $DR(r)$ denotes the number of data-random point pairs separated by a distance r. If N_D, N_R are the number of points in the data and random catalogs respectively, for general N_D, N_R, Eq.(5.5) gets modified [260] to,

$$\xi(r) = \left[\frac{DD(r)}{N_D(N_D - 1)} - \frac{DR(r)}{N_D N_R} + \frac{RR(r)}{N_R(N_R - 1)} \right] \left[\frac{RR(r)}{N_R(N_R - 1)} \right]^{-1}. \tag{5.6}$$

The correlation function of the galaxies from a survey can be estimated using Eq.(5.6). With next generation GW detectors like ET and CE, we expect to detect BBH mergers up to large redshifts. If the number of detections are sufficiently large, we can use their localization information to study
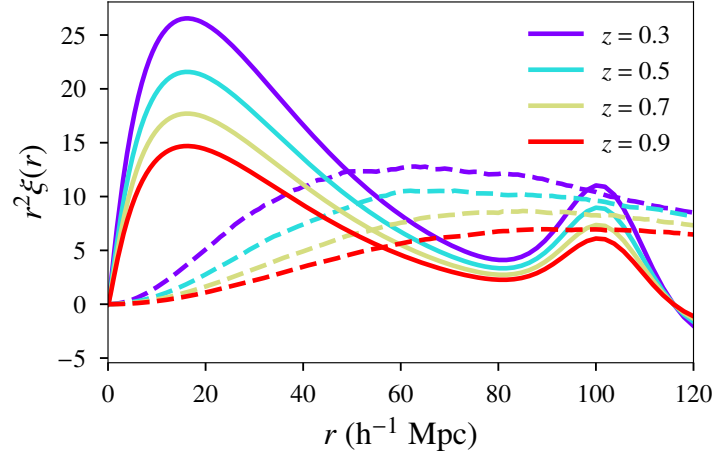
Figure 5.1: The "smeared" correlation function (dashed lines) and the "true" correlation function (solid lines) for various redshifts. The true correlation function is simply the matter correlation function calculated using Eisenstein-Hu prescription [16] for the standard model of cosmology. The "smearing" of the correlation function due to measurement errors is calculated assuming that the distribution of errors in localization of GW population follow a Gaussian distribution with mean $\{\mu_{RA} = 0.5°, \mu_{dec} = 0.5°, \mu_d = 50 \, h^{-1} \, \text{Mpc}\}$ and standard deviation $\{\sigma_{RA} = 0.5°, \sigma_{dec} = 0.5°, \sigma_d = 20 h^{-1} \, \text{Mpc}\}$.

how these GW events are clustered by estimating the correlation function $\xi_{BBH}(r)$.

5.2.2 *Smearing of the correlation function due to GW localization errors*

The challenge in estimating $\xi_{BBH}(r)$ is that the precision in the GW source localization (sky location and distance) will be poor as compared to the galaxy localization (which can be described as a point in the survey volume). Due to the large statistical uncertainties in the GW localization, the observed correlation function of BBHs will be modified from the actual correlation function — the poor source localization distributes weights from the points of actual location to a smeared field around those points. The "smearing" of the correlation function will depend on the distribution of the GW localization uncertainties from the population. The smeared correlation function (Fig. 5.1) can be computed by convolving the actual correlation function with the ensemble averaged localization posteriors obtained from GW data. We describe this below.

In the absence of any measurement errors, the probability distribution $P_{tr}(\mu)$ of the location μ

67

Angular: RA (degrees), Radial: Comoving distance (h^{-1} Mpc)
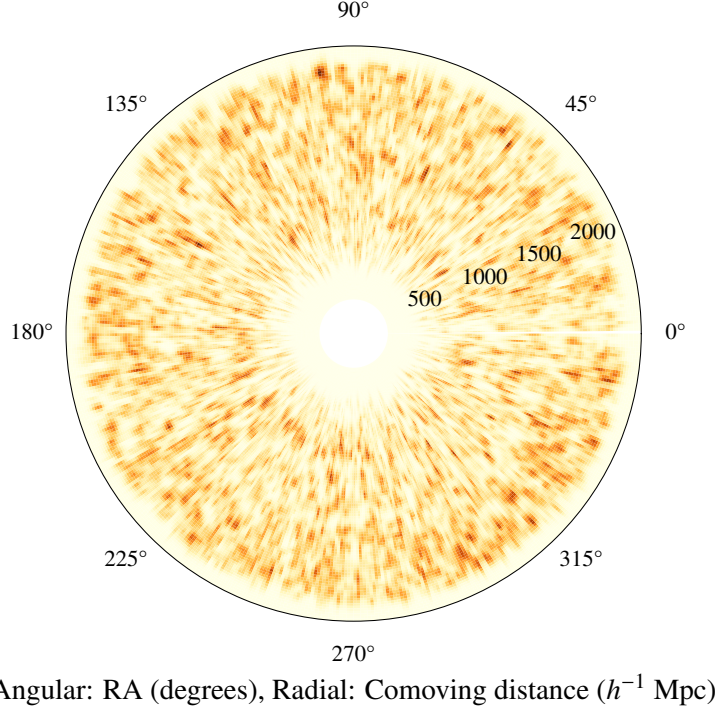
Figure 5.2: An example of probability field obtained from localization posteriors from a realization of simulated catalog of BBH observations in redshift range $z \in [0.1, 1.1]$. The radial direction corresponds to comoving distance and the angular direction corresponds to RA (the dec coordinate is projected out). BBH events are distributed according to the input power spectrum and bias factor (= 1.5) in each redshift bin. The errors on localization are drawn from a probability distribution described in the text.

of BBH mergers is given by

$$P_{\text{tr}}(\boldsymbol{\mu}) = N^{-1} \sum_i \delta^{(3)}(\boldsymbol{\mu} - \boldsymbol{\mu}_i), \tag{5.7}$$

where $\delta^{(3)}$ is the three dimensional Dirac delta function, $\boldsymbol{\mu}_i$ denotes the three-dimensional location of BBH i, and N is the total number of BBHs in the survey volume V such that $\int_V P_{\text{tr}}(\boldsymbol{\mu}) \, dV_\mu = 1$ (dV_μ is the volume element in μ; i.e, in Cartesian coordinates $dV_\mu := d\mu^3$). Density contrast in this field is given by[1]

$$\delta_{\text{tr}}(\boldsymbol{\mu}) := P_{\text{tr}}(\boldsymbol{\mu})/\bar{P}_{\text{tr}} - 1 = V P_{\text{tr}}(\boldsymbol{\mu}) - 1. \tag{5.8}$$

Above, $\bar{P}_{\text{tr}} = 1/V$ denotes the volume-averaged probability density. The correlation function

---

1. The density contrast δ_{tr} is not to be confused with the Dirac delta function $\delta^{(3)}$.
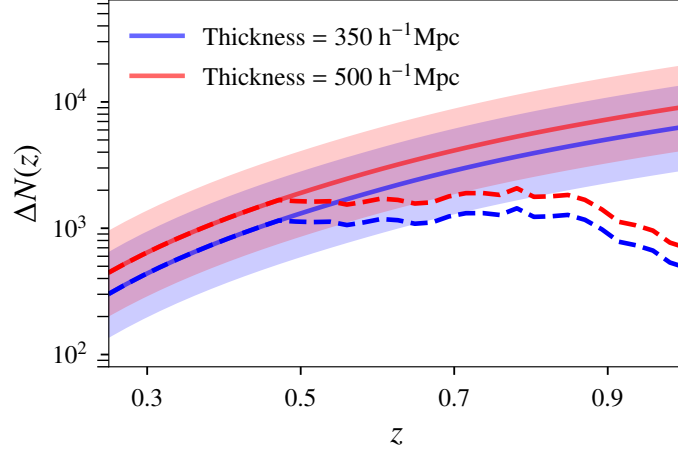
Figure 5.3: Solid curve with shaded region shows the total number of merger events as a function of redshift in shell of thickness $\sim 350\ h^{-1}$ Mpc and $\sim 500\ h^{-1}$ Mpc in comoving distance. These numbers are calculated by assuming the redshift distribution of BBHs from [17] and the local merger rates of BBHs estimated in [18]. The dashed lines show the average number of mergers in the shell of given thickness for which the errors in sky localization are within a degree square and errors in estimating the comoving distance are $\leq 90\ h^{-1}$ Mpc for a network of three XG detectors.

between two points μ and ν in the field of density contrast is given by

$$\xi_{\text{tr}}(\boldsymbol{\mu}, \boldsymbol{\nu}) := \langle \delta_{\text{tr}}(\boldsymbol{\mu})\,\delta_{\text{tr}}(\boldsymbol{\nu})\rangle = V^2\,\langle P_{\text{tr}}(\boldsymbol{\mu})\,P_{\text{tr}}(\boldsymbol{\nu})\rangle - 1, \tag{5.9}$$

where $\langle\rangle$ denotes ensemble averages. Using Eq.(5.7), we can write

$$\langle P_{\text{tr}}(\boldsymbol{\mu})\,P_{\text{tr}}(\boldsymbol{\nu})\rangle = N^{-2}\left\langle \sum_{ij} \delta^{(3)}(\boldsymbol{\mu} - \boldsymbol{\mu}_i)\,\delta^{(3)}(\boldsymbol{\nu} - \boldsymbol{\nu}_j)\right\rangle. \tag{5.10}$$

Now we investigate how the true correlation function $\xi_{\text{tr}}(\boldsymbol{\mu}, \boldsymbol{\nu})$ gets smeared by the presence of measurement uncertainties. Assuming that the localization posteriors follow Gaussian distributions,

$$\begin{aligned}
P_i(\mathbf{x} - \boldsymbol{\mu}_i, \Delta\boldsymbol{\mu}_i) &= \frac{1}{\sqrt{(2\pi)^3\,|\mathsf{C}_i|}} \exp\left[-\frac{1}{2}(\mathbf{x} - \boldsymbol{\mu}_i - \Delta\boldsymbol{\mu}_i)^T\right. \\
&\quad \times \left. \mathsf{C}_i^{-1}(\mathbf{x} - \boldsymbol{\mu}_i - \Delta\boldsymbol{\mu}_i)\right]
\end{aligned} \tag{5.11}$$

where $\boldsymbol{\mu}_i$ is the true location of the ith BBH, C_i is the covariance matrix for the corresponding

localization posterior (assumed to be diagonal), and $\Delta\boldsymbol{\mu}_i$ is the scatter induced by the detector noise. In the absence of systematic biases $\Delta\boldsymbol{\mu}_i$ will be distributed according to a Gaussian distribution of mean zero and covariance matrix C_i. We now marginalize $P_i(\mathbf{x} - \boldsymbol{\mu}_i, \Delta\boldsymbol{\mu}_i)$ over $\Delta\boldsymbol{\mu}_i$:

$$P_i(\mathbf{x} - \boldsymbol{\mu}_i) \quad = \quad \int dV_{\Delta\mu} \, P(\Delta\boldsymbol{\mu}_i) \, P_i(\mathbf{x} - \boldsymbol{\mu}_i, \Delta\boldsymbol{\mu}_i). \tag{5.12}$$

This averaging can be performed on the posterior (as opposed to the final correlation function) since the noise-induced shifts $\Delta\boldsymbol{\mu}_i$ are uncorrelated with the BBH locations $\boldsymbol{\mu}_i$. The resulting posterior $P_i(\mathbf{x} - \boldsymbol{\mu}_i)$ is a Gaussian distribution with mean $\boldsymbol{\mu}_i$ and covariance matrix $2C_i$. Using the property of Dirac delta function, $P_i(\mathbf{x} - \boldsymbol{\mu}_i)$ can be rewritten as

$$P_i(\mathbf{x} - \boldsymbol{\mu}_i) = \int dV_\mu \, P_i(\mathbf{x} - \boldsymbol{\mu}) \, \delta^{(3)}(\boldsymbol{\mu} - \boldsymbol{\mu}_i), \tag{5.13}$$

and the probability distribution of the location of a population of BBH mergers is given by

$$P(\mathbf{x}) = N^{-1} \sum_i P_i(\mathbf{x} - \boldsymbol{\mu}_i). \tag{5.14}$$

The correlation function between two points $\mathbf{x}$ and $\mathbf{y}$ of this probability field is given by

$$\langle P(\mathbf{x})P(\mathbf{y}) \rangle = N^{-2} \left\langle \sum_{ij} P_i(\mathbf{x} - \boldsymbol{\mu}_i) \, P_j(\mathbf{y} - \boldsymbol{\nu}_j) \right\rangle. \tag{5.15}$$

Note that each term in the sum over i, j is equal to the joint posterior probability of the BBH mergers i and j to take the positions $\mathbf{x}$ and $\mathbf{y}$, respectively. In a frequentist interpretation, this is equivalent to the joint probability of drawing two samples of $\mathbf{x}$ and $\mathbf{y}$ from the posteriors of the two events. The relation between this and our simulations should be apparent now. We only want to consider correlations between two different BBH mergers; thus, we restrict the sum to $i \neq j$. Now,

Using Eq.(5.13), this can be rewritten as

$$
\begin{aligned}
\langle P(\mathbf{x})P(\mathbf{y})\rangle \;=\; & N^{-2} \left\langle \sum_{ij} \int dV_\mu \, P_i(\mathbf{x} - \boldsymbol{\mu}) \, \delta^{(3)}(\boldsymbol{\mu} - \boldsymbol{\mu}_i) \right. \\
& \times \left. \int dV_\nu \, P_j(\mathbf{y} - \boldsymbol{\nu}) \, \delta^{(3)}(\boldsymbol{\nu} - \boldsymbol{\nu}_j) \right\rangle .
\end{aligned}
\tag{5.16}
$$

Now, we make the following assumptions:

1. Assuming that the widths of the posterior distributions are uncorrelated with the location of mergers on the sky (as would be expected for a GW detector network with uniform sky coverage)[2], we can write:

$$
\left\langle P_i(\mathbf{x} - \boldsymbol{\mu})P_j(\mathbf{x} - \boldsymbol{\nu}) \, \delta^{(3)}(\boldsymbol{\mu} - \boldsymbol{\mu}_i)\delta^{(3)}(\boldsymbol{\nu} - \boldsymbol{\nu}_j) \right\rangle = \left\langle P_i(\mathbf{x} - \boldsymbol{\mu})P_j(\mathbf{x} - \boldsymbol{\nu}) \right\rangle \left\langle \delta^{(3)}(\boldsymbol{\mu} - \boldsymbol{\mu}_i)\delta^{(3)}(\boldsymbol{\nu} - \boldsymbol{\nu}_j) \right\rangle .
$$

2. Since P_i and P_j are posterior probability distributions estimated from two independent GW events (uncorrelated noise),

$$
\left\langle P_i(\mathbf{x} - \boldsymbol{\mu})P_j(\mathbf{y} - \boldsymbol{\nu}) \right\rangle = \langle P_i(\mathbf{x} - \boldsymbol{\mu})\rangle \left\langle P_j(\mathbf{y} - \boldsymbol{\nu}) \right\rangle .
$$

3. Motivated by the homogeneity of space, we assume

$$
\langle P_i(\mathbf{x} - \boldsymbol{\mu})\rangle = P(\mathbf{x} - \boldsymbol{\mu}) \quad \text{and} \quad \left\langle P_j(\mathbf{y} - \boldsymbol{\nu}) \right\rangle = P(\mathbf{y} - \boldsymbol{\nu}) .
$$

---

2. This is a valid approximation for the three-detector network of GW detectors (at the locations of LIGO-Hanford, LIGO-Livingston, and Virgo) that we consider in our study. For a discussion of this, see Appendix B of Ref. [261].

Using these assumptions Eq.(5.16) can be rewritten as

$$\langle P(\mathbf{x})P(\mathbf{y})\rangle = N^{-2} \int dV_\mu \int dV_\nu \, P(\mathbf{x} - \mu) \, P(\mathbf{y} - \nu)$$

$$\times \left\langle \sum_{ij} \delta^{(3)}(\mu - \mu_i) \, \delta^{(3)}(\nu - \nu_j) \right\rangle.$$

$$= \int dV_\mu \int dV_\nu \, P(\mathbf{x} - \mu) \, P(\mathbf{y} - \nu) \, \langle P_{\text{tr}}(\mu) \, P_{\text{tr}}(\nu)\rangle, \tag{5.17}$$

where we have used Eq.(5.10) for the last step. The smeared correlation function of the probability density contrast field $\delta_P(\mathbf{x}) := P(\mathbf{x})/\bar{P} - 1$ is given by

$$\xi(\mathbf{x}, \mathbf{y}) = \langle \delta_P(\mathbf{x}) \, \delta_P(\mathbf{y})\rangle = V^2 \, \langle P(\mathbf{x}) \, P(\mathbf{y})\rangle - 1. \tag{5.18}$$

Using Eqs.(5.17) and (5.9), this can be rewritten as

$$\xi(\mathbf{x}, \mathbf{y}) = \int_V dV_\mu \int_V dV_\nu \, P(\mathbf{x} - \mu) \, P(\mathbf{y} - \nu) \, \xi_{\text{tr}}(\mu, \nu) \quad . \tag{5.19}$$

This can be used to compute the smeared correlation function $\xi(\mathbf{x}, \mathbf{y})$ from the true correlation function $\xi_{\text{tr}}(\mu, \nu)$. Essentially we convolve the true correlation function ξ_{tr} by a smoothing function (ensemble-averaged localization posteriors).

Due to the homogeneity and isotropy of space, the true correlation function only depends on the magnitude of the difference of its arguments $\xi_{\text{tr}}(|\nu - \mu|)$. We can exploit this by transforming to new integration variables, $\mathbf{a} := \mathbf{x} - \mu$ and $\mathbf{b} := \mathbf{y} - \nu$ to get:

$$\xi(\mathbf{y} - \mathbf{x}) = \int_V dV_a \int_V dV_b \, P(\mathbf{a}) \, P(\mathbf{b}) \, \xi_{\text{tr}}(s), \tag{5.20}$$

where $s := |\nu - \mu| = |(\mathbf{y} - \mathbf{x}) - (\mathbf{b} - \mathbf{a})|$. This shows that the smeared correlation function also depends only on the separation of points $\mathbf{x}$ and $\mathbf{y}$, i.e., $\xi(\mathbf{y} - \mathbf{x})$. However, unlike the true correlation function, the direction also matters unless posterior functions are isotropic. In the case of BBH mergers, we expect the radial uncertainty to be much larger than the angular uncertainties and

therefore we cannot demand isotropy and thus the orientation of $\mathbf{x} - \mathbf{y}$ matters. To deal with this, we average Eq.(5.20) over all orientations for a given $r := |\mathbf{x} - \mathbf{y}|$ to find the spherically averaged correlation function $\xi(r)$. We choose the volume of interest to be large enough to permit every possible orientation with minimal bias.

In this work, we simulate the combined probability distribution of BBHs by placing GW posteriors around the true BBH locations, after introducing a noise-induced scatter in the mean of the posteriors. The posterior distributions of right ascension (RA), declination (dec) and comoving distance (d), estimated from N simulated events are combined to create a normalized combined posterior probability field $P(\mathbf{x}) = N^{-1} \sum_{i=1}^{N} P_i(\mathbf{x})$, where $\mathbf{x} = \{\text{RA}, \text{dec}, d\}$. Assuming that the localization posteriors follow Gaussian distributions,

$$P_i(\mathbf{x}) = \mathcal{N} \exp\left[-\frac{1}{2}(\mathbf{x} - \boldsymbol{\mu}_i - \Delta\boldsymbol{\mu}_i)^T \mathsf{C}_i^{-1}(\mathbf{x} - \boldsymbol{\mu}_i - \Delta\boldsymbol{\mu}_i)\right] \tag{5.21}$$

where $\boldsymbol{\mu}_i$ is the true location of the ith BBH and C_i is the covariance matrix of the corresponding localization posterior (assumed to be diagonal), while $\mathcal{N} = 1/\sqrt{(2\pi)^3 |\mathsf{C}_i|}$ is a normalization constant. Note that the individual posteriors will in general not be centered around the true BBH locations, because of the scatter $\Delta\boldsymbol{\mu}_i$ introduced by the detector noise. This random scatter is drawn from a mean-zero Gaussian distribution of covariance matrix C_i. Figure 5.2 shows the $P(\mathbf{x})$ from a simulated catalog of BBH observations.

The correlation function of this field can be estimated by drawing random samples from this field and calculating LS estimator. By repeating this procedure many times, we get the average estimate of $\xi_{\text{BBH}}(r)$ and the corresponding error bars. We used the open source software package CORRFUNC [262, 263] for this purpose. Once we have the recovered correlation function $\xi_{\text{BBH}}(r)$, bias factor b_{BBH} can be estimated by comparing it with the smeared theoretical matter correlation function. For a given redshift bin centered around z, the bias $b_{\text{BBH}}(z)$ is estimated by averaging the same from all the r-bins.

5.3 Simulations and results
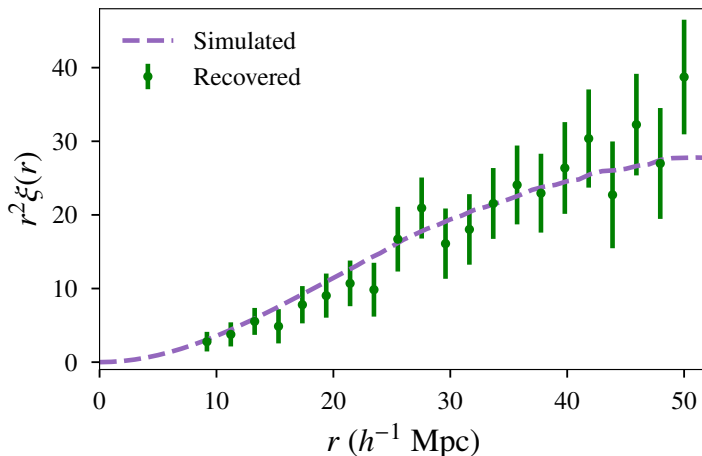
Figure 5.4: Smeared correlation function for a given distribution of localization errors is plotted along with the one recovered from simulated events at redshift 0.3 and input bias factor of 1.5. Smeared correlation function is scaled with input bias for comparison. We used 5000 simulated events distributed in a shell of thickness $350\ h^{-1}$ Mpc around the given redshift.

To put our method to test, we use the publicly available code LOGNORMAL_GALAXIES [264], to simulate galaxy catalogs at various redshifts with input power spectrum taken as the matter power spectrum approximated by the fitting function of Eisenstein and Hu [16] and consistent with the Planck-18 cosmological parameters [245]. This code enables one to generate mock galaxy catalogs assuming lognormal probability density function for the matter field and galaxies. We assume that GW events occur in any random subsample of the galaxies in the catalog, which essentially implies $b_{\mathrm{BBH}} = b_{\mathrm{gal}}$. We simulate three different catalogs having input linear bias $b_{\mathrm{gal}} = [1.0, 1.2, 1.5]$. Since it is possible to directly infer the distance (within the localization errors) to the BBH from the GW observations, peculiar velocities of galaxies will not play any role (unlike EM galaxy surveys where the distance is inferred from the redshift). Hence, while generating the catalogs, we switched off peculiar velocities in the code.

We then simulate the mock BBH catalogs using the steps outlined below and check whether we are able to recover the bias consistent with the input value. For simplicity, we have assumed the input b_{gal} to be redshift-independent, however, our conclusions on the recovery of the bias would

remain unchanged even if we use an evolving bias. These are the steps involved:

1. Choose a shell of thickness $350\ h^{-1}$ Mpc around the given redshift. The value was chosen so that we have enough events in the shell, and the actual correlation function does not vary appreciably within the redshift bin. The extent Δz of the redshift bin corresponding to this shell thickness at redshift $z = 0.3$ (1.0) turns out to be 0.13 (0.2).

2. Randomly select N galaxies from this shell as proxy for GW events and put localization error bars on each event assuming Gaussian posteriors (see below for details regarding uncertainties).

3. Select one point from each of the N posteriors. This simulates a particular realization of galaxy locations. Use LS estimator to estimate the correlation function. We repeat this process 1000 times and take the average to get $\xi(r)$.

4. To estimate the variance, we create 50 galaxy catalogs corresponding to different realization of the cosmic matter field to account for cosmic variance. For each of these catalogs, we select 20 sub-catalogs N of random galaxies each to account for fluctuations due to sampling, thus amounting to a total of 1000 sub-catalogs. One sub-catalog was taken as realization of our Universe and $\xi_{\mathrm{BBH}}(r)$ was estimated using steps described above. Error bars on $\xi_{\mathrm{BBH}}(r)$ was placed making use of the scatter estimated from other sub-catalogs.

5. Estimate the bias factor b_{BBH} by comparing the recovered correlation function $\xi_{\mathrm{BBH}}(r)$ with the smeared correlation function $\xi_{\mathrm{sm}}^{\mathrm{m}}(r)$. We estimate the correlation function in the range of comoving distance $r \in [10, 50] \sim h^{-1}$ Mpc as this is well within the chosen shell thickness and the linear bias approximation is valid in this range. To find the fit for the bias factor we then define a χ^2 function,

$$\chi^2(b) = \sum_{i,j} \left(\xi_{\mathrm{est}}(r_i) - b^2\, \xi_{\mathrm{sm}}^{\mathrm{m}}(r_i) \right) \Sigma_{ij}^{-1} \left(\xi_{\mathrm{est}}(r_j) - b^2\, \xi_{\mathrm{sm}}^{\mathrm{m}}(r_j) \right) \tag{5.22}$$

75

where $\xi_{\text{sm}}^{\text{m}}(r_i)$ is the smeared matter correlation function for the given distribution of localization errors, b is the bias factor, $\xi_{\text{est}}(r_i)$ is the correlation function estimated from the simulated catalog for each r-bin r_i, and Σ_{ij} is the error-covariance matrix between different bins in r. We then estimate mean and the standard deviation of the bias factor by minimizing χ^2 function.

Since we used the galaxies as proxy for GW events, we expect the recovered b_{BBH} to be consistent with the input bias factor used for simulating the galaxy distribution. Clearly, this method will be valid only when the errors in localization do not exceed the range of comoving distances we are trying to probe. This translates into the requirement that errors in RA, dec should be within a degree and errors in the comoving distances should not exceed few tens of Mpc. To find if this requirement can be fulfilled with XG detectors, we perform GW parameter estimation studies using a population of BBH events distributed up to redshift ~ 1.2 with XG detector network 2CE-ET (CE locations: one in Hanford, USA and one in LIGO-India location. ET location: proposed one in Europe). For simplicity, all the simulated BBHs have source-frame masses $m_1, m_2 = 35 M_\odot$ each and negligible spins (similar to the first BBH observation GW150914). We use the IMR-PHENOMPV2 [265] waveform available in the LALSUITE [217] software package along with the appropriate detector PSDs [41, 42] to simulate our signals, and use the PYCBCINFERENCE package [266] to determine distribution of localization errors. We find that a significant fraction of events up to $z \simeq 1$ fulfills this requirement. Figure 5.3 shows number of expected BBH mergers (using the BBH merger rate given in [18]) at various redshifts for one year of observations along with fraction of events that are expected to be localized well enough for this type of study. In our simulations, this selection introduces no significant biases; however possible selection effects need to be considered for the actual analysis. The distribution of the widths of the 68% credible regions of the marginalized posteriors on RA, dec and comoving distance can be approximated by truncated Gaussian distributions with mean $\{\mu_{\text{RA}} = 0.5°, \mu_{\text{dec}} = 0.5°, \mu_{\text{d}} = 50 \ h^{-1} \ \text{Mpc}\}$ and standard deviation $\{\sigma_{\text{RA}} = 0.5°, \sigma_{\text{dec}} = 0.5°, \sigma_{\text{d}} = 20 h^{-1} \ \text{Mpc}\}$[3]. For RA and dec, the range of

---

3. The posteriors on RA and dec are, in general, correlated with each other. For simplicity, we do not include these

truncated Gaussian was taken to be $\in [0.1°, 1.5°]$ and for comoving distance $\in [20, 90]\ h^{-1}$ Mpc.. The chosen distribution widths are consistent with expectations upto $z = 0.7$ from other studies such as Ref. [267]. We neglect the correlations between the errors in RA, dec and distance. For reference, an error on $1°$ corresponds to a comoving scale of $15\ h^{-1}$ Mpc, $23\ h^{-1}$ Mpc, and $30\ h^{-1}$ Mpc at redshifts 0.3, 0.5, and 0.7 respectively.
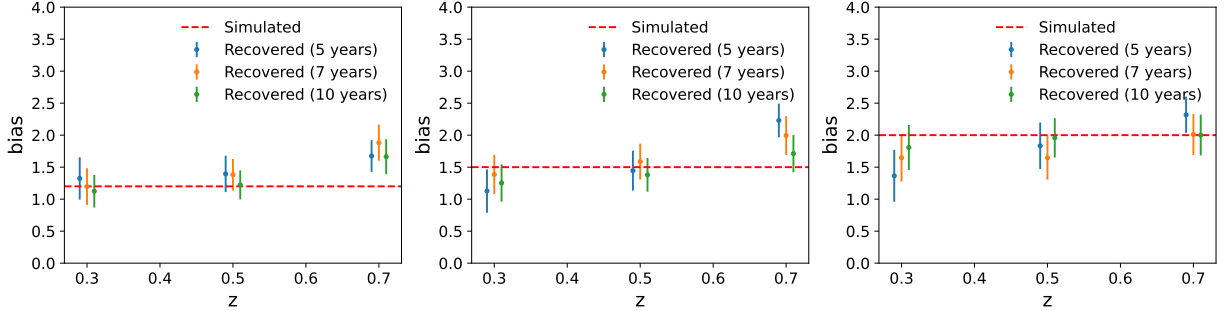
Figure 5.5: The recovered bias factor b_{BBH} from various redshifts bins (with shell thickness of $\sim 350\ h^{-1}$ Mpc). The catalogs were created using the matter power spectrum of Eisenstein-Hu with different values of linear bias 1 (left) 1.2 (middle) and 1.5 (right). Each subplot shows the estimated bias factor, along with the corresponding error bars (68% confidence regions), using GW observations of BBHs over a period of 5, 7 and 10 years.

Figure 5.4 shows the smeared correlation function compared to the estimated correlation function from a simulation using 5000 GW observation in a shell around the redshift $z = 0.3$. Figure 5.5 shows the bias factor recovered from different redshift bins using different observation duration (5, 7 and 10 years). The estimated b_{BBH}, in general, are consistent with the simulated bias within error-bars. The small number of events where the actual value is outside the error bars is consistent with statistical fluctuations. Note that even with a moderate observational time of five years, we can recover the bias to within $\sim 20\%$ at $z \lesssim 0.7$, while errors in bias recovery are larger at redshift $z \sim 1$ due to large errors in localization [4].

In order to test the robustness of this method, we simulated ~ 1000 catalogues with galaxies

---

correlation while generating our mock observations. Including these correlations would only improve the accuracy with which the correlation function is measured, since the sky area subtended by correlated posteriors will be smaller than subtended by uncorrelated posteriors.

4. Note that the LS estimator might not be the optimal estimator in the presence of measurement errors like in the case of GW observations. We are investigating alternative methods for the estimation of correlation function.
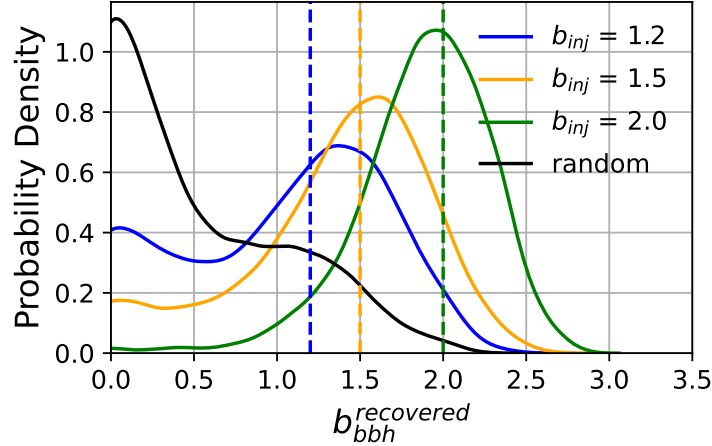
Figure 5.6: Blue, orange, and green curves represent the distribution of stacked posterior from realizations of simulated Universe with injected values of bias are b_{inj} = 1.2, 1.5, and 2.0 respectively. Black curve represent the same from Universes with random distribution of BBH mergers. This comparison is shown with Universe simulated at the redshift of 0.5 with 10 years of accumulated data.

distributed with b_{GW} = 1.2, 1.5, and 2.0. For reference, we also generated a catalog with no underlying correlation function i.e. galaxies are distributed randomly (corresponding to b = 0) at redshift z = 0.5. In Figure 5.6, we show the stacked posterior samples from all the individual runs. The width of stacked posterior samples depends on the localization volume distribution, and sampling errors. We note that the stacked posteriors are peaked around the injected values. These reference distribution, for given localization volumes, can be used to assign significance to a particular bias recovery measurement with respect to the random distribution.

There are various ways one can use the recovered $b_{BBH}(z)$ to understand the properties of the event hosts. For example, one can compare the clustering properties of the galaxies as measured from the optical surveys with $b_{BBH}(z)$ and obtain insights on the type of galaxies that host these merger events. Further, the recovered bias can also be related to the host dark matter halo mass [268]. In general, if one assumes that the typical masses of the haloes hosting these GW events do not evolve with redshift, one can predict the redshift-dependence of $b_{BBH}(z)$ for a given cosmological model. This then can be compared with the observations to understand the formation channels of the BBHs.

5.4   Summary

In this work we explored the possibility of probing large scale structure with BBH observations using XG GW detectors. We showed that bias factor can be estimated using clustering information of BBH events with 3-5 years of observations. This can be achieved solely from the GW observations, without requiring EM counterparts or galaxy catalogs. The bias factor b_{BBH} estimated from various redshifts will enable us to find whether the BBH mergers track the distribution of specific types of galaxies, or dark matter halos. Although the statistical precision of the estimated bias b_{BBH} is weaker than that of the galaxy bias obtained from EM galaxy surveys, it is important to note that the GW-based analysis probes the underlying dark matter distribution using a novel astrophysical tracer, thus enabling an independent probe of the large scale structure. We intend to extend this analysis to include effects such as selection bias, and method of cross correlating with galaxy catalogs to probe higher redshift, etc.

CHAPTER 6

SUMMARY

The detection of GWs has revolutionized the field of astronomy, and has opened up many unique avenues for probes of gravity, astrophysics, and cosmology. In this thesis, we explored a few of these probes. Wherever possible, we applied the methods developed to data from the LIGO, Virgo, and KAGRA detectors, while in other places we simulated data from various future observing scenarios to ascertain the applicability of our methods.

In chapter 2, we propose a method to constrain the variation of the gravitational constant G with cosmic time using GW observations of merging binary neutron stars. The method essentially relies on the fact that the maximum and minimum allowed masses of neutron stars at a particular cosmic epoch has a simple dependence on the value of G at that epoch. GWs carry an imprint of the value of G at the time of the merger. Thus, if the value of G at merger is significantly different from its current value, the masses of the neutron stars inferred from the GW observations will be inconsistent with the theoretically allowed range. This enables us to place bounds on the variation of G between the merger epoch and the present epoch. Using the observation of the binary neutron star system GW170817, we constrain the fractional difference in G between the merger and the current epoch to be in the range $-1 \lesssim \Delta G/G \lesssim 8$. Assuming a monotonic variation in G, this corresponds to a bound on the average rate of change of -7×10^{-9} yr$^{-1} \leq \dot{G}/G \leq 5 \times 10^{-8}$ yr^{-1} between these epochs. Future observations will put tight constraints on the deviation of G over vast cosmological epochs not probed by other observations. Our work can be extended by posing the problem in a fully Bayesian approach, and also by probing specific theories of gravity using the constraints over diverse epochs.

In chapter 3, we ask the question: can a BNS merger in the vicinity of a SMBH enable a detection of a postmerger gravitational wave signal? The postmerger GW signal of a BNS merger is expected to contain valuable information that could shed light on the EOS of NSs, the properties of the matter produced during the merger, as well as the nature of any potential intermediate merger product such as hypermassive or supramassive NSs. However, the postmerger lies in the

80

high frequency regime ($\gtrsim$ 1000 Hz) where current LIGO-Virgo detectors are insensitive. While proposed detectors such as NEMO, Cosmic Explorer and Einstein Telescope could potentially detect the postmerger for BNSs within $\mathcal{O}$(10 Mpc), such events are likely to be rare. We speculate on the possibility of detecting the postmerger from BNSs coalescing in the vicinity of SMBH. The redshift produced by the gravitational field of the SMBH, as well as the BNS's proper motion around the SMBH, could effectively "stretch" the postmerger signal into the band of the detectors. We demonstrate, using a phenomenological model, that such BNS coalescences would enable constraints on the peak of the postmerger signal that would otherwise have not been possible, provided the degree of redshifting due to the SMBH can be independently acquired. Further, using numerical simulations of binary neutron stars, we show how such mergers would improve EOS model selection using the postmerger signal. We discuss the mechanisms that might deliver such events, and the limitations of this work.

In chapter 4, we discuss the prospects of probing the line-of-sight acceleration of CBCs, which would enable novel probes the environments of CBCs. Line-of-sight acceleration of a CBC would modulate the shape of the GWs it produces with respect to the corresponding non-accelerated CBC. Such modulations could be indicative of its astrophysical environment. We investigate the prospects of detecting this acceleration in future observing runs of the LIGO-Virgo-KAGRA network, as well as in XG detectors and the proposed DECIGO. We place the first observational constraints on this acceleration, for putative binary neutron star mergers GW170817 and GW190425. We find no evidence of line-of-sight acceleration in these events at 90% confidence. Prospective constraints for the fifth observing run of the LIGO at A+ sensitivity, suggest that accelerations for typical BNSs could be constrained with a precision of $a/c \sim 10^{-7}$ [s^{-1}], assuming a signal-to-noise ratio of 10. These improve to $a/c \sim 10^{-9}$ [s^{-1}] in XG detectors, and $a/c \sim 10^{-16}$ [s^{-1}] in DECIGO. We also interpret these constraints in the context of mergers around SMBHs.

In chapter 5, we consider GW events as probes of the cosmological large scale structure, and ascertain how well we can measure two-point correlation function. XG GW detectors are expected to detect a large number of BBHs to large redshifts, opening up an independent probe of the large

scale structure using their clustering. This probe will be complementary to the probes using galaxy clustering — GW events could be observed up to very large redshifts ($z \sim 10$) although the source localization will be much poorer at large distances ($\sim$ tens of square degrees). We explore the possibility of probing the large scale structure from the spatial distribution of the observed BBH population, using their two-point (auto)correlation function. We find that we can estimate the bias factor of population of BBH (up to $z \sim 0.7$) with a few years of observations with these detectors. Our method relies solely on the source-location posteriors obtained from the GW events and does not require any information from electromagnetic observations. This will help in identifying the type of galaxies that host the BBH population, thus shedding light on their origins. Our work has already been extended to probe the baryon acoustic oscillation feature [269] in the correlation function.

In just $\sim$ 8 years since the first GW detection, we have detected $\sim$ 90 signals [34]. The ongoing observing run 4 (O4) of the LVK detectors is already adding to that number. The coming decades promise to be an exciting time for GW research, with an exponential increase in the number of detections from ground-based GW detectors. The space-based Laser Interferometer Space Antenna (LISA) mission will also allow us to observe gravitational-waves from a complementary set of astrophysical systems. While these would open up a wide variety of probes, many challenges related to the data analysis, theoretical modelling, interpretation etc. of the detected signals will be posed. Solving these challenges would be crucial to the progress of the field and interfacing astrophysical constraints derived from GWs with those derived using EM astronomy.

LIST OF PUBLICATIONS

Papers relevant to the thesis

1. **Aditya Vijaykumar**, Avinash Tiwari, Shasvath J. Kapadia, K.G. Arun, Parameswaran Ajith

   Waltzing binaries: Probing line-of-sight acceleration of merging compact objects with gravitational waves

   Astrophys. J. 954 (2023) 1, 105, arXiv:2302.09651.

2. **Aditya Vijaykumar**, Shasvath J. Kapadia, Parameswaran Ajith

   Can a binary neutron star merger in the vicinity of a supermassive black hole enable a detection of a post-merger gravitational wave signal?

   MNRAS, 513, 3577 (2022), arXiv:2202.08673.

3. **Aditya Vijaykumar**, M. V. S. Saketh, Sumit Kumar, Parameswaran Ajith, Tirthankar Roy Choudhury

   Probing the large scale structure using gravitational wave observations of binary black holes,

   Phys. Rev. D 108 (2023) 10, 103017, arXiv:2005.01111.

4. **Aditya Vijaykumar**, Shasvath J. Kapadia, Parameswaran Ajith

   Constraints on the time variation of the gravitational constant using gravitational wave observations of binary neutron stars,

   Phys. Rev. Lett. 126, 141104 (2021), arXiv:2003.12832.

Other papers

1. Avinash Tiwari, **Aditya Vijaykumar**, Shasvath J. Kapadia, Giacomo Fragione, Sourav Chatterjee

   Accelerated binary black holes in globular clusters: forecasts and detectability in the era of

space-based gravitational-wave detectors

Accepted to *MNRAS*, arXiv:2307.00930.

2. Adhrit Ravichandran, **Aditya Vijaykumar**, Shasvath J. Kapadia, Prayush Kumar

   Rapid Identification and Classification of Eccentric Gravitational Wave Inspirals with Machine Learning

   Accepted to *Physical Review D*, arXiv:2302.00666.

3. Srashti Goyal, **Aditya Vijaykumar**, Jose Maria Ezquiaga, Miguel Zumalacarregui

   Probing lens-induced gravitational-wave birefringence as a test of general relativity

   Accepted to *Physical Review D*, arXiv:2301.04826.

4. Bikram Keshari Pradhan, **Aditya Vijaykumar**, Debarati Chatterjee

   Impact of updated Multipole Love and f-Love Universal Relations in context of Binary Neutron Stars

   Phys. Rev. D. 107 (2023) 2, 023010, arXiv:2210.09425.

5. **Aditya Vijaykumar**, Ajit Kumar Mehta, Apratim Ganguly

   Detection and parameter estimation challenges of Type-II lensed binary black hole signals

   Submitted to *Physical Review D*, arXiv:2202.06334.

6. Abbott et al. (LIGO Scientific and Virgo Collaborations including **Aditya Vijaykumar**)

   Tests of General Relativity with GWTC-3,

   Accepted to *Physical Review D*, arXiv:2112.06861.

7. Sumit Kumar, **Aditya Vijaykumar**, Alexander H. Nitz

   Detecting Baryon Acoustic Oscillations with third generation gravitational wave observatories,

   ApJ 930 113, arXiv:2110.06152.

8. M. Saleem et al. (including **Aditya Vijaykumar**)

The Science Case for LIGO-India

Class. Quantum Grav. 39 025004, arXiv:2105.01716.

9. Abbott et al. (LIGO Scientific and Virgo Collaborations including **Aditya Vijaykumar**)
   Tests of General Relativity with Binary Black Holes from the second LIGO-Virgo Gravitational-Wave Transient Catalog,
   Phys. Rev. D 103 (2021) 12, 122002, arXiv:2010.14529.

10. Abbott et al. (LIGO Scientific and Virgo Collaborations including **Aditya Vijaykumar**)
    GWTC-2: Compact Binary Coalescences Observed by LIGO and Virgo During the First Half of the Third Observing Run,
    Phys. Rev. X 11 (2021) 021053, arXiv:2010.14527.

11. P. Virtanen *et al.* (including **Aditya Vijaykumar** as *SciPy 1.0 Contributor*)
    SciPy 1.0–Fundamental Algorithms for Scientific Computing in Python,
    Nat Methods 17, 261–272 (2020), arXiv:1907.10121.

BIBLIOGRAPHY

[1] LIGO SCIENTIFIC, VIRGO collaboration, *Properties of the binary neutron star merger GW170817*, *Phys. Rev. X* **9** (2019) 011001 [`1805.11579`].

[2] LIGO SCIENTIFIC, VIRGO collaboration, *GW190425: Observation of a Compact Binary Coalescence with Total Mass ∼ 3.4$M_\odot$*, *Astrophys. J. Lett.* **892** (2020) L3 [`2001.01761`].

[3] C. Bambi, M. Giannotti and F. L. Villante, *Response of primordial abundances to a general modification of G_n and/or of the early universe expansion rate*, *Phys. Rev. D* **71** (2005) 123524.

[4] O. G. Benvenuto, E. García-Berro and J. Isern, *Asteroseismological bound on $\dot{G}/g$ from pulsating white dwarfs*, *Phys. Rev. D* **69** (2004) 082002.

[5] V. M. Kaspi, J. H. Taylor and M. F. Ryba, *High - precision timing of millisecond pulsars. 3: Long - term monitoring of PSRs B1855+09 and B1937+21*, *Astrophys. J.* **428** (1994) 713.

[6] S. E. Thorsett, *The gravitational constant, the chandrasekhar limit, and neutron star masses*, *Phys. Rev. Lett.* **77** (1996) 1432.

[7] D. B. Guenther, L. M. Krauss and P. Demarque, *Testing the constancy of the gravitational constant using helioseismology*, *The Astrophysical Journal* **498** (1998) 871.

[8] F. Hofmann and J. Müller, *Relativistic tests with lunar laser ranging*, *Classical and Quantum Gravity* **35** (2018) 035015.

[9] B. Kiziltan, A. Kottas, M. De Yoreo and S. E. Thorsett, *The Neutron Star Mass Distribution*, *Astrophys. J.* **778** (2013) 66 [`1309.6635`].

[10] N. Farrow, X.-J. Zhu and E. Thrane, *The mass distribution of Galactic double neutron stars*, *Astrophys. J.* **876** (2019) 18 [`1902.03300`].

[11] S. Bernuzzi, A. Nagar, S. Balmelli, T. Dietrich and M. Ujevic, *Quasiuniversal properties of neutron star mergers*, *Phys. Rev. Lett.* **112** (2014) 201101 [`1402.6244`].

[12] CoRe Collaboration, "Computational relativity (CoRe) gw database." `http://www.computational-relativity.org/gwdb/`, 2022.

[13] K. W. Tsang, T. Dietrich and C. Van Den Broeck, *Modeling the postmerger gravitational wave signal and extracting binary properties from future binary neutron star detections*, Phys. Rev. D **100** (2019) 044047 [`1907.02424`].

[14] J. Bovy, *galpy: A Python Library for Galactic Dynamics*, *Astrophys. J. Suppl.* **216** (2015) 29 [`1412.3451`].

[15] GRAVITY Collaboration, R. Abuter, A. Amorim, M. Bauböck, J. P. Berger, H. Bonnet et al., *A geometric distance measurement to the Galactic center black hole with 0.3% uncertainty*, A&A **625** (2019) L10 [`1904.05721`].

[16] D. J. Eisenstein and W. Hu, *Power spectra for cold dark matter and its variants*, *Astrophys. J.* **511** (1997) 5 [`astro-ph/9710252`].

[17] K. Belczynski et al., *The Effect of Pair-Instability Mass Loss on Black Hole Mergers*, *Astron. Astrophys.* **594** (2016) A97 [`1607.03116`].

[18] LIGO SCIENTIFIC, VIRGO collaboration, *Binary Black Hole Population Properties Inferred from the First and Second Observing Runs of Advanced LIGO and Advanced Virgo*, *Astrophys. J.* **882** (2019) L24 [`1811.12940`].

[19] S. Bernuzzi, A. Nagar, T. Dietrich and T. Damour, *Modeling the Dynamics of Tidally Interacting Binary Neutron Stars up to the Merger*, *Phys. Rev. Lett.* **114** (2015) 161103 [`1412.4553`].

[20] T. Dietrich, S. Bernuzzi and W. Tichy, *Closed-form tidal approximants for binary neutron star gravitational waveforms constructed from high-resolution numerical relativity simulations*, *Phys. Rev. D* **96** (2017) 121501 [`1706.02969`].

[21] A. Einstein, *The Field Equations of Gravitation*, *Sitzungsber. Preuss. Akad. Wiss. Berlin (Math. Phys.)* **1915** (1915) 844.

[22] A. Einstein, *Über Gravitationswellen*, *Sitzungsber. Preuss. Akad. Wiss. Berlin (Math. Phys.)* **1918** (1918) 154.

[23] M. E. Gertsenshtein and V. I. Pustovoit, *On the Detection of Low Frequency Gravitational Waves*, *Sov. Phys. JETP* **16** (1962) 433.

[24] R. Weiss, D. Muehlner, R. Benford, D. Owens, N. Pierre and M. Rosenbluh, *Gravitation research*, .

[25] LIGO SCIENTIFIC, VIRGO collaboration, *Observation of Gravitational Waves from a Binary Black Hole Merger*, *Phys. Rev. Lett.* **116** (2016) 061102 [`1602.03837`].

[26] LIGO SCIENTIFIC, VIRGO collaboration, *Tests of general relativity with GW150914*, *Phys. Rev. Lett.* **116** (2016) 221101 [`1602.03841`].

[27] LIGO SCIENTIFIC, VIRGO collaboration, *The Rate of Binary Black Hole Mergers Inferred from Advanced LIGO Observations Surrounding GW150914*, *Astrophys. J. Lett.* **833** (2016) L1 [`1602.03842`].

[28] LIGO SCIENTIFIC, VIRGO collaboration, *GW170817: Observation of Gravitational Waves from a Binary Neutron Star Inspiral*, *Phys. Rev. Lett.* **119** (2017) 161101 [`1710.05832`].

[29] LIGO SCIENTIFIC, VIRGO, FERMI GBM, INTEGRAL, ICECUBE, ASTROSAT CADMIUM ZINC TELLURIDE IMAGER TEAM, IPN, INSIGHT-HXMT, ANTARES, SWIFT, AGILE TEAM, 1M2H TEAM, DARK ENERGY CAMERA GW-EM, DES,

DLT40, GRAWITA, FERMI-LAT, ATCA, ASKAP, LAS CUMBRES OBSERVATORY GROUP, OzGRAV, DWF (DEEPER WIDER FASTER PROGRAM), AST3, CAASTRO, VINROUGE, MASTER, J-GEM, GROWTH, JAGWAR, CALTECHNRAO, TTU-NRAO, NuSTAR, PAN-STARRS, MAXI TEAM, TZAC CONSORTIUM, KU, NORDIC OPTICAL TELESCOPE, ePESSTO, GROND, TEXAS TECH UNIVERSITY, SALT GROUP, TOROS, BOOTES, MWA, CALET, IKI-GW FOLLOW-UP, H.E.S.S., LOFAR, LWA, HAWC, PIERRE AUGER, ALMA, EURO VLBI TEAM, PI OF SKY, CHANDRA TEAM AT McGILL UNIVERSITY, DFN, ATLAS TELESCOPES, HIGH TIME RESOLUTION UNIVERSE SURVEY, RIMAS, RATIR, SKA SOUTH AFRICA/MEERKAT collaboration, *Multi-messenger Observations of a Binary Neutron Star Merger*, *Astrophys. J. Lett.* **848** (2017) L12 [`1710.05833`].

[30] LIGO SCIENTIFIC, VIRGO, 1M2H, DARK ENERGY CAMERA GW-E, DES, DLT40, LAS CUMBRES OBSERVATORY, VINROUGE, MASTER collaboration, *A gravitational-wave standard siren measurement of the Hubble constant*, *Nature* **551** (2017) 85 [`1710.05835`].

[31] P. Creminelli and F. Vernizzi, *Dark Energy after GW170817 and GRB170817A*, *Phys. Rev. Lett.* **119** (2017) 251302 [`1710.05877`].

[32] J. M. Ezquiaga and M. Zumalacárregui, *Dark Energy After GW170817: Dead Ends and the Road Ahead*, *Phys. Rev. Lett.* **119** (2017) 251304 [`1710.05901`].

[33] LIGO SCIENTIFIC, VIRGO collaboration, *GW170817: Measurements of neutron star radii and equation of state*, *Phys. Rev. Lett.* **121** (2018) 161101 [`1805.11581`].

[34] LIGO SCIENTIFIC, VIRGO, KAGRA collaboration, *GWTC-3: Compact Binary Coalescences Observed by LIGO and Virgo During the Second Part of the Third Observing Run*, *arXiv preprint arXiv:2111.03606* (2021) [`2111.03606`].

[35] KAGRA, VIRGO, LIGO SCIENTIFIC collaboration, *Population of Merging Compact Binaries Inferred Using Gravitational Waves through GWTC-3*, *Phys. Rev. X* **13** (2023) 011048 [`2111.03634`].

[36] LIGO SCIENTIFIC collaboration, *Advanced LIGO*, *Class. Quant. Grav.* **32** (2015) 074001 [`1411.4547`].

[37] VIRGO collaboration, *Advanced Virgo: a second-generation interferometric gravitational wave detector*, *Class. Quant. Grav.* **32** (2015) 024001 [`1408.3978`].

[38] KAGRA collaboration, *Overview of KAGRA: Detector design and construction history*, *PTEP* **2021** (2021) 05A101 [`2005.05574`].

[39] B. Iyer et al., *LIGO-India, Proposal of the Consortium for Indian Initiative in Gravitational-wave Observations (IndIGO)*, .

[40] M. Punturo et al., *The third generation of gravitational wave observatories and their science reach*, *Class. Quant. Grav.* **27** (2010) 084007.

[41] S. Hild et al., *Sensitivity Studies for Third-Generation Gravitational Wave Observatories*, *Class. Quant. Grav.* **28** (2011) 094013 [`1012.0908`].

[42] LIGO SCIENTIFIC collaboration, *Exploring the Sensitivity of Next Generation Gravitational Wave Detectors*, *Class. Quant. Grav.* **34** (2017) 044001 [`1607.08697`].

[43] D. Reitze et al., *Cosmic Explorer: The U.S. Contribution to Gravitational-Wave Astronomy beyond LIGO*, *Bull. Am. Astron. Soc.* **51** (2019) 035 [`1907.04833`].

[44] S. Vitale and M. Evans, *Parameter estimation for binary black holes with networks of third generation gravitational-wave detectors*, *Phys. Rev.* **D95** (2017) 064052 [`1610.06917`].

[45] C. Mills, V. Tiwari and S. Fairhurst, *Localization of binary neutron star mergers with second and third generation gravitational-wave detectors*, *Phys. Rev. D* **97** (2018) 104064 [`1708.00806`].

[46] C. W. Misner, K. S. Thorne and J. A. Wheeler, *Gravitation*. W. H. Freeman, San Francisco, 1973.

[47] M. Maggiore, *Gravitational Waves: Volume 1: Theory and Experiments*. OUP Oxford, 2007.

[48] T. Padmanabhan, *Gravitation: Foundations and frontiers*. Cambridge University Press, 12, 2014.

[49] P. R. Saulson, *Fundamentals of Interferometric Gravitational Wave Detectors*. World Scientific, 2nd. ed. ed., 2017, 10.1142/10116.

[50] C. Cutler and E. E. Flanagan, *Gravitational waves from merging compact binaries: How accurately can one extract the binary's parameters from the inspiral wave form?*, *Phys. Rev. D* **D49** (1994) 2658 [gr-qc/9402014].

[51] T. W. Baumgarte and S. L. Shapiro, *Numerical Relativity: Solving Einstein's Equations on the Computer*. Cambridge University Press, 2010, 10.1017/CBO9781139193344.

[52] A. Einstein, *Explanation of the Perihelion Motion of Mercury from the General Theory of Relativity*, *Sitzungsber. Preuss. Akad. Wiss. Berlin (Math. Phys.)* **1915** (1915) 831.

[53] J. M. Weisberg and J. H. Taylor, *Observations of Post-Newtonian Timing Effects in the Binary Pulsar PSR 1913+16*, *Phys. Rev. Lett.* **52** (1984) 1348.

[54] L. Blanchet, *Gravitational Radiation from Post-Newtonian Sources and Inspiralling Compact Binaries*, *Living Rev. Rel.* **17** (2014) 2 [1310.1528].

[55] L. Blanchet, G. Faye, Q. Henry, F. Larrouturou and D. Trestini, *Gravitational-Wave Phasing of Compact Binary Systems to the Fourth-and-a-Half post-Newtonian Order*, 2304.11185.

[56] R. L. Arnowitt, S. Deser and C. W. Misner, *The Dynamics of general relativity*, *Gen. Rel. Grav.* **40** (2008) 1997 [gr-qc/0405109].

[57] L. Lehner and F. Pretorius, *Numerical Relativity and Astrophysics*, *Ann. Rev. Astron. Astrophys.* **52** (2014) 661 [`1405.4840`].

[58] C. V. Vishveshwara, *Stability of the schwarzschild metric*, *Phys. Rev. D* **1** (1970) 2870.

[59] S. Bhagwat, M. Okounkova, S. W. Ballmer, D. A. Brown, M. Giesler, M. A. Scheel et al., *On choosing the start time of binary black hole ringdowns*, *Phys. Rev. D* **97** (2018) 104065 [`1711.00926`].

[60] M. Giesler, M. Isi, M. A. Scheel and S. Teukolsky, *Black Hole Ringdown: The Importance of Overtones*, *Phys. Rev. X* **9** (2019) 041060 [`1903.08284`].

[61] M. Isi, M. Giesler, W. M. Farr, M. A. Scheel and S. A. Teukolsky, *Testing the no-hair theorem with GW150914*, *Phys. Rev. Lett.* **123** (2019) 111102 [`1905.00869`].

[62] R. Cotesta, G. Carullo, E. Berti and V. Cardoso, *Analysis of Ringdown Overtones in GW150914*, *Phys. Rev. Lett.* **129** (2022) 111102 [`2201.00822`].

[63] P. Ajith et al., *Phenomenological template family for black-hole coalescence waveforms*, *Class. Quant. Grav.* **24** (2007) S689 [`0704.3764`].

[64] A. Buonanno and T. Damour, *Effective one-body approach to general relativistic two-body dynamics*, *Phys. Rev. D* **59** (1999) 084006 [`gr-qc/9811091`].

[65] L. A. Wainstein and V. D. Zubakov, *Extraction of Signals from Noise*. 1970.

[66] J. Creighton and W. Anderson, *Gravitational-Wave Physics and Astronomy: An Introduction to Theory, Experiment and Data Analysis*. 2011.

[67] W. M. Farr, J. R. Gair, I. Mandel and C. Cutler, *Counting and confusion: Bayesian rate estimation with multiple populations*, *Phys. Rev. D* **91** (2015) 023005 [`1302.5341`].

[68] E. Thrane and C. Talbot, *An introduction to Bayesian inference in gravitational-wave astronomy: parameter estimation, model selection, and hierarchical models*, *Publ. Astron. Soc. Austral.* **36** (2019) e010 [`1809.02293`].

[69] N. Christensen and R. Meyer, *Parameter estimation with gravitational waves*, *Rev. Mod. Phys.* **94** (2022) 025001 [`2204.04449`].

[70] J. Skilling, *Nested sampling for general Bayesian computation*, *Bayesian Analysis* **1** (2006) 833.

[71] LIGO SCIENTIFIC, VIRGO collaboration, *GW190425: Observation of a Compact Binary Coalescence with Total Mass ∼ 3.4$M_\odot$*, *Astrophys. J. Lett.* **892** (2020) L3 [`2001.01761`].

[72] B. D. Metzger, *Kilonovae*, *Living Reviews in Relativity* **20** (2017) 3 [`1610.09381`].

[73] LIGO SCIENTIFIC, VIRGO collaboration, *Estimating the Contribution of Dynamical Ejecta in the Kilonova Associated with GW170817*, *Astrophys. J. Lett.* **850** (2017) L39 [`1710.05836`].

[74] D. Kasen, B. Metzger, J. Barnes, E. Quataert and E. Ramirez-Ruiz, *Origin of the heavy elements in binary neutron-star mergers from a gravitational-wave event*, Nature **551** (2017) 80 [`1710.05463`].

[75] M. Bulla, *POSSIS: predicting spectra, light curves, and polarization for multidimensional models of supernovae and kilonovae*, MNRAS **489** (2019) 5037 [`1906.04205`].

[76] LIGO SCIENTIFIC, VIRGO, FERMI-GBM, INTEGRAL collaboration, *Gravitational Waves and Gamma-rays from a Binary Neutron Star Merger: GW170817 and GRB 170817A*, *Astrophys. J. Lett.* **848** (2017) L13 [`1710.05834`].

[77] R. Margutti and R. Chornock, *First Multimessenger Observations of a Neutron Star Merger*, *Ann. Rev. Astron. Astrophys.* **59** (2021) 155 [`2012.04810`].

[78] P. Kroupa, *On the variation of the initial mass function*, MNRAS **322** (2001) 231 [`astro-ph/0009005`].

[79] S. E. Woosley, *Pulsational Pair-Instability Supernovae*, *Astrophys. J.* **836** (2017) 244 [`1608.08939`].

[80] V. Tiwari and S. Fairhurst, *The Emergence of Structure in the Binary Black Hole Mass Distribution*, *Astrophys. J. Lett.* **913** (2021) L19 [`2011.04502`].

[81] B. Edelman, Z. Doctor, J. Godfrey and B. Farr, *Ain't No Mountain High Enough: Semiparametric Modeling of LIGO–Virgo's Binary Black Hole Mass Distribution*, *Astrophys. J.* **924** (2022) 101 [`2109.06137`].

[82] A. M. Farah, B. Edelman, M. Zevin, M. Fishbach, J. M. Ezquiaga, B. Farr et al., *Things that might go bump in the night: Assessing structure in the binary black hole mass spectrum*, `2301.00834`.

[83] M. Renzo, R. Farmer, S. Justham, Y. Götberg, S. E. de Mink, E. Zapartas et al., *Predictions for the hydrogen-free ejecta of pulsational pair-instability supernovae*, A&A **640** (2020) A56 [`2002.05077`].

[84] P. Madau and M. Dickinson, *Cosmic Star Formation History*, *Ann. Rev. Astron. Astrophys.* **52** (2014) 415 [`1403.0007`].

[85] LIGO SCIENTIFIC, VIRGO, KAGRA collaboration, *Tests of General Relativity with GWTC-3*, `2112.06861`.

[86] C. D. Capano, M. Cabero, J. Westerweck, J. Abedi, S. Kastha, A. H. Nitz et al., *Observation of a multimode quasi-normal spectrum from a perturbed black hole*, `2105.05238`.

[87] M. H.-Y. Cheung et al., *Nonlinear Effects in Black Hole Ringdown*, *Phys. Rev. Lett.* **130** (2023) 081401 [`2208.07374`].

[88] V. Baibhav, M. H.-Y. Cheung, E. Berti, V. Cardoso, G. Carullo, R. Cotesta et al., *Agnostic black hole spectroscopy: quasinormal mode content of numerical relativity waveforms and limits of validity of linear perturbation theory*, 2302.03050.

[89] LIGO SCIENTIFIC, VIRGO collaboration, *Tests of General Relativity with GW170817*, *Phys. Rev. Lett.* **123** (2019) 011102 [1811.00364].

[90] K. Pardo, M. Fishbach, D. E. Holz and D. N. Spergel, *Limits on the number of spacetime dimensions from GW170817*, *JCAP* **07** (2018) 048 [1801.08160].

[91] B. F. Schutz, *Determining the Hubble Constant from Gravitational Wave Observations*, *Nature* **323** (1986) 310.

[92] D. E. Holz and S. A. Hughes, *Using Gravitational-Wave Standard Sirens*, ApJ **629** (2005) 15 [astro-ph/0504616].

[93] W. Del Pozzo, *Inference of the cosmological parameters from gravitational waves: application to second generation interferometers*, *Phys. Rev. D* **86** (2012) 043011 [1108.1317].

[94] S. Bera, D. Rana, S. More and S. Bose, *Incompleteness Matters Not: Inference of H_0 from Binary Black Hole–Galaxy Cross-correlations*, *Astrophys. J.* **902** (2020) 79 [2007.04271].

[95] S. Mukherjee, B. D. Wandelt, S. M. Nissanke and A. Silvestri, *Accurate precision Cosmology with redshift unknown gravitational wave sources*, *Phys. Rev. D* **103** (2021) 043520 [2007.02943].

[96] S. R. Taylor, J. R. Gair and I. Mandel, *Hubble without the Hubble: Cosmology using advanced gravitational-wave detectors alone*, *Phys. Rev. D* **85** (2012) 023535 [1108.5161].

[97] W. M. Farr, M. Fishbach, J. Ye and D. Holz, *A Future Percent-Level Measurement of the Hubble Expansion at Redshift 0.8 With Advanced LIGO*, *Astrophys. J. Lett.* **883** (2019) L42 [`1908.09084`].

[98] LIGO SCIENTIFIC, VIRGO,, KAGRA, VIRGO collaboration, *Constraints on the Cosmic Expansion History from GWTC–3*, *Astrophys. J.* **949** (2023) 76 [`2111.03604`].

[99] P. A. M. Dirac, *The Cosmological Constants*, *Nature* **139** (1937) .

[100] P. A. M. Dirac, *A New Basis for Cosmology*, *Proceedings of the Royal Society A* **165** (1938) .

[101] P. Jordan, *Formation of the Stars and Development of the Universe*, *Nature* **164** (1949) 637.

[102] P. Jordan, *The present state of Dirac's cosmological hypothesis*, *Z. Phys.* **157** (1959) 112.

[103] P. Jordan, *Die physikalischen Weltkonstanten*, *Naturwissenschaften* **25** (1937) 513.

[104] C. Brans and R. H. Dicke, *Mach's principle and a relativistic theory of gravitation*, *Phys. Rev.* **124** (1961) 925.

[105] J.-P. Uzan, *Varying Constants, Gravitation and Cosmology*, *Living Rev. Rel.* **14** (2011) 2 [`1009.5514`].

[106] C. M. Will, *The Confrontation between General Relativity and Experiment*, *Living Rev. Rel.* **17** (2014) 4 [`1403.7377`].

[107] C. J. Copi, A. N. Davis and L. M. Krauss, *New nucleosynthesis constraint on the variation of g*, *Phys. Rev. Lett.* **92** (2004) 171301.

[108] J. Alvey, N. Sabti, M. Escudero and M. Fairbairn, *Improved BBN Constraints on the Variation of the Gravitational Constant*, *Eur. Phys. J. C* **80** (2020) 148 [`1910.10730`].

[109] F. Wu and X. Chen, *Cosmic microwave background with Brans-Dicke gravity II: constraints with the WMAP and SDSS data*, *Phys. Rev.* **D82** (2010) 083003 [`0903.0385`].

[110] E. Gaztañaga, E. García-Berro, J. Isern, E. Bravo and I. Domínguez, *Bounds on the possible evolution of the gravitational constant from cosmological type-ia supernovae*, *Phys. Rev. D* **65** (2001) 023506.

[111] E. Garcia-Berro, Y. Kubyshin, P. Loren-Aguilar and J. Isern, *The Variation of the Gravitational Constant Inferred from the Hubble Diagram of Type ia Supernovae*, *International Journal of Modern Physics D* **15** (2006) 1163 [`gr-qc/0512164`].

[112] E. García-Berro, J. Isern and Y. A. Kubyshin, *Astronomical measurements and constraints on the variability of fundamental constants*, A&A Rev. **14** (2007) 113.

[113] E. García-Berro, P. Lorén-Aguilar, S. Torres, L. G. Althaus and J. Isern, *An upper limit to the secular variation of the gravitational constant from white dwarf stars*, J. Cosmology Astropart. Phys. **2011** (2011) 021 [`1105.1992`].

[114] R. Tomaschitz, *Effect of a varying gravitational constant on the SN Ia Hubble diagram, AGN luminosity evolution, and X-ray source counts*, Ap&SS **325** (2010) 259.

[115] J. Mould and S. A. Uddin, *Constraining a Possible Variation of G with Type Ia Supernovae*, PASA **31** (2014) e015 [`1402.1534`].

[116] S. Degl'Innocenti, G. Fiorentini, G. G. Raffelt, B. Ricci and A. Weiss, *Time variation of Newton's constant and the age of globular clusters*, *Astron. Astrophys.* **312** (1996) 345 [`astro-ph/9509090`].

[117] E. V. Pitjeva and N. P. Pitjev, *Relativistic effects and dark matter in the Solar system from observations of planets and spacecraft*, *Monthly Notices of the Royal Astronomical Society* **432** (2013) 3431 [`https://academic.oup.com/mnras/article-pdf/432/4/3431/18606903/stt695.p`

[118] A. Fienga, J. Laskar, P. Exertier, H. Manche and M. Gastineau, *Tests of General relativity with planetary orbits and Monte Carlo simulations*, *arXiv e-prints* (2014) arXiv:1409.4932 [1409.4932].

[119] A. Genova, E. Mazarico, S. Goossens, F. G. Lemoine, G. A. Neumann, D. E. Smith et al., *Solar system expansion and strong equivalence principle as seen by the nasa messenger mission*, *Nat. Commun.* **9** (2019) 044003.

[120] J. D. Anderson, J. K. Campbell, R. F. Jurgens and E. L. Lau, *Recent developments in solar-system tests of general relativity.*, in *Marcel Grossmann Meeting on General Relativity*, p. 353, Jan., 1992.

[121] J. G. Williams, S. G. Turyshev and D. H. Boggs, *Progress in lunar laser ranging tests of relativistic gravity*, *Phys. Rev. Lett.* **93** (2004) 261101 [gr-qc/0411113].

[122] N. Yunes, K. Yagi and F. Pretorius, *Theoretical Physics Implications of the Binary Black-Hole Mergers GW150914 and GW151226*, *Phys. Rev. D* **94** (2016) 084002 [1603.08955].

[123] J. R. Oppenheimer and G. M. Volkoff, *On massive neutron cores*, *Phys. Rev.* **55** (1939) 374.

[124] T. Damour and G. Esposito-Farese, *Nonperturbative strong field effects in tensor - scalar theories of gravitation*, *Phys. Rev. Lett.* **70** (1993) 2220.

[125] J. Wu, Q. Li, J. Liu, C. Xue, S. Yang, C. Shao et al., *Progress in Precise Measurements of the Gravitational Constant*, *Annalen Phys.* **531** (2019) 1900013.

[126] J. M. Lattimer and M. Prakash, *The physics of neutron stars*, *Science* **304** (2004) 536 [astro-ph/0405262].

[127] P. Haensel, J. L. Zdunik and F. Douchin, *Equation of state of dense matter and the minimum mass of cold neutron stars*, *Astron. Astrophys.* **385** (2002) 301 [astro-ph/0201434].

[128] S. Koranda, N. Stergioulas and J. L. Friedman, *Upper limit set by causality on the rotation and mass of uniformly rotating relativistic stars*, *Astrophys. J.* **488** (1997) 799 [astro-ph/9608179].

[129] C. E. Rhoades, Jr. and R. Ruffini, *Maximum mass of a neutron star*, *Phys. Rev. Lett.* **32** (1974) 324.

[130] A. Buonanno, B. Iyer, E. Ochsner, Y. Pan and B. S. Sathyaprakash, *Comparison of post-Newtonian templates for compact binary inspiral signals in gravitational-wave detectors*, *Phys. Rev. D* **80** (2009) 084043 [0907.0700].

[131] C. Messenger and J. Read, *Measuring a cosmological distance-redshift relationship using only gravitational wave observations of binary neutron star coalescences*, *Phys. Rev. Lett.* **108** (2012) 091101 [1107.5725].

[132] Planck Collaboration, Ade, P. A. R., Aghanim, N., Arnaud, M., Ashdown, M., Aumont, J. et al., *Planck 2015 results - xiii. cosmological parameters*, *A&A* **594** (2016) A13.

[133] B. Sathyaprakash et al., *Scientific Objectives of Einstein Telescope*, *Class. Quant. Grav.* **29** (2012) 124013 [1206.0331].

[134] LIGO SCIENTIFIC, VIRGO collaboration, *Population Properties of Compact Objects from the Second LIGO-Virgo Gravitational-Wave Transient Catalog*, 2010.14533.

[135] B. D. Metzger and E. Berger, *What is the Most Promising Electromagnetic Counterpart of a Neutron Star Binary Merger?*, ApJ **746** (2012) 48 [1108.6056].

[136] S. Borhanian, *gwbench: a novel Fisher information package for gravitational-wave benchmarking*, 2010.15202.

[137] J. D. Barrow, *Varying constants*, *Phil. Trans. Roy. Soc. Lond. A* **363** (2005) 2139 [astro-ph/0511440].

[138] S. E. Perkins, N. Yunes and E. Berti, *Probing fundamental physics with gravitational waves: The next generation*, Phys. Rev. D **103** (2021) 044024 [2010.09010].

[139] F. Özel and P. Freire, *Masses, radii, and the equation of state of neutron stars*, Annual Review of Astronomy and Astrophysics **54** (2016) 401 [https://doi.org/10.1146/annurev-astro-081915-023322].

[140] J. M. Lattimer, *The nuclear equation of state and neutron star masses*, Annual Review of Nuclear and Particle Science **62** (2012) 485 [https://doi.org/10.1146/annurev-nucl-102711-095018].

[141] J. M. Lattimer, M. Prakash, D. Masak and A. Yahil, *Rapidly Rotating Pulsars and the Equation of State*, ApJ **355** (1990) 241.

[142] K. C. Gendreau, Z. Arzoumanian, P. W. Adkins, C. L. Albert, J. F. Anders, A. T. Aylward et al., *The Neutron star Interior Composition Explorer (NICER): design and development*, in *Space Telescopes and Instrumentation 2016: Ultraviolet to Gamma Ray*, J.-W. A. den Herder, T. Takahashi and M. Bautz, eds., vol. 9905 of *Society of Photo-Optical Instrumentation Engineers (SPIE) Conference Series*, p. 99051H, July, 2016, DOI.

[143] G. Prigozhin, K. Gendreau, J. P. Doty, R. Foster, R. Remillard, A. Malonis et al., *NICER instrument detector subsystem: description and performance*, in *Space Telescopes and Instrumentation 2016: Ultraviolet to Gamma Ray*, J.-W. A. den Herder, T. Takahashi and M. Bautz, eds., vol. 9905 of *Society of Photo-Optical Instrumentation Engineers (SPIE) Conference Series*, p. 99051I, July, 2016, DOI.

[144] K. Chatziioannou, *Neutron-star tidal deformability and equation-of-state constraints*, General Relativity and Gravitation **52** (2020) 109 [2006.03168].

[145] J. A. Clark, A. Bauswein, N. Stergioulas and D. Shoemaker, *Observing gravitational waves from the post-merger phase of binary neutron star coalescence*, Classical and Quantum Gravity **33** (2016) 085003 [1509.08522].

[146] K. Hotokezaka, K. Kiuchi, K. Kyutoku, T. Muranushi, Y.-i. Sekiguchi, M. Shibata et al., *Remnant massive neutron stars of binary neutron star mergers: Evolution process and gravitational waveform*, Phys. Rev. D **88** (2013) 044026 [`1307.5888`].

[147] N. Sarin and P. D. Lasky, *The evolution of binary neutron star post-merger remnants: a review*, *General Relativity and Gravitation* **53** (2021) 59 [`2012.08172`].

[148] KAGRA, LIGO SCIENTIFIC, VIRGO, VIRGO collaboration, *Prospects for observing and localizing gravitational-wave transients with Advanced LIGO, Advanced Virgo and KAGRA*, *Living Rev. Rel.* **21** (2018) 3 [`1304.0670`].

[149] F. Acernese et al., *Advanced virgo: a second-generation interferometric gravitational wave detector*, *Classical and Quantum Gravity* **32** (2014) 024001.

[150] LIGO SCIENTIFIC, VIRGO collaboration, *GWTC-1: A Gravitational-Wave Transient Catalog of Compact Binary Mergers Observed by LIGO and Virgo during the First and Second Observing Runs*, *Phys. Rev.* **X9** (2019) 031040 [`1811.12907`].

[151] LIGO SCIENTIFIC, VIRGO collaboration, *GWTC-2: Compact Binary Coalescences Observed by LIGO and Virgo During the First Half of the Third Observing Run*, *Phys. Rev. X* **11** (2021) 021053 [`2010.14527`].

[152] LIGO SCIENTIFIC, VIRGO collaboration, *GWTC-2.1: Deep Extended Catalog of Compact Binary Coalescences Observed by LIGO and Virgo During the First Half of the Third Observing Run*, `2108.01045`.

[153] S. Olsen, T. Venumadhav, J. Mushkin, J. Roulet, B. Zackay and M. Zaldarriaga, *New binary black hole mergers in the LIGO–Virgo O3a data*, `2201.02252`.

[154] A. H. Nitz, S. Kumar, Y.-F. Wang, S. Kastha, S. Wu, M. Schäfer et al., *4-OGC: Catalog of gravitational waves from compact-binary mergers*, `2112.06878`.

[155] LIGO SCIENTIFIC, VIRGO collaboration, *Search for Post-merger Gravitational Waves from the Remnant of the Binary Neutron Star Merger GW170817*, *Astrophys. J. Lett.* **851** (2017) L16 [`1710.09320`].

[156] LIGO Scientific Collaboration, *Instrument science white paper*, 2015.

[157] K. Ackley, V. B. Adya, P. Agrawal, P. Altin, G. Ashton, M. Bailes et al., *Neutron Star Extreme Matter Observatory: A kilohertz-band gravitational-wave detector in the global network*, PASA **37** (2020) e047 [`2007.03128`].

[158] M. Maggiore et al., *Science Case for the Einstein Telescope*, *JCAP* **03** (2020) 050 [`1912.02622`].

[159] P. Peng and X. Chen, *The last migration trap of compact objects in AGN accretion disc*, *Mon. Not. Roy. Astron. Soc.* **505** (2021) 1324 [`2104.07685`].

[160] X. Chen, S. Li and Z. Cao, *Mass-redshift degeneracy for the gravitational-wave sources in the vicinity of supermassive black holes*, MNRAS **485** (2019) L141 [`1703.10543`].

[161] X. Chen and W.-B. Han, *Extreme-mass-ratio inspirals produced by tidal capture of binary black holes*, *Communications Physics* **1** (2018) 1.

[162] J. Miralda-Escudé and A. Gould, *A Cluster of Black Holes at the Galactic Center*, ApJ **545** (2000) 847 [`astro-ph/0003269`].

[163] M. Freitag, P. Amaro-Seoane and V. Kalogera, *Stellar Remnants in Galactic Nuclei: Mass Segregation*, ApJ **649** (2006) 91 [`astro-ph/0603280`].

[164] F. Antonini and H. B. Perets, *Secular Evolution of Compact Binaries near Massive Black Holes: Gravitational Wave Sources and Other Exotica*, ApJ **757** (2012) 27 [`1203.2938`].

[165] C. Norman and J. Silk, *The dynamics and fueling of active nuclei*, ApJ **266** (1983) 502.

[166] D. Syer, C. J. Clarke and M. J. Rees, *Star-disc interactions near a massive black hole*, MNRAS **250** (1991) 505.

[167] P. Artymowicz, D. N. C. Lin and E. J. Wampler, *Star Trapping and Metallicity Enrichment in Quasars and Active Galactic Nuclei*, ApJ **409** (1993) 592.

[168] M. MacLeod and D. N. C. Lin, *The Effect of Star-Disk Interactions on Highly Eccentric Stellar Orbits in Active Galactic Nuclei: A Disk Loss Cone and Implications for Stellar Tidal Disruption Events*, ApJ **889** (2020) 94 [`1909.09645`].

[169] J. Goodman and J. C. Tan, *Supermassive Stars in Quasar Disks*, ApJ **608** (2004) 108 [`astro-ph/0307361`].

[170] Y. Levin, *Starbursts near supermassive black holes: young stars in the Galactic Centre, and gravitational waves in LISA band*, MNRAS **374** (2007) 515 [`astro-ph/0603583`].

[171] J.-M. Wang, C.-S. Yan, H.-Q. Gao, C. Hu, Y.-R. Li and S. Zhang, *Accretion Disks in Active Galactic Nuclei: Gas Supply Driven by Star Formation*, ApJ **719** (2010) L148 [`1007.4060`].

[172] B. McKernan, K. Ford and R. O'Shaughnessy, *Black hole, neutron star, and white dwarf merger rates in agn discs*, *Monthly Notices of the Royal Astronomical Society* **498** (2020) 4088.

[173] K. Ford and B. McKernan, *Binary black hole merger rates in agn disks versus nuclear star clusters: Loud beats quiet*, *arXiv preprint arXiv:2109.03212* (2021) .

[174] N. Aghanim, Y. Akrami, M. Ashdown, J. Aumont, C. Baccigalupi, M. Ballardini et al., *Planck 2018 results-vi. cosmological parameters*, *Astronomy & Astrophysics* **641** (2020) A6.

[175] R. P. Kerr, *Gravitational field of a spinning mass as an example of algebraically special metrics*, *Phys. Rev. Lett.* **11** (1963) 237.

[176] R. A. Isaacson, *Gravitational Radiation in the Limit of High Frequency. I. The Linear Approximation and Geometrical Optics*, *Physical Review* **166** (1968) 1263.

[177] L. A. Wainstein and V. D. Zubakov, *Extraction of Signals from Noise*, Dover books on physics and mathematical physics. Prentice-Hall, Englewood Cliffs, NJ, 1962.

[178] J. D. Creighton and W. G. Anderson, *Gravitational-wave physics and astronomy: An introduction to theory, experiment and data analysis*. John Wiley & Sons, 2012.

[179] B. F. Schutz and M. Tinto, *Antenna patterns of interferometric detectors of gravitational waves–i. linearly polarized waves*, *Monthly Notices of the Royal Astronomical Society* **224** (1987) 131.

[180] M. Tinto, *Antenna patterns of interferometric detectors of gravitational waves–ii. elliptically and randomly polarized waves*, *Monthly Notices of the Royal Astronomical Society* **226** (1987) 829.

[181] M. Breschi, S. Bernuzzi, F. Zappa, M. Agathos, A. Perego, D. Radice et al., *kiloHertz gravitational waves from binary neutron star remnants: time-domain model and constraints on extreme matter*, *Phys. Rev. D* **100** (2019) 104029 [1908.11418].

[182] E. E. Flanagan and T. Hinderer, *Constraining neutron star tidal Love numbers with gravitational wave detectors*, *Phys. Rev. D* **77** (2008) 021502 [0709.1915].

[183] P. J. Easter, P. D. Lasky, A. R. Casey, L. Rezzolla and K. Takami, *Computing Fast and Reliable Gravitational Waveforms of Binary Neutron Star Merger Remnants*, *Phys. Rev. D* **100** (2019) 043005 [1811.11183].

[184] T. Soultanis, A. Bauswein and N. Stergioulas, *Analytic models of the spectral properties of gravitational waves from neutron star merger remnants*, *arXiv preprint arXiv:2111.08353* (2021) [2111.08353].

[185] C. Cutler and E. E. Flanagan, *Gravitational waves from merging compact binaries: How accurately can one extract the binary's parameters from the inspiral waveform?*, *Physical Review D* **49** (1994) 2658.

[186] N. Cornish, L. Sampson, N. Yunes and F. Pretorius, *Gravitational wave tests of general relativity with the parameterized post-einsteinian framework*, *Physical Review D* **84** (2011) 062003.

[187] M. Vallisneri, *Testing general relativity with gravitational waves: A reality check*, Phys. Rev. D **86** (2012) 082001 [1207.4759].

[188] K. Kyutoku, M. Shibata and K. Taniguchi, *Gravitational waves from nonspinning black hole-neutron star binaries: Dependence on equations of state*, *Phys. Rev. D* **82** (2010) 044049.

[189] F. Douchin and P. Haensel, *A unified equation of state of dense matter and neutron star structure*, A&A **380** (2001) 151 [astro-ph/0111092].

[190] KAGRA Collaboration, LIGO Scientific Collaboration and Virgo Collaboration, *Advanced ligo, advanced virgo and kagra observing run plans*, 2019.

[191] S. Hild, *Beyond the second generation of laser-interferometric gravitational wave observatories*, *Classical and Quantum Gravity* **29** (2012) 124006.

[192] LIGO SCIENTIFIC collaboration, *Exploring the Sensitivity of Next Generation Gravitational Wave Detectors*, *Class. Quant. Grav.* **34** (2017) 044001 [1607.08697].

[193] C. S. Unnikrishnan, *Indigo and ligo-india: Scope and plans for gravitational wave research and precision metrology in india*, *International Journal of Modern Physics D* **22** (2013) 1341010.

[194] M. Saleem et al., *The science case for LIGO-India*, *Class. Quant. Grav.* **39** (2022) 025004 [2105.01716].

[195] G. Ashton et al., *BILBY: A user-friendly Bayesian inference library for gravitational-wave astronomy*, *Astrophys. J. Suppl.* **241** (2019) 27 [`1811.02042`].

[196] J. S. Speagle, *dynesty: a dynamic nested sampling package for estimating Bayesian posteriors and evidences*, *Mon. Not. Roy. Astron. Soc.* **493** (2020) 3132 [`1904.02180`].

[197] C. S. Reynolds, *Measuring Black Hole Spin Using X-Ray Reflection Spectroscopy*, Space Sci. Rev. **183** (2014) 277 [`1302.3260`].

[198] K. Danzmann, L. S. Team et al., *Lisa: laser interferometer space antenna for gravitational wave measurements*, *Classical and Quantum Gravity* **13** (1996) A247.

[199] D. Chatterjee, A. H. K. R., G. Holder, D. E. Holz, S. Perkins, K. Yagi et al., *Cosmology with Love: Measuring the Hubble constant using neutron star universal relations*, *Phys. Rev. D* **104** (2021) 083528 [`2106.06589`].

[200] C. Messenger, K. Takami, S. Gossan, L. Rezzolla and B. S. Sathyaprakash, *Source redshifts from gravitational-wave observations of binary neutron star mergers*, *Phys. Rev. X* **4** (2014) 041004.

[201] J.-P. Zhu, B. Zhang, Y.-W. Yu and H. Gao, *Neutron Star Mergers in Active Galactic Nucleus Accretion Disks: Cocoon and Ejecta Shock Breakouts*, *Astrophys. J. Lett.* **906** (2021) L11 [`2011.08428`].

[202] M. Zevin, S. S. Bavera, C. P. L. Berry, V. Kalogera, T. Fragos, P. Marchant et al., *One Channel to Rule Them All? Constraining the Origins of Binary Black Holes Using Multiple Formation Pathways*, *Astrophys. J.* **910** (2021) 152 [`2011.10057`].

[203] LIGO SCIENTIFIC, VIRGO collaboration, *Observation of Gravitational Waves from Two Neutron Star-Black Hole Coalescences*, ApJ **915** (2021) L5 [`2106.15163`].

[204] M. Morris, *Massive Star Formation near the Galactic Center and the Fate of the Stellar Remnants*, ApJ **408** (1993) 496.

[205] F. Antonini, *On the Distribution of Stellar Remnants around Massive Black Holes: Slow Mass Segregation, Star Cluster Inspirals, and Correlated Orbits*, ApJ **794** (2014) 106 [`1402.4865`].

[206] N. Yunes, F. Pretorius and D. Spergel, *Constraining the evolutionary history of Newton's constant with gravitational wave observations*, *Phys. Rev. D* **81** (2010) 064018 [`0912.2724`].

[207] A. Vijaykumar, S. J. Kapadia and P. Ajith, *Constraints on the time variation of the gravitational constant using gravitational wave observations of binary neutron stars*, `2003.12832`.

[208] N. Yunes, M. Coleman Miller and J. Thornburg, *The Effect of Massive Perturbers on Extreme Mass-Ratio Inspiral Waveforms*, *Phys. Rev. D* **83** (2011) 044030 [`1010.1721`].

[209] C. Bonvin, C. Caprini, R. Sturani and N. Tamanini, *Effect of matter structure on the gravitational waveform*, *Phys. Rev. D* **95** (2017) 044029 [`1609.08093`].

[210] LIGO SCIENTIFIC, VIRGO collaboration, *A guide to LIGO–Virgo detector noise and extraction of transient gravitational-wave signals*, *Class. Quant. Grav.* **37** (2020) 055002 [`1908.11170`].

[211] S. Sato et al., *The status of DECIGO*, *J. Phys. Conf. Ser.* **840** (2017) 012010.

[212] N. Tamanini, A. Klein, C. Bonvin, E. Barausse and C. Caprini, *Peculiar acceleration of stellar-origin black hole binaries: Measurement and biases with LISA*, *Phys. Rev. D* **101** (2020) 063002 [`1907.02018`].

[213] K. Inayoshi, N. Tamanini, C. Caprini and Z. Haiman, *Probing stellar binary black hole formation in galactic nuclei via the imprint of their center of mass acceleration on their gravitational wave signal*, *Phys. Rev. D* **96** (2017) 063014 [`1702.06529`].

[214] J. Binney and S. Tremaine, *Galactic dynamics*. Princeton University Press, Princeton, NJ, 1987.

[215] J. Bovy, *Dynamics and Astrophysics of Galaxies (in preparation)*. Princeton University Press, Princeton, NJ, 2023.

[216] T. Dietrich et al., *Matter imprints in waveform models for neutron star binaries: Tidal and self-spin effects*, *Phys. Rev. D* **99** (2019) 024029 [1804.02235].

[217] LIGO Scientific Collaboration, "LIGO Algorithm Library - LALSuite." free software (GPL), 2018. 10.7935/GT1W-FZ16.

[218] I. M. Romero-Shaw et al., *Bayesian inference for compact binary coalescences with bilby: validation and application to the first LIGO–Virgo gravitational-wave transient catalogue*, *Mon. Not. Roy. Astron. Soc.* **499** (2020) 3295 [2006.00714].

[219] N. J. Cornish, *Fast Fisher Matrices and Lazy Likelihoods*, 1007.4820.

[220] B. Zackay, L. Dai and T. Venumadhav, *Relative Binning and Fast Likelihood Evaluation for Gravitational Wave Parameter Estimation*, 1806.08792.

[221] N. J. Cornish, *Heterodyned likelihood for rapid gravitational wave parameter inference*, Phys. Rev. D **104** (2021) 104054 [2109.02728].

[222] K. Krishna, A. Vijaykumar, A. Ganguly and P. Ajith, *Relative Binning in BILBY*, .

[223] LIGO SCIENTIFIC, VIRGO collaboration, *Open data from the first and second observing runs of Advanced LIGO and Advanced Virgo*, *SoftwareX* **13** (2021) 100658 [1912.11716].

[224] DES, DARK ENERGY CAMERA GW-EM collaboration, *The Electromagnetic Counterpart of the Binary Neutron Star Merger LIGO/Virgo GW170817. I. Discovery of the Optical Counterpart Using the Dark Energy Camera*, *Astrophys. J. Lett.* **848** (2017) L16 [1710.05459].

[225] A. J. Levan et al., *The environment of the binary neutron star merger GW170817*, *Astrophys. J. Lett.* **848** (2017) L28 [`1710.05444`].

[226] K. Gultekin et al., *The M-sigma and M-L Relations in Galactic Bulges and Determinations of their Intrinsic Scatter*, *Astrophys. J.* **698** (2009) 198 [`0903.4897`].

[227] S. Khan, S. Husa, M. Hannam, F. Ohme, M. Pürrer, X. Jiménez Forteza et al., *Frequency-domain gravitational waves from nonprecessing black-hole binaries. II. A phenomenological model for the advanced detector era*, *Phys. Rev. D* **93** (2016) 044007 [`1508.07253`].

[228] LIGO SCIENTIFIC, VIRGO collaboration, *GW170608: Observation of a 19-solar-mass Binary Black Hole Coalescence*, *Astrophys. J. Lett.* **851** (2017) L35 [`1711.05578`].

[229] V. Srivastava, D. Davis, K. Kuns, P. Landry, S. Ballmer, M. Evans et al., *Science-driven Tunable Design of Cosmic Explorer Detectors*, May, 2022. 10.3847/1538-4357/ac5f04.

[230] M. Vallisneri, *Use and abuse of the Fisher information matrix in the assessment of gravitational-wave parameter-estimation prospects*, *Phys. Rev. D* **77** (2008) 042001 [`gr-qc/0703086`].

[231] K. Yagi and N. Seto, *Detector configuration of DECIGO/BBO and identification of cosmological neutron-star binaries*, *Phys. Rev. D* **83** (2011) 044011 [`1101.3940`].

[232] K. Yagi and N. Seto, *Erratum: Detector configuration of decigo/bbo and identification of cosmological neutron-star binaries [phys. rev. d 83, 044011 (2011)]*, *Phys. Rev. D* **95** (2017) 109901.

[233] P. Amaro-Seoane, S. Aoudia, S. Babak, P. Binétruy, E. Berti, A. Bohé et al., *Low-frequency gravitational-wave science with eLISA/NGO*, *Classical and Quantum Gravity* **29** (2012) 124016 [`1202.0839`].

[234] TIANQIN collaboration, *TianQin: a space-borne gravitational wave detector*, *Class. Quant. Grav.* **33** (2016) 035010 [`1512.02076`].

[235] R. Barbieri, S. Savastano, L. Speri, A. Antonelli, L. Sberna, O. Burke et al., *Constraining the evolution of Newton's constant with slow inspirals observed from spaceborne gravitational-wave detectors*, `2207.10674`.

[236] B. McKernan, K. E. S. Ford and R. O'Shaughnessy, *Black hole, neutron star, and white dwarf merger rates in AGN discs*, *Mon. Not. Roy. Astron. Soc.* **498** (2020) 4088 [`2002.00046`].

[237] M. J. Graham et al., *Candidate Electromagnetic Counterpart to the Binary Black Hole Merger Gravitational Wave Event S190521g*, *Phys. Rev. Lett.* **124** (2020) 251102 [`2006.14122`].

[238] A. Toubiana et al., *Detectable environmental effects in GW190521-like black-hole binaries with LISA*, *Phys. Rev. Lett.* **126** (2021) 101105 [`2010.06056`].

[239] L. Sberna et al., *Observing GW190521-like binary black holes and their environment with LISA*, *Phys. Rev. D* **106** (2022) 064056 [`2205.08550`].

[240] X. Chen, S. Li and Z. Cao, *Mass–redshift degeneracy for the gravitational-wave sources in the vicinity of supermassive black holes*, *Mon. Not. Roy. Astron. Soc.* **485** (2019) L141 [`1703.10543`].

[241] L. Randall and Z.-Z. Xianyu, *A Direct Probe of Mass Density Near Inspiraling Binary Black Holes*, *Astrophys. J.* **878** (2019) 75 [`1805.05335`].

[242] K. W. K. Wong, V. Baibhav and E. Berti, *Binary radial velocity measurements with space-based gravitational-wave detectors*, *Mon. Not. Roy. Astron. Soc.* **488** (2019) 5665 [`1902.01402`].

[243] A. Nishizawa, K. Yagi, A. Taruya and T. Tanaka, *Cosmology with space-based gravitational-wave detectors — dark energy and primordial gravitational waves —*, *Phys. Rev. D* **85** (2012) 044047 [`1110.2865`].

[244] LIGO Scientific Collaboration, *Instrument Science White Paper 2019*, 2019.

[245] PLANCK collaboration, *Planck 2018 results. VI. Cosmological parameters*, `1807.06209`.

[246] A. G. Riess et al., *A 2.4% Determination of the Local Value of the Hubble Constant*, *Astrophys. J.* **826** (2016) 56 [`1604.01424`].

[247] W. Del Pozzo, *Inference of the cosmological parameters from gravitational waves: application to second generation interferometers*, *Phys. Rev.* **D86** (2012) 043011 [`1108.1317`].

[248] H.-Y. Chen, M. Fishbach and D. E. Holz, *A two per cent Hubble constant measurement from standard sirens within five years*, *Nature* **562** (2018) 545 [`1712.06531`].

[249] LIGO SCIENTIFIC, VIRGO collaboration, *A Standard Siren Measurement of the Hubble Constant from GW170817 without the Electromagnetic Counterpart*, *Astrophys. J.* **871** (2019) L13 [`1807.05667`].

[250] R. Nair, S. Bose and T. D. Saini, *Measuring the Hubble constant: Gravitational wave observations meet galaxy clustering*, *Phys. Rev.* **D98** (2018) 023502 [`1804.06085`].

[251] K. Osato, *Exploring the distance-redshift relation with gravitational wave standard sirens and tomographic weak lensing*, *Phys. Rev.* **D98** (2018) 083524 [`1807.00016`].

[252] DES, LIGO SCIENTIFIC, VIRGO collaboration, *First Measurement of the Hubble Constant from a Dark Standard Siren using the Dark Energy Survey Galaxies and the LIGO/Virgo Binary–Black-hole Merger GW170814*, *Astrophys. J.* **876** (2019) L7 [`1901.01540`].

[253] R. Gray et al., *Cosmological Inference using Gravitational Wave Standard Sirens: A Mock Data Challenge*, `1908.06050`.

[254] LIGO SCIENTIFIC, VIRGO collaboration, *A gravitational-wave measurement of the Hubble constant following the second observing run of Advanced LIGO and Virgo*, `1908.06060`.

[255] T. Namikawa, A. Nishizawa and A. Taruya, *Detecting Black-Hole Binary Clustering via the Second-Generation Gravitational-Wave Detectors*, *Phys. Rev.* **D94** (2016) 024013 [`1603.08072`].

[256] F. Calore, A. Cuoco, T. Regimbau, S. Sachdev and P. D. Serpico, *Cross-correlating galaxy catalogs and gravitational waves: a tomographic approach*, `2002.02466`.

[257] S. Mukherjee, B. D. Wandelt and J. Silk, *Probing the theory of gravity with gravitational lensing of gravitational waves and galaxy surveys*, `1908.08951`.

[258] N. Kaiser, *On the Spatial correlations of Abell clusters*, *Astrophys. J. Lett.* **284** (1984) L9.

[259] SDSS collaboration, *The Luminosity and color dependence of the galaxy correlation function*, *Astrophys. J.* **630** (2005) 1 [`astro-ph/0408569`].

[260] S. D. Landy and A. S. Szalay, *Bias and variance of angular correlation functions*, *Astrophys. J.* **412** (1993) 64.

[261] R. Essick, W. M. Farr, M. Fishbach, D. E. Holz and E. Katsavounidis, *(An)isotropy measurement with gravitational wave observations*, *Phys. Rev. D* **107** (2023) 043016 [`2207.05792`].

[262] M. Sinha and L. H. Garrison, *Corrfunc — A Suite of Blazing Fast Correlation Functions on the CPU*, *Mon. Not. Roy. Astron. Soc.* **491** (2020) 3022 [`1911.03545`].

[263] M. Sinha and L. H. Garrison, *Corrfunc: Blazing fast correlation functions with AVX512F SIMD Intrinsics*, in *Communications in Computer and Information Science: Proceedings*

of the 'Software Challenges to Exascale Computing' Second Workshop, SCEC 2018, Delhi, India, December 13-14 2018, Vol. 964, pp. 3-20, 2019, DOI [1911.08275].

[264] A. Agrawal, R. Makiya, C.-T. Chiang, D. Jeong, S. Saito and E. Komatsu, *Generating Log-normal Mock Catalog of Galaxies in Redshift Space*, *JCAP* **1710** (2017) 003 [1706.09195].

[265] M. Hannam, P. Schmidt, A. Bohé, L. Haegel, S. Husa, F. Ohme et al., *Simple Model of Complete Precessing Black-Hole-Binary Gravitational Waveforms*, *Phys. Rev. Lett.* **113** (2014) 151101 [1308.3271].

[266] C. M. Biwer, C. D. Capano, S. De, M. Cabero, D. A. Brown, A. H. Nitz et al., *PyCBC Inference: A Python-based parameter estimation toolkit for compact binary coalescence signals*, *Publ. Astron. Soc. Pac.* **131** (2019) 024503 [1807.10312].

[267] S. Borhanian and B. S. Sathyaprakash, *Listening to the Universe with Next Generation Ground-Based Gravitational-Wave Detectors*, 2202.11048.

[268] A. Cooray and R. K. Sheth, *Halo Models of Large Scale Structure*, *Phys. Rept.* **372** (2002) 1 [astro-ph/0206508].

[269] S. Kumar, A. Vijaykumar and A. H. Nitz, *Detecting Baryon Acoustic Oscillations with Third-generation Gravitational Wave Observatories*, *Astrophys. J.* **930** (2022) 113 [2110.06152].